Single-source precursor synthesis of gold (I) sulphide nanostructures for application in dye sensitized solar cells

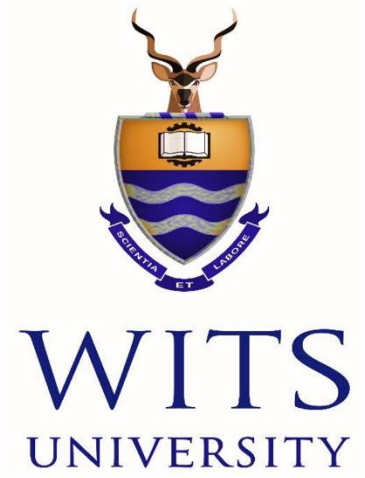

Esmie Mposa

1796980

Principal Supervisor: Prof N. Moloto

Co-supervisors: Dr S. S. Gqoba

Dr L.E.F. Machogo-Phao

A dissertation submitted to the Faculty of Science, University of the Witwatersrand, in partial fulfilment for the degree of Master of Science in Chemistry

2022

Declaration

I declare that the work reported in this dissertation is my own independent work, submitted at the School of Chemistry, University of the Witwatersrand, Johannesburg. This work has not been submitted for any degree or examination in any other institution of higher learning.

	25/05/2022
Candidate	Date
	01/06/2022
Supervisor	Date
	
Co-Supervisor	Date
	02/06/2022
Co-Supervisor	Date

Abstract

The current study focused on synthesis of gold (I) sulphide nanostructures from a single-source precursor for use as a counter electrode (CE) in dye-sensitized solar cells (DSSCs). The single-source precursor method was chosen as opposed to the usual dual source precursor synthesis method because there is safety in carrying out the synthesis procedures, ease of separation of nanocrystalline material and the use of lower decomposition temperatures. Gold dithiocarbamate complexes were synthesized using ethanol and dichloromethane as solvents for three hours. The complexes were characterized using Fourier transformer infrared spectroscopy (FTIR), nuclear magnetic resonance spectroscopy (NMR), single crystal X-ray diffraction (XRD), elemental analysis, ultraviolet-visible absorption spectroscopy, high resolution mass spectroscopy and thermogravimetric analysis. Upon complexation, there was a shift in the FTIR wavenumbers of the main functional groups from low to high frequencies. An up-field shift was observed in the NMR spectra of the complexes with respect to their relevant ligands. Single crystal XRD showed that the atomic packing of the complexes was orthorhombic with a space group of Fddd and triclinic with a space group P-1. All complexes decomposed within a temperature range of 200-250 ℃ to form the Au_2S nanostructures.

The colloidal synthesis method was employed for the synthesis of the nanostructures because of its flexibility and ability to vary reaction parameters. As a result, the reaction time, temperature, precursor source and precursor concentration were varied to find the optimum conditions for the synthesis of the nanostructures. Au_2S nanostructures were favoured with an average size of ~ 3 nm at a reaction temperature of 170 ℃ for 45 min in oleylamine, oleic acid and 1-octadecene with a precursor concentration of 3.837 M. Only three reaction parameters had an influence on the synthesized nanostructures; longer reaction times (60 min) resulted in larger nanoparticles due to Ostwald ripening, higher temperatures (200 ℃) also resulted in an increase in the nanostructures' size and a mixed morphology was also observed due to the formation of elemental gold nanoparticles. A similar trend was also observed with precursor concentration, an increase in precursor concentration (7.674 M) resulted in an increase in the size of the synthesized nanostructures. The band gap energies of the nanostructures varied accordingly, the smaller the size of the nanostructures, the larger the band gap energy due to quantum confinement effects.

The electrocatalytic activity of the Au_2S nanostructures towards the reduction of the triiodide ions at the electrode/electrolyte interface was investigated in a three-electrode system and the results were compared to that of Pt under similar conditions. The Pt and Au_2S had a peak current density of 1.45 mA and 1.20 mA, respectively and the minimal difference between the two suggests comparable catalytic activity of the Au_2S CE. Consequently, DSSCs assembled with the Au_2S reached a power conversion efficiency of 1.94% which was slightly lower but comparable to the conventional Pt CE 2.5%.

Acknowledgements

- For everything accomplished this far, I give all the glory and honour to God Almighty, El Shaddai, for opening this door of possibilities, for taking care of me throughout the covid pandemic, and for renewing my strength every day.
- My sincerest appreciation goes to my supervisors Professor Nosipho Moloto, Dr. Siziwe, S. Gqoba and Dr. Lerato, E.F. Machogo-Phao for their guidance and mentorship from honours up to the completion of this master's program.
- Much appreciation goes to WITS MMU staff for assisting with the characterization techniques of the nanostructures, (XRD, TEM and SEM) and to Dr. Rudolph Erasmus, many thanks for assisting with the acquisition of the Raman spectra. From the single crystal XRD unit, special thanks go to Professor Manuel Fernandes for assisting with solving crystal structures of the complexes. I would also like to thank Dr. Eric Morifi for assisting with setting up experiments to run on the HRMS for the complexes. And a special thanks to Dr. Grace N. Ngubeni for assisting with the application of the Au_2S CE in the construction of the DSSC.
- My special appreciation also goes to all my colleagues in Lab 330B and CATMAT group, my friends, Lineo Mxakaza, Olusola Akinbami, Zakhele Ndala and Ndivhuwo Shumbula for the emotional support.
- My gratitude goes to the School of Chemistry at Wits University and the National Research Foundation (RSA) for funding.
- I would like to thank my parents, Mr. and Mrs. Mposa and my sister Ella Mposa Chasonkhana for all the sacrifices made in supporting me to pursue my dream and for the spiritual support rendered. And to my biggest supporter, Mr. William Mangaka, thank you for believing in me and for the continued love and support.

Dedication

This dissertation is dedicated to my parents, my sister and all my family and friends who have been with me throughout this journey

List of presentations

- Poster presentation at the South African Chemical Institute Young Chemists' Symposium. Royal Society of Chemistry local section (SACI/RSC) from the 8th-9th July 2021, (Online, Teams meeting). **Title:** Synthesis and characterization of gold (I) sulphide (Au_2S) nanostructures from a single source precursor.

- Oral presentation at the 12th annual University of the Witwatersrand's cross-faculty postgraduate symposium from 26th-28th of July 2021, (Online, Teams meeting). **Title:** Colloidal synthesis of gold (I) sulphide (Au_2S) nanostructures from a single-source precursor.

- Oral presentation at Catalysis and Materials' (CATMAT) seminar held at the School of Chemistry, University of the Witwatersrand on the 13th of August 2021. **Title:** Synthesis of gold (I) sulphide (Au_2S) nanostructures from a single source precursor.

- Oral presentation at the 10th Annual Nanoscience's Young Researchers' Symposium (SANi-NYRS) from the 7th-8th October 2021, (Online, Teams meeting). (1st prize MSc category). **Title:** Gold (I) sulphide nanostructures synthesized from a single-source precursor for application in dye sensitized solar cells (DSSCs).

List of publications

- E. Mposa, R. K. Sithole, Z. Ndala, G. N. Ngubeni, K. P. Mubiayi, P. M. Shumbula, L. E. F. Machogo-Phao, N. Moloto "Novel 2D-AuSe nanostructures as effective platinum replacement counter electrodes in dye-sensitized solar cells, RSC Advances, **12**, 2022, 12882-12890.

- E. Mposa, L. Mxakaza, O. Akinbami, G. N. Ngubeni, K.P. Mubiayi, L.E.F. Machogo-Phao, S. S. Gqoba, N. Moloto "Gold diethyldithiocarbamate complex as a single-source precursor for gold sulphide dye-sensitized counter electrode." To be submitted.

Table of contents

Declaration i

Abstract ii

Acknowledgements iv

Dedication v

List of presentations vi

List of publications vi

List of figures xi

List of tables xv

List of schemes xvi

List of abbreviations xvii

Synopsis xviii

CHAPTER 1 1

General background 1

1.1 Introduction 1

1.2 Problem Statement 4

1.3 Rationale 4

1.4 Aims and Objectives 5

1.5 References 6

CHAPTER 2 9

Literature review 9

2.1 Introduction to metal chalcogenides 9

2.1.1 Transition metal chalcogenides 9

2.1.2 Quantum confinement effects 11

2.1.3 Transition metal sulphides 12

2.1.4 Au_2S structure and properties 14
2.2 Synthesis of transition metal chalcogenides 16
2.2.1 Top-down synthesis approaches 16
2.2.2 Bottom-up synthesis approaches 19
2.3 Applications of transition metal chalcogenides 30
2.3.1 Dye-sensitized solar cells 30
2.4 References 36
CHAPTER 3 43
Synthesis and characterization of gold dithiocarbamate complexes single-source precursors 43
3.1 Introduction 43
3.2 Experimental section 45
3.2.1 Materials 45
3.2.2 Synthesis of gold dithiocarbamate complexes 46
3.3 Characterization techniques 47
3.4 Results and discussion 48
3.4.1 Purity of the complexes 48
3.4.2 Infrared spectral studies of the complexes 49
3.4.3 NMR Spectral studies 52
3.4.4 Description of crystal structures 56
3.4.5 Electronic spectra of the ligands and complexes 61
3.4.6 Thermal studies of the complexes 62
3.5 Conclusion 64
3.6 References 65
CHAPTER 4 67

Synthesis of Au_2S nanostructures from a dithiocarbamate gold complex as a single-source precursor: the effect of the nature of the precursor, temperature, time, and concentration on the properties of Au_2S nanostructures 67

4.1 Introduction 67

4.2 Experimental Section 70

4.2.1 Materials 70

4.2.2 Synthesis of Au_2S nanostructures 70

4.2.3 Characterization 71

4.2.4 Results and discussion 72

4.2.3 Effect of the nature of the single-source precursor on the synthesis of Au_2S nanostructures 83

4.2.4 Effect of temperature 86

4.2.5 Effect of time 89

4.2.6 Effect of concentration 93

4.3 Conclusion 96

4.4 References 97

CHAPTER 5 100

Investigating the electrocatalytic activity of Au_2S synthesized from a single-source precursor as counter electrode in dye-sensitized solar cells 100

5.1 Introduction 100

5.2 Experimental Section 102

5.2.1 Materials 102

5.2.2 Fabrication of the dye-sensitized solar cells 102

5.3 Results and discussion 104

5.4 Conclusion 109

5.5 References 109

CHAPTER 6 112
Overall conclusions and recommendations 112
6.1 Conclusions 112
6.2 Recommendations 112
Appendix 114
Chapter 3: Supporting information 114
Chapter 4: Supporting information 117

List of figures

Fig. 1.1: Global energy-related carbon dioxide emissions, 1990-2021 [9]. 2
Fig. 1.2: Three generations of solar cell technology [20]. 3
Fig. 2.1: (a) A comparison of the electronic energy levels of a bulk material and the nanoparticles and (b) direct and indirect band gap materials [5, 6]. 10
Fig. 2.2: Periodic table showing the transition metals and chalcogen atoms found in transition metal chalcogenides [9]. 11
Fig. 2.3: An illustration of quantum confinement effects showing the increase in the band-gap energy as the size of the nanoparticles decreases [5]. 12
Fig. 2.4: Unit cell of (a) ZnS (b) NiAs, (c) Au_2S (d) MnS, (e) CuS [20–22]. 13
Fig. 2.5: The atomic structure of layered MoS_2, where the Mo atom is sandwiched between the S atoms and the distance between two layers is 6.5 Å [25]. 14
Fig. 2.6: Cubic unit cell of Au_2S. 15
Fig. 2.7: (a) van Arkel–Ketelaar triangle of bonding, (b) Lewis dot diagram for bulk Au_2S [29, 32]. 16
Fig. 2.8: Schematic illustration of the bottom-up and top-down approaches of NPs synthesis [38]. 17
Fig. 2.9: (a) Hierarchal stages involved in UILPE (b) Sputter deposition of target material on the substrate [40, 46]. 19
Fig. 2.10: Schematic of a thermal-assisted CVD system [35]. 20
Fig. 2.11: Schematic of the sol-gel process showing all the stages [51]. 21
Fig. 2.12: A plot of the Gibbs free energy against the radius of the clusters [63]. 24
Fig. 2.13: A graphical illustration of LaMer and Dinegar nucleation [56]. 25
Fig. 2.14: (a) Potential energy graph of the thermodynamically and kinetically controlled reactions and (b) An illustration of the effect of temperature on the size of nanoparticles with an increase in temperature from T1 to T2 [81]. 29
Fig. 2.15: Schematic illustration and operating principles of a DSSC [92]. 31
Fig. 2.16: Schematic diagram of the reaction site at the counter electrode (CE)/electrolyte interface region and the electron transfer mechanism from the CE to the electrolyte material [100]. 33
Fig. 2.17: An illustration of a typical cyclic voltammogram for the CE of the DSSC [102]. 34

Fig. 2.18: (a) Set up for the measurement of an I-V curve (b) typical I-V curve for the DSSC [105, 107]. 36
Fig. 3.1: Resonance forms of the dithiocarbamates. 43
Fig. 3.2: Examples of some different types of DTCs (a) symmetrically disubstituted, (b) unsymmetrically disubstituted, and (c) monosubstituted. 44
Fig. 3.3: FT-IR spectra of the dithiocarbamate ligands with their respective gold complexes, (a) Au(DTC) complex, (b) Au($PDTC^1$) and (c) Au($PDTC^2$) complexes. 51
Fig. 3.4: ^{1}H NMR spectra of (a) Na-DTC ligand and (b) Au(DTC) complex 53
Fig. 3.5: ^{1}H NMR spectra of (a) Na-PDTC ligand and (b) Au($PDTC^1$) complex. 54
Fig. 3.6: ^{1}H NMR spectra of (a) NH_4-PDTC ligand and (b) Au($PDTC^2$) complex. 54
..... 55
Fig. 3.7: ^{13}C NMR spectra of (a) Na-DTC ligand and (b) Au(DTC) complex 55
..... 55
Fig. 3.8: ^{13}C NMR spectra of (a) Na-PDTC ligand and (b) Au($PDTC^1$) complex. 55
Fig. 3.9: ^{13}C NMR spectra of (a) NH_4-DTC ligand and (b) Au($PDTC^2$) complex. 56
Fig. 3.10: (a) A perspective view of the molecular structure of Au(DTC) complex showing the atom numbering scheme. Atomic displacement parameters are shown at the 50% probability level and (b) Single turns of helix-modulated $Au^{+}\cdots Au^{+}$ bonded filaments viewed perpendicularly and the Au(DTC) monomer has been enclosed in brackets. 58
Fig. 3.11: A perspective view of the molecular structure of Au (PDTC) complex showing the atom numbering scheme. Atomic displacement parameters (ADP's) are shown at the 50% probability level. 59
Fig. 3.12: UV-vis absorption spectra of (a) DTC ligand and Au(DTC) complex, (b) Na-$PDTC^1$ and Au($PDTC^1$) complex and (c) NH_4-$PDTC^2$ and Au($PDTC^2$) complex. 62
Fig. 3.13: TGA and DTG thermogramse of the dithiocarbamte complexes, (a) Au(DTC), (b) Au($PDTC^1$) and (c) Au($PDTC^2$). 64
Fig. 4.1: (a) Powder X-ray diffraction patterns of Au_2S matched to standard powder pattern of Au_2S and (b) Raman spectrum of the Au_2S nanostructures. 74
Fig. 4.2: (a) TEM image and (b) corresponding size distribution of Au_2S nanostructures. 75
Fig. 4.3: (a) SEM image and (b) EDS spectrum of the synthesized Au_2S nanostructures. 76

Fig. 4.4: (a) XPS survey spectrum, (b) C 1s, (c) N 1s, (d) Au 4f, (e) S 2p and (f) O 1s high-resolution spectra of capped of Au_2S nanostructures. 78
Fig. 4.5: FT-IR spectra of OA, OLA and Au_2S capped nanostructures..... 79
Fig. 4.6: ^1H NMR spectra of OA, OLA and Au_2S nanostructures, R=CH_2CH_2. 81
Fig. 4.7: (a) Tauc plot and (b) photoluminescence spectra of Au_2S nanostructures..... 83
Fig. 4.8: X-ray diffractogram patterns of the Au_2S nanostructures synthesized using (a) gold (ammonium) pyrrolidine dithiocarbamate complex (b) gold (sodium) pyrrolidine dithiocarbamate complex and (c) gold diethyldithiocarbamate complex. 84
..... 85
Fig. 4.9: (a-c) TEM images (d-f) corresponding size distribution of the Au_2S nanostructures synthesized using different single-source precursors. 85
Fig. 4.10: XRD patterns of Au_2S nanostructures synthesized at different temperatures. 87
Fig. 4.11: (a-c) TEM images and (d-f) corresponding distribution curves for the Au_2S nanostructures synthesized at different temperatures. 88
Fig. 4.12: (a) Tauc plots and (b) photoluminescence spectra of Au_2S nanostructures synthesized at different temperatures. 89
Fig. 4.13: XRD patterns of Au_2S nanostructures synthesized at different reaction times. 90
Fig. 4.14: (a-c) TEM images and (d-f) size distribution of Au_2S nanostructures synthesized at different reaction times. 92
Fig. 4.15: (a) Tauc plots and (b) photoluminescence spectra of Au_2S nanostructures synthesized at different reaction times. 93
Fig. 4.16: XRD patterns of Au_2S nanostructures synthesized using different precursor concentrations. 94
Fig. 4.17: (a-c) TEM images and (d-f) size distribution of Au_2S nanostructures synthesized using different precursor concentrations. 95
Fig. 4.18: (a) Tauc plots and (b) photoluminescence spectra of Au_2S nanostructures synthesized using different precursor concentrations..... 96
Fig. 5.1: Electrochemical measurements set-up [8]..... 103
Fig. 5.2: (a) Cyclic voltammograms of the Pt and Au_2S counter electrodes at a scan rate of 50 mV/s for the I^-/I_3^- redox couple, (b) the Au_2S CE for 30 consecutive cycles, with an insert

showing the 1st and the 30th cycle, (c) Au_2S CE at varying scan rates from 25 mV/s to 100mV/s and (d) dependence of anodic and cathodic peak currents on square root of the scan rates..... 105
Fig. 5.3: (a) Nyquist curves, (b) Tafel polarization plots and (c) equivalent circuit of Pt and Au_2S CEs..... 107
Fig. 5.4: (a) Schematic of the DSSC, (b) band diagram and (c) J-V curves of the DSSCs with Pt and Au_2S CEs..... 108

List of tables

Table 3.1: Analytical data for the synthesized complexes 49
Table 3.2: FT-IR assignments for the synthesized gold dithiocarbamate complexes 51
Table 3.3: Crystallographic characteristics, experimental and structure refinement details for the Au(DTC) and the Au(PDTC) complexes 59
Table 3.4a: Selected bond lengths and bond angles for the Au(DTC) complex 60
Table 3.4b: Selected bond lengths and bond angles for the Au(PDTC) complexes 60
Table 4.1: Summarized examples of metal dithiocarbamates and their respective metal sulphides 68
Table 4.2: Summary of the reaction conditions for the synthesis of Au_2S nanostructures 71
Table 4.3: Summary of the bonding configuration and elemental composition data obtained from the XPS spectra of Au_2S 77
Table 4.4: FT-IR assignments for oleic acid, oleylamine and Au_2S nanostructures 80
Table 4.5: NMR assignments for oleic acid, oleylamine and Au_2S nanostructures 82
Table 5.1: Electrochemical performance parameters from CV, EIS & Tafel polarization plots for the CEs 106
Table 5.2: J-V parameters of DSSCs with Pt and Au_2S CEs 109

List of schemes

Scheme 2.1: Generic representation of decomposition of SSP to form the nanoparticles. 30
Scheme 3.1: Synthesis of metal dithiocarbamate complexes by direct ligand addition. 45
Scheme 3.2: Synthesis of metal dithiocarbamate complexes by one-pot synthesis. 45
Scheme 4.1: The synthesis of Au_2S nanostructures from gold diethyldithiocarbamate single-source precursor. 73

List of abbreviations

CB: Conduction band

CE: Counter electrode

DSSC: Dye-sensitized solar cell

DTC: dithiocarbamate

EDX: Energy-dispersive X-ray spectroscopy

E_g: Energy gap

FTIR: Fourier Transform Infrared

FTO: Fluorine doped tin oxide

HOMO: Highest occupied molecular orbital

ITO: Indium tin oxide

LUMO: Lowest unoccupied molecular orbital

NMR: Nuclear Magnetic Resonance

NP: Nanoparticle

OA: Oleic acid

ODE: 1-Octadecene

OLA: Oleylamine

PCE: Photoelectric conversion efficiency

PL: Photoluminescence

PXRD: Powder x-ray diffraction

PV: Photovoltaic

SEM: Scanning electron microscopy

TEM: Transmission electron microscope

TMC: Transition metal chalcogenide

TMS: Transition metal sulphide

VB: Valence band

XPS: X-ray photoelectron spectroscopy

Synopsis

The aim of the study was to synthesize and characterize gold (I) sulphide nanostructures from a single-source precursor method and to investigate the electrocatalytic capabilities of the Au_2S nanostructures as a potential platinum replacement counter electrode in dye-sensitized solar cells. The layout of the dissertation is therefore presented below.

Chapter 1: Provides a brief background to the study, problem statement, motivation, and rationale for the study as well as the aims and objectives.

Chapter 2: Is the literature review of metal chalcogenides, in particular metal sulphides, their properties, and main synthetic routes. In addition, a review on DSSCs and the use of metal chalcogenides as counter electrode materials.

Chapter 3: Reports on the synthesis and characterization of gold dithiocarbamate single-source precursors.

Chapter 4: Reports on the colloidal synthesis and characterization of Au_2S nanostructures from the gold diethyldithiocarbamate single-source precursor and the effect of varying reaction parameters; single-source precursor source, temperature, time, and precursor concentration on the synthesis of the Au_2S nanostructures.

Chapter 5: Reports on the electrocatalytic properties of Au_2S nanostructures in the redox reaction of the iodide-triiodide system as an alternative counter electrode in dye-sensitized solar cells.

Chapter 6: This chapter looks at the conclusions of the study and suggests possible future studies.

CHAPTER 1
General background

1.1 Introduction

Energy has a profound impact on human development as it is a key source of economic growth as it is used as a basic component in many manufacturing and consumption activities [1, 2]. Fossil fuels, including coal, oil, and natural gas, are currently the world's primary energy sources formed from organic material hundreds of millions of years ago. The fossil fuels have fueled global economic development over the past centuries and yet they are finite resources and irreparably harm the environment by contributing to the greenhouse effect [3, 4]. The energy sector accounts for around two-thirds of greenhouse-gas emissions as more than 80% of global energy consumption is based on fossil fuels. Around 90% of energy-related greenhouse-gas emission is carbon dioxide (CO_2) and around 9% is methane gas (CH_4). The global energy-related CO_2 emissions reached a historic high of 36.65 Gt CO_2 in 2018 and it was the highest rate since 2013, and 70% higher than the average since 2010 as shown in **Fig. 1.1** [5–9]. Africa has been the lowest source of greenhouse gas emission owing to the lack of industrial development and it accounts for only 2–3% of the world's carbon dioxide emissions [10, 11]. A small number of nations are largely responsible for the African emissions from fossil fuels and cement production; South Africa, Egypt, Algeria, Nigeria, Libya, Morocco and Angola [11, 12]. South Africa, frequently referred to as Africa's worst polluter, relies on coal as the largest fuel source for electricity generation, which serves about 90% of the country's power, followed by nuclear (5.2%) and natural gas (3.2%) [13]. It is responsible for 42% of Africa's emissions, more than the whole of Sub-Saharan Africa combined, and 1% of global emissions [13]. According to a report released in 2020 by South Africa's environmental department, the country emitted 556-million metric tons of CO_2 in 2017. Of the figure, 84.75% was from carbon dioxide, 9.28% from methane, 4.81% from nitrous oxide and 1.16% from fluorinated gasses [14]. Because of the negative environmental effects of fossil fuels, the development of renewable and sustainable energy sources has become a primary priority for many nations. The push for renewable energy has been emphasized even more by the adoption of the Sustainable Development Goals (SDGs) by the United Nations in 2015 with SDG 7 aiming to provide access to affordable, dependable, sustainable, and modern energy for all [15].

Renewable energy sources can be used to produce energy again and again and these sources can provide energy free of air pollutants and greenhouse gases by emitting zero or nearly zero percent of these gases. Currently, the common sources of renewable energy are solar energy, hydropower, wind, biomass and geothermal. Solar energy is by far a good alternative to replace the fossil fuels as it is the most reliable and economical form of clean energy. The Earth receives 174 petawatts of incoming solar radiation at the upper atmosphere in a year. The total solar energy absorbed by the Earth's surface is approximately 3850 zettajoules per year, which is more energy in one hour than what the world uses in one year [16]. Africa has the best potential for solar energy development as it receives around 49% of the world's solar energy, with the sub-Saharan Africa having solar power potential of up to 1.5 million TWh a year [17]. It is interesting to note that South Africa is a potentially solar rich country with most areas receiving an average of more than 2 500 hours of sunshine per year, with an average solar-radiation level range between 4.5 and 6.5 kWh/m^2 in one day [18]. This represents a huge opportunity for the South African market to take advantage of and invest in solar energy as a renewable source of energy.

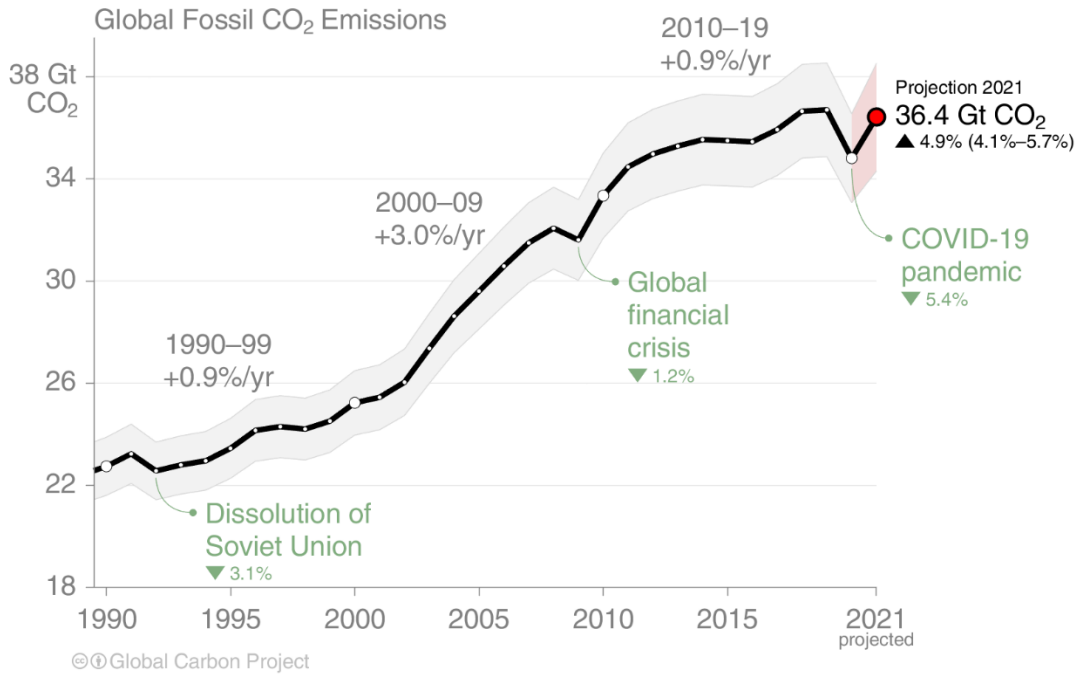

Fig. 1.1: Global energy-related carbon dioxide emissions, 1990-2021 [9].

Solar energy involves the conversion of energy from sunlight into electricity, either directly, indirectly or a combination of both. Of the solar energy harvesting methods currently known; solar thermal collectors, photovoltaic systems, biofuels (natural photosynthesis) and artificial photosynthesis, the photovoltaic cells are currently thought of as the best to convert the solar energy directly into electrical energy. A solar cell, or photovoltaic cell, is an electrical device that converts the energy of light directly into electricity by the photovoltaic effect, which is a physical and chemical phenomenon [19, 20]. Solar cells are divided into three generations based on the semiconducting material they are made from, **Fig. 1.2.**

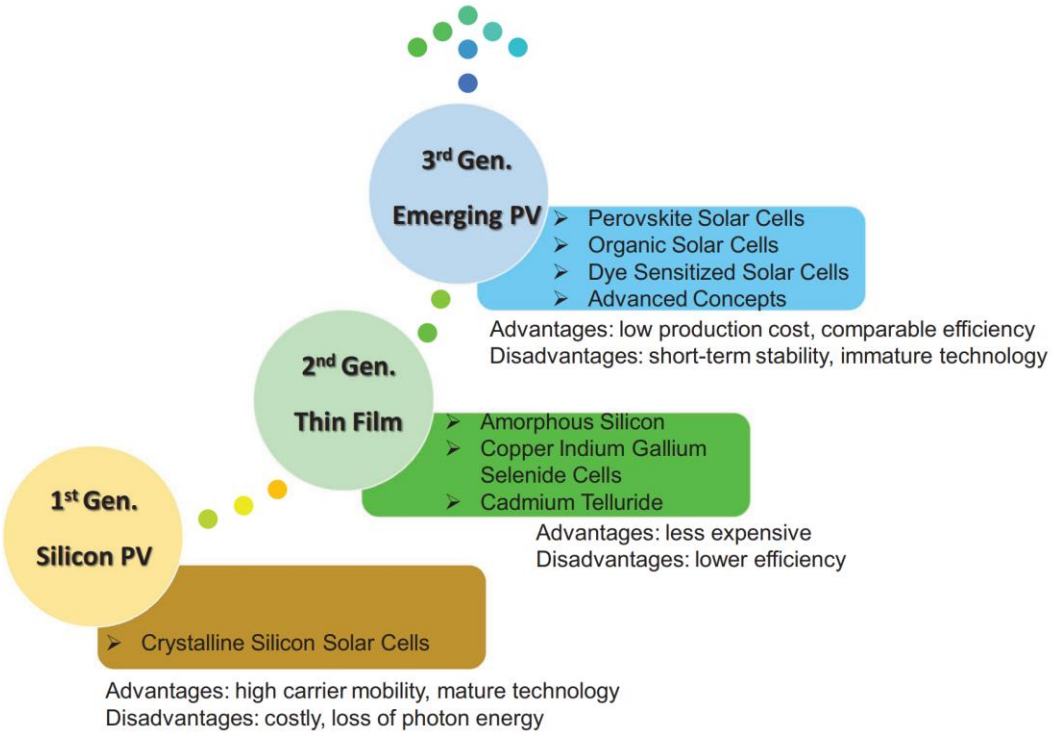

Fig. 1.2: Three generations of solar cell technology [20].

Dye-sensitized solar cells (DSSCs) have attracted much attention due to their simple and low-cost fabrication processes, versatility (meaning they may be integrated in a wide range of goods), and environmental friendliness [21]. Great efforts have been made to improve the technology of the DSSC in just over three decades since it was first created, and its multicomponent structure gives it an advantage because it permits individual elements of the device to be easily modified. A typical

DSSC consists of three main parts: A dye-sensitized TiO_2 photoanode, an electrolyte containing the redox couple (I_3^- /I^-), and a counter electrode (CE) that is a conductive substrate supported on electrocatalytically active materials [22, 23]. Currently, platinum (Pt) is the most useful CE in DSSCs; however it corrodes when exposed to an iodide-based electrolyte and is diminishing in its reserve, hence there is a need to explore Pt-free materials for the CE in DSSCs for future large-scale fabrication [24, 25].

1.2 Problem Statement

Electricity is critical to any country's economic development and reliance on a single source of electricity generation, such as coal combustion, is insufficient to meet the global energy demands owing to depletion of the resource over time. South Africa and other countries around the world are increasingly taking measures to research and use renewable energy sources to improve energy security, encourage economic growth and respond to the environmental challenges particularly associated with climate change. Solar energy is the most abundant energy resource on earth as it can be captured and used as an environmentally friendly renewable energy source. Solar panels (solar cells are a component of the panel) are available commercially but are expensive and have lower efficiencies than traditional electricity generating technologies. However, DSSCs demonstrate specific advantages over other photovoltaic devices, because of their low cost and simple fabrication procedures, environmental friendliness, transparency, and good plasticity [26]. However, the challenge is in the low efficiencies of the DSSCs and the choice of materials used such as the use of Pt as the counter electrode (CE) material. Alternative materials are now being explored to address the above-mentioned challenges, including transition metal chalcogenides, synthesized using the single-source precursor method as opposed to the conventional dual precursor method which usually results in synthesized nanoparticles with impurities and/or defects.

1.3 Rationale

Dye-sensitized solar cells have emerged as a viable alternative to Si-based PV systems due to their low cost of manufacture, low toxicity, and ability to perform in low-light conditions. The main disadvantage of DSSCs is their low efficiency when compared to silicon solar cells. An efficiency of 13% has been reported, which is lower than the 26% efficiency of silicon solar cells [27, 28].

Improving the efficiency and stability of the DSSCs is the major challenge most researchers are currently trying to resolve. Due to its good catalytic activity, platinum has been widely employed in the fabrication of DSSC counter electrodes up to date. Because platinum corrodes in the presence of the iodine-triiodide electrolyte, one way to improve the device's stability is by modifying the counter electrode through the use of other materials with qualities close to those of platinum. In this work, we propose using gold (I) sulphide nanostructures as the counter electrode material in place of the typically used platinum. Furthermore, to maintain the cost-effectiveness of DSSCs, we present a cheaper colloidal synthetic technique for producing gold (I) sulphide nanostructures from a single-source precursor as opposed to the typically used exfoliation method for 2D materials or dual precursor method. The single-source precursor method involves the decomposition of a molecular precursor, usually organometallic molecules to form the desired products. The single-source precursor method possesses an advantage over the dual precursor method due to its ease of separation of nanocrystalline material, better control over the size and shape of the nanoparticles, the eco-friendly nature of the process, use of low temperatures and its insensitivity to air and moisture as the method avoids introduction of precursors once the reaction has started [29]. While gold is generally expensive, the use of the sulphide form result in use of 46% of gold. To add on, South Africa is one of the major gold-producing countries in the world; it is therefore in the country's best interest to explore the beneficiation of this mineral which could ultimately enhance the economy of the country. South Africa is currently experiencing a downturn in gold mining, and this has profound environmental and socioeconomic impacts. For example, businesses that offer services to mines (e.g., engineering companies) or mine workers and their families (e.g., local transportation operations) have been forced to close [30]. It is therefore important that the country begins to focus on mineral beneficiation not just to improve the mining sector's profitability but also to address the country's energy crisis.

1.4 Aims and Objectives

The aim of this project was to focus on the colloidal synthesis of Au_2S nanostructures from a single-source precursor method and to use various characterization techniques to understand the synthesized nanostructures. Furthermore, the aim was to also investigate the electrocatalytic capabilities of Au_2S nanostructures to use them as a counter electrode in DSSCs. The following objectives were identified to achieve the above-mentioned aims:

- Synthesis and characterization of gold-sulphide complexes to be used as single-source precursors.
- Synthesis and characterization of Au_2S nanostructures from the single-source precursor.
- Investigate the effect of various reaction parameters such as reaction time, reaction temperature, precursor source and precursor concentration on the properties of the Au_2S nanostructures.
- Fabrication and characterization of CEs using Au_2S nanostructures.
- Evaluation of the performance of the DSSCs using Au_2S CEs.

1.5 References

[1] S. Pachauri, A. Brew-Hammond, D.F. Barnes, D.H. Bouille, S. Gitonga, V. Modi, G. Prasad, A. Rath, H. Zerriffi, T. Dafrallah, C. Heruela, F. Kemausuor, R. Kowsari, Y. Nagai, K. Rijal, M. Takada, N. Wamukonya, J. Sathaye, *Global Energy Assess*, (2012) 1401–1458.

[2] Z. Asghar, Econpapers.Repec.Org. 8, 44 (2008)

[3] J.J. Buonocore, E. Choma, A.H. Villavicencio, J.D. Spengler, D.A. Koehler, J.S. Evans, J. Lelieveld, P. Klop, R. Sanchez-Pina, *Palgrave Communications*, 5 (2019) 1–14.

[4] F. Perera, *International Journal of Environmental Research*, 15 (2018).

[5] International Energy Agency, *Global Energy Review*, 2020 (2021) 1–36.

[6] O. Edenhofer, R. Pichs-Madruga, Y. Sokona, E. Farahani, S. Kadner, K. Seyboth, A. Adler, I. Baum, S. Brunner, P. Eickemeier, B. Kriemann, J. Savolainen, S. Schlömer, C. von Stechow, T. Zwickel and J.C. Minx, *Intergovernmental Panel on Climate Change*, (2014) 1-1454.

[7] International Energy Agency, World Energy Outlook Special Report (2025) 1–200.

[8] R.J. Zedalis, *International Energy Agency*, (2017) 1-29.

[9] R. Andrew, G. Peters, (2021), https://zenodo.org/record/5569235#.Yh5L5OhBw2w accessed on 1 March, 2022.

[10] O. Awojobi, *Journal of International Academic Research for Multidisciplinary*, 5 (2017) 1–52.

[11] United Nations Fact Sheet on Climate Change - Africa, (2006).

[12] US Department of energy, (2011), http://cdiac.ornl.gov/trends/emis/tre_afr.html, accessed on 2 March 2022.

[13] F.V. Bekun, F. Emir, S.A. Sarkodie, *Science of the Total Environment*, 655 (2019) 759–765.

[14] Department of Forestry Fisheries and the Environment: National GHG inventory report: Republic of South Africa, 2000-2017. Gov. Gaz. (2020)

[15] A. Guterres, *United Nations Publication, Department of Economic and Social Affairs* (2020) 1–64.

[16] J. Wu, Z. Lan, J. Lin, M. Huang, Y. Huang, L. Fan, G. Luo, Y. Lin, Y. Xie, Y. Wei, *Chemical Society Reviews*, 46 (2017) 5975–6023.

[17] Helioscsp, https://helioscsp.com/it-is-time-for-africa-to-tap-the-solar-power/ accessed on 1 March 2022.

[18] Renewable energy department of South Africa, http://www.energy.gov.za/files/esources/renewables/r_solar.html accessed on 1 March, 2022.

[19] A. M. Bagher, *Ameriacn Journal of Optics and Photonics*, 3 (2015) 94-113.

[20] H.D. Pham, T.C.J. Yang, S.M. Jain, G.J. Wilson, P. Sonar, *Advnaces in Energy Materials*, 10, (2020) 1903326.

[21] M. Yilmaz, S.H. Hsu, S. Raina, M. Howell, W.P. Kang, J.H. Huang, *Journal of Renewable and Sustainable Energy*, 10 (2018), 063501.

[22] J. Guo, S. Liang, Y. Shi, C. Hao, X. Wang, T. Ma, *Physical Chemistry Chemical Physics*, 17 (2015) 28985–28992.

[23] H. Yuan, L. Kong, T. Li, Q. Zhang, *Chinese Chemical Letters*, 28 (2017) 2180–2194.

[24] S. Thomas, T.G. Deepak, G.S. Anjusree, T.A. Arun, S.V. Nair, A.S. Nair, *Journal of Materials Chemistry A*, 2 (2014) 4474–4490.

[25] Y. Xing, X. Zheng, Y. Wu, M. Li, W.H. Zhang, C. Li, *Chemical Communications*, 51 (2015) 8146–8149.

[26] K. Ranabhat, L. Patrikeev, A.A. Revina, K. Andrianov, V. Lapshinsky, E. Sofronova, *Journal of Applied Engineering in Science*, 14 (2016) 481–491.

[27] A. Blakers, N. Zin, K.R. McIntosh, K. Fong, *Energy Procedia*, 33 (2013) 1–10.

[28] L.C. Andreani, A. Bozzola, P. Kowalczewski, M. Liscidini, L. Redorici, *Advances in Physics X*, 4, (2019) 1548305.

[29] N. Maiti, S.H. Im, Y.H. Lee, C.H. Kim, S. Seok Il, *CrystEngComm*, 13 (2011) 3767–3772.

[30] C. Strambo, A. Atteridge, *Stockholm Environment Institute*, (2021) 1–8.

[31] A. Amiri, M. Naraghi, G. Ahmadi, M. Soleymaniha, M. Shanbedi, *FlatChem*, 61 (2018) 030047.

CHAPTER 2

Literature review

2.1 Introduction to metal chalcogenides

2.1.1 Transition metal chalcogenides

Transition metal chalcogenide (TMC) nanoparticles (NPs) have sparked a lot of interest in recent years, with many researchers focusing on their fascinating features and wide range of applications, which include fuel cells, solar cells, sensors, field effect transistors, light-emitting diodes, and supercapacitors [1–3]. These nanoparticles have at least one dimension in the range 1-100 nm and have fascinating features that are due to their optical, electronic, catalytic, and magnetic properties which are different from their bulk material because at this level quantum effects are significant [4, 5]. The structure of the bulk material is made up of overlapping atomic orbitals that form bonding and anti-bonding molecular orbitals. The bonding molecular orbitals make up the valence band (VB) and the anti-bonding molecular orbitals make up the conduction band (CB). The conduction and valence bands are separated by an energy gap, known as the band gap energy (E_g) [6] as shown in **Fig. 2.1(a)**. The E_g is the minimum energy required to excite an electron from the VB into the CB and is specific for each material and for the same material, the E_g for the bulk material is different from that of its nanoparticles. The transfer of electrons between the valence band and the conduction band can either be direct or indirect. A direct band-gap material is one where the maximum energy level of the valence band aligns with the minimum energy level of the conduction band with respect to momentum, **Fig. 2.1(b)**. They are said to be materials that permit electrons to use the direct path with the least energy difference between the valence band and the conduction band without changing momentum [7]. An indirect band-gap material on the other hand is one in which the maximum energy level of the valence band and the minimum energy of the conduction band are misaligned with respect to momentum, **Fig. 2.1(b)**. The electrons in such materials are said to be forbidden to follow the route of least energy difference between the two bands without a change in momentum [7]. Quantum confinement happens when at least one of the dimensions of the NP is decreased to the same order as the Bohr exciton radius of the material and thus the exciton properties are modified. Depending on the dimension of the confinement, three

types of confined structures are defined: zero-dimensional (e.g., quantum dots), one-dimensional (quantum wires e.g., nanorods) and two-dimensional (quantum wells e.g., nanosheets) [6, 8].

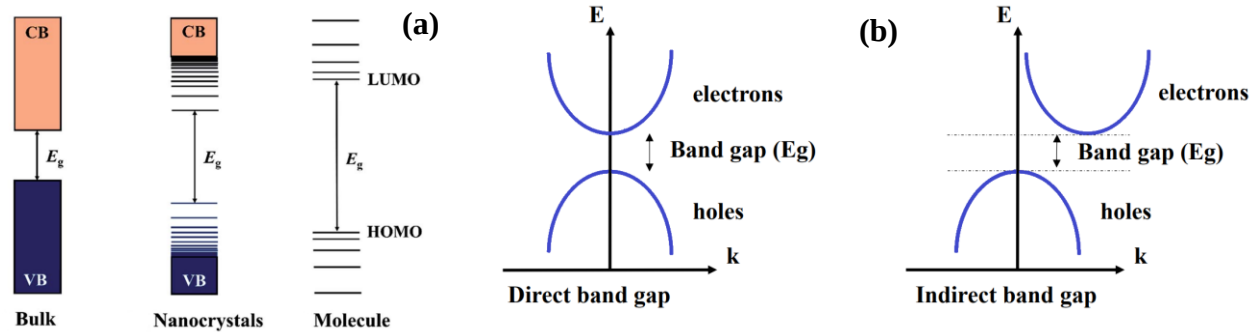

Fig. 2.1: (a) A comparison of the electronic energy levels of a bulk material and the nanoparticles and (b) direct and indirect band gap materials [5, 6].

There are varieties of transition metal chalcogenide nanoparticles with some adopting a layered structure that has chemical and electronic properties that differ from bulk semi-conductors. They have the general formula M_yX_z where M is a transition metal (e.g., Mo, W, Nb) and X is a chalcogen (S, Se, Te). The chemistry of metal-chalcogen bonds was widely researched for the chalcogen sulphur in the early 1970s and later for selenium and tellurium as well [1, 9]. **Fig. 2.2** shows the common transition metals and the chalcogen atoms.

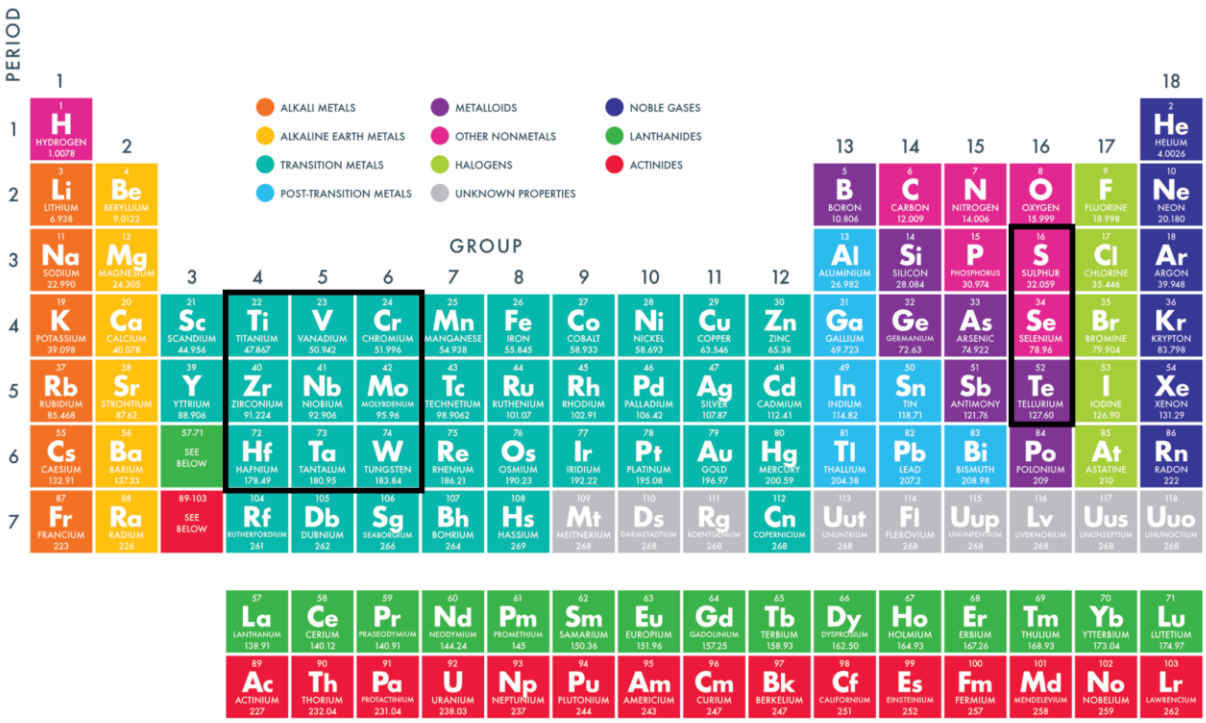

Fig. 2.2: Periodic table showing the transition metals and chalcogen atoms found in transition metal chalcogenides [9].

2.1.2 Quantum confinement effects

Quantum confinement is a concept that refers to the energy of confined electrons (electrons or electron hole pairs). The quantum confinement effect is observed when the size of the particle is too small to be comparable to the De Brogile wavelength of electrons in the conduction band, resulting in discrete levels of energy [5]. For any given semiconductor at low temperatures, the valence band contains most of the electrons while the conduction band has extremely few or none. Light absorption excites valence electrons to high density states in the conduction band only if incident photons transfer enough energy for electrons to overcome the energy barrier (E_g). The migration of electrons to the conduction band, leave holes in the valence band, and the charge carrier in semiconductor device recombines with the hole after the release of energy [8]. When the size of the semiconductor is drastically reduced, the charge carriers are limited within a potential well, which can be considered as a ‘particle in a box’, resulting in quantum effects [10, 11]. This means that the valence and conduction bands are split into quantized levels or discrete energy levels, rather than a continuous band as in the corresponding bulk material. The quantum

confinement effect has an impact on the properties of the nanoparticles as they tend to have unique optical and electronic properties that have the potential to enhance the power conversion efficiency of photovoltaic solar cells [5, 6]. This unique nature of the nanoparticles explains why they have greater energy electrons than the bulk materials. The result is that the bandgap exhibits size-dependent properties and eventually causes a blue shift in the emitted light as the particle's size is decreased. That is to say, the energy difference between the bands is increased with a decrease in particle size as shown in **Fig. 2.3**. The quantum confinement effect has been shown to contribute to the extension of the photovoltaic potential of low-bandgap semiconductors like PbS or PbSe (bandgaps of 0.41 and 0.27 eV respectively) by shifting their bandgap to an optimal value for high energy conversion efficiency [12, 13].

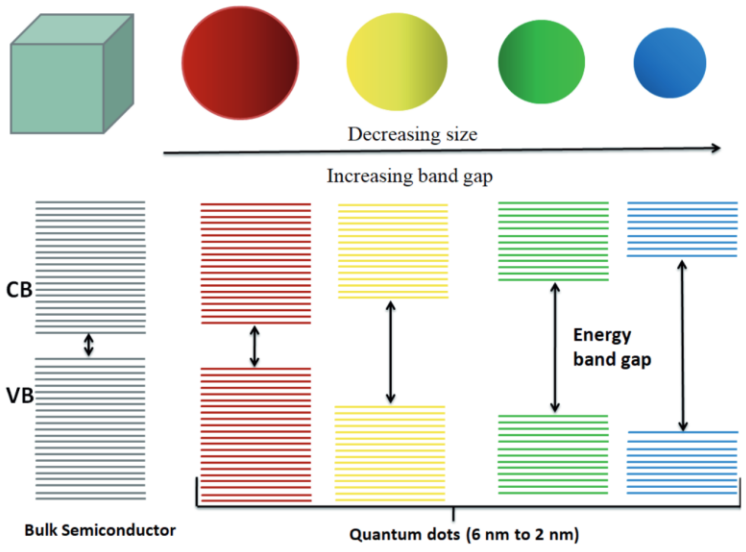

Fig. 2.3: An illustration of quantum confinement effects showing the increase in the band-gap energy as the size of the nanoparticles decreases [5].

2.1.3 Transition metal sulphides

Transition metal sulfide (TMS) nanoparticles have sparked a lot of interest among researchers because of their unique size-dependent optical, electrical, chemical, catalytic and mechanical properties that are different from the bulk material [14, 15]. TMSs are a class of inorganic binary materials having the general formula M_xS_y, (M = metal and S = sulphur). The M–S bond is considered a covalent bond because of the lower electronegativity value of sulphur (2.58) on the

Pauling scale. The increased covalent character of the M–S bond in M_xS_y binary compounds has significant implications on the TMS structures and chemical characteristics [16–18]. Transition metal monosulfides (M_xS) have a formal oxidation number of the metals as +2 while the d electron configuration changes from d^2 to d^{10}. Except for MnS, CuS, ZnS, and Au_2S, all other monosulphides crystallize in the NiAs related structure, **Fig. 2.4** [19–22]. MnS, ZnS, and Au_2S have the cubic rock-salt structure, zincblende structure and cubic phase structures respectively, but CuS has a unique hexagonal structure with copper being present in both the + 1 and +2 oxidation states, **Fig. 2.4**. Transition metal disulfides (M_xS_2) form layered compounds with monoatomic and diatomic anions. Each layer is made up of metal atoms sandwiched between two layers of sulphur chalcogen atoms (S-M-S), where the interlayer bonding is due to strong in-plane covalent bonding, while the layers are held together by weak van der Waals forces, **Fig. 2.5** [23–25].

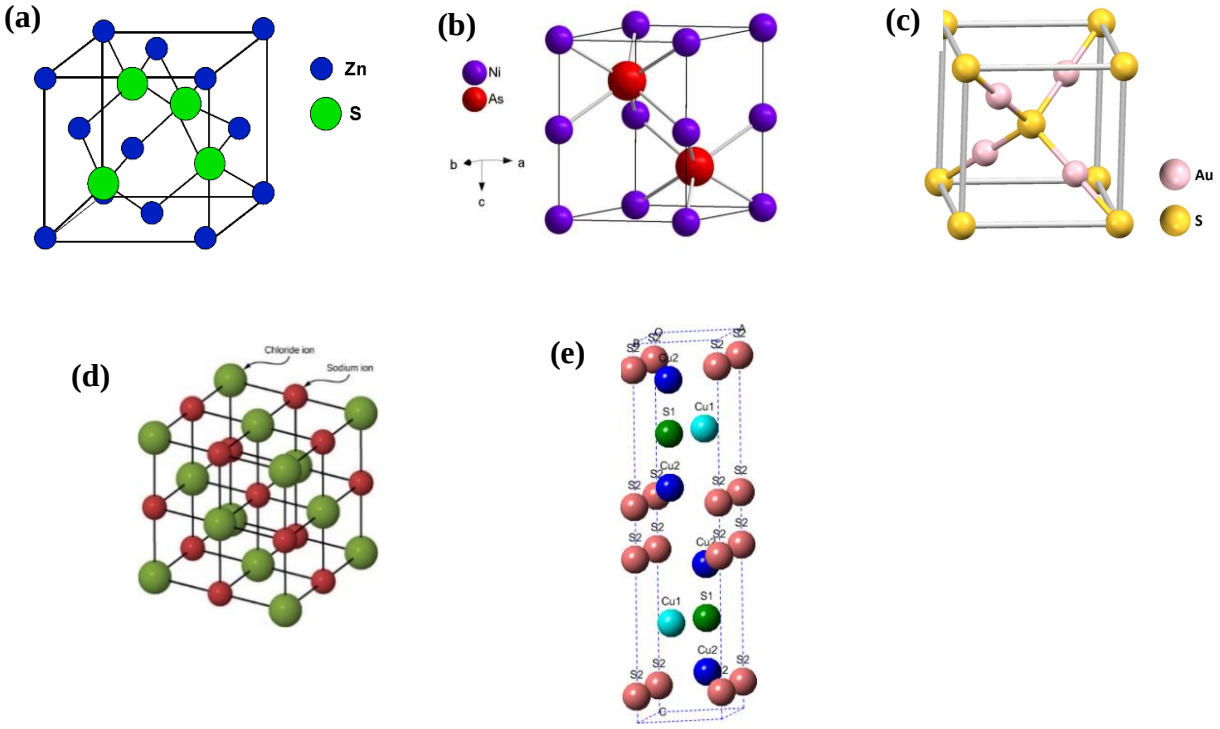

Fig. 2.4: Unit cell of (a) ZnS (b) NiAs, (c) Au_2S (d) MnS, (e) CuS [20–22].

Aside from mono- and disulphides, transition metals form sulfides with general formulae such as MS_3, $M_{1+x}S$, MS_{1+x}, and so on, as well as several other well-defined compounds with distinct characteristics [23]. TMS nanoparticles are important semiconductor materials with wide range of applications. Copper sulphide (CuS) nanoparticles, for example, are semiconductor materials with

increased conductivity at high temperature, excellent solar radiation absorbing properties and high-capacity cathode material in lithium secondary batteries. The band gap of CuS can be easily adjusted by altering the morphology, e.g., CuS microspheres have band gap of 2.08 eV, CuS nanoflakes have band gap of 2.16 eV and CuS nanoparticles have band gap of 1.88 eV. Because of these properties, CuS can be employed in light emitting devices, photocatalysis, solar cells and sensors to name a few [26–28]. Despite several research publications on different transition metal sulphides, their study is far from complete, as there are several materials still to be discovered and extensively investigated.

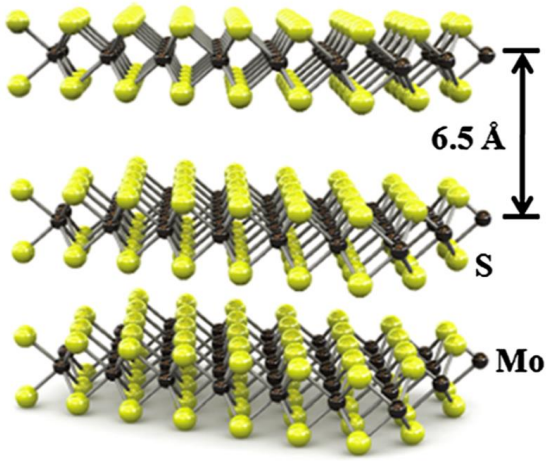

Fig. 2.5: The atomic structure of layered MoS_2, where the Mo atom is sandwiched between the S atoms and the distance between two layers is 6.5 Å [25].

2.1.4 Au_2S structure and properties

Gold (I) sulphide (Au_2S) is a simple binary solid with cuprite-type structure, space group Pn-3m (224), with lattice parameter $\alpha = 5.0443$ Å ($Z = 2$, $V = 128.36$ Å) [29, 30]. **Fig. 2.6** shows the crystal structure of Au_2S. The unit cell of Au_2S has S atoms at the corners of a simple cube with one S atom in the center surrounded by four Au atoms forming a linear geometry such that the S-Au-S bond angle is 180° and the distance between the Au and S atoms is 2.16 Å [31]. The structure is made up of a face-centered cubic (fcc) gold lattice and a body-centered cubic (bcc) sulphur lattice [29]. The chemical bonding in Au_2S can be explained with regards to the electronegativities of both atoms. The Pauling electronegativity of gold is similar to that of sulfur, (Au = 2.54 and S = 2.58), thus placing Au_2S in the covalent area of the van Arkel–Ketelaar triangle of bonding, **Fig. 2.7** [29, 32]. Because of the strong Au-S covalent bond, Au_2S is a stable 1D structure [33]. By

putting together, a simple Lewis model, Santamarıa-Perez and coworkers [29] suggest that Au–S bonds in bulk Au_2S are an average of two different types of single bonds (dative and shared) and the crystal's ground state is a combination of degenerate configurations with various spatial arrangements of these bonds, **Fig. 2.7**. In the Lewis dot diagram, the central atom, S, forms two dative bonds and two shared bonds with its four neighboring Au atoms. The character (dative or shared) of the rest of the bonds in the cell, and, by extension, the entire crystal, is determined by the distribution of these four bonds. If translational symmetry is applied, there are six different ways to arrange the bonds in the central atom, and hence six different ground-state configurations for this crystal. Because these two bonds are not equivalent (they have different bond strengths and lengths), then all degenerate electronic configurations contribute equally to the ground state of Au_2S, making the system multireference [29].

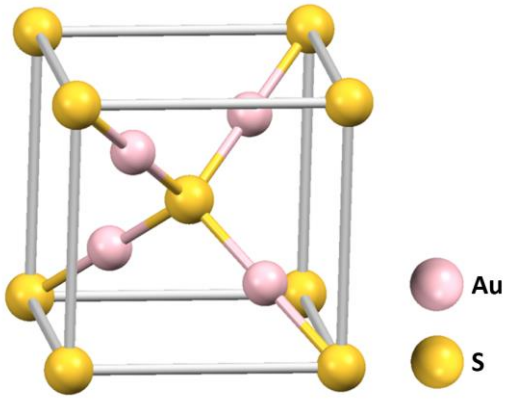

Fig. 2.6: Cubic unit cell of Au_2S.

Au_2S is a bulky covalent crystal that has been shown to exhibit p-type semiconductivity in the range 210-420 K [30]. However, the semiconducting properties of Au_2S is still a matter of controversy to date. According to Averitt and coworkers, [34] their theoretical calculations suggest that Au_2S has a band gap energy range of 1.3 to 2.6 eV. On the other hand, Morris et al., [31] suggested that Au_2S, like Cu_2S and Ag_2S, is an indirect semiconductor with a direct band gap of 1.8 eV and an indirect band gap of 0.5 eV. They further suggested that Au_2S nanostructures exhibit quantum confinement effects (i.e., blue-shift in the absorption spectrum) when they noticed a color change from brownish black (bulk) to yellowish-brown (nanostructures) when the nanostructures were filtered and collected for elemental analysis. On this basis, the Au_2S nanostructures show potential in various applications including photovoltaic cells.

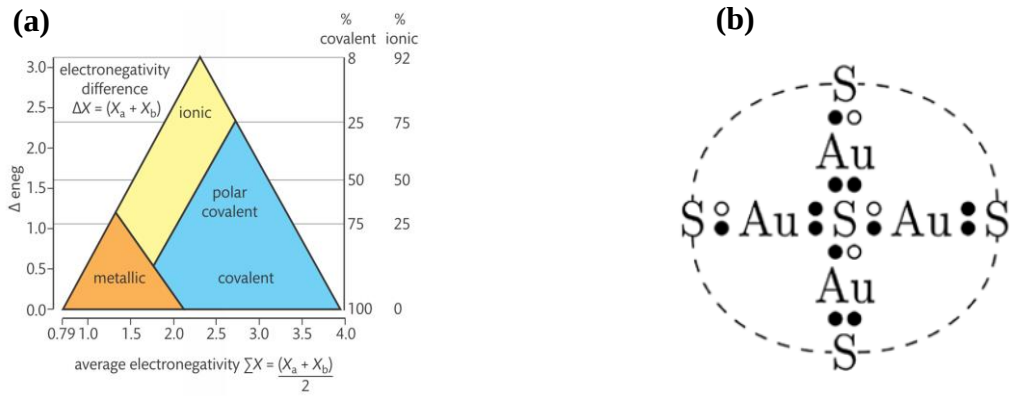

Fig. 2.7: (a) van Arkel–Ketelaar triangle of bonding, (b) Lewis dot diagram for bulk Au_2S [29, 32].

2.2 Synthesis of transition metal chalcogenides

The growing interest in transition metal chalcogenides has prompted researchers to investigate a variety of synthetic techniques for producing these nanomaterials, some of which are addressed in this section. There are two general approaches for the synthesis of nanomaterials: the top-down and bottom-up approaches. In the top-down approach, the bulk material is broken down into nanosized structures or particles and in the bottom-up approach, nanoparticles are built up from the bottom, atom-by-atom, molecule-by-molecule, or cluster-by cluster [35–37] as shown in **Fig. 2.8.**

2.2.1 Top-down synthesis approaches

In the top-down approach, there is either removal or division of bulk material (physical processes) to produce the desired nanoparticles with the appropriate properties. The following are some of the most common approaches utilized in this approach; sputtering, mechanical or ball milling and ultrasonication induced liquid phase exfoliation. Despite that the top-down approaches are simple to use, they are ineffective in producing suitable particle size and shape [37, 38].

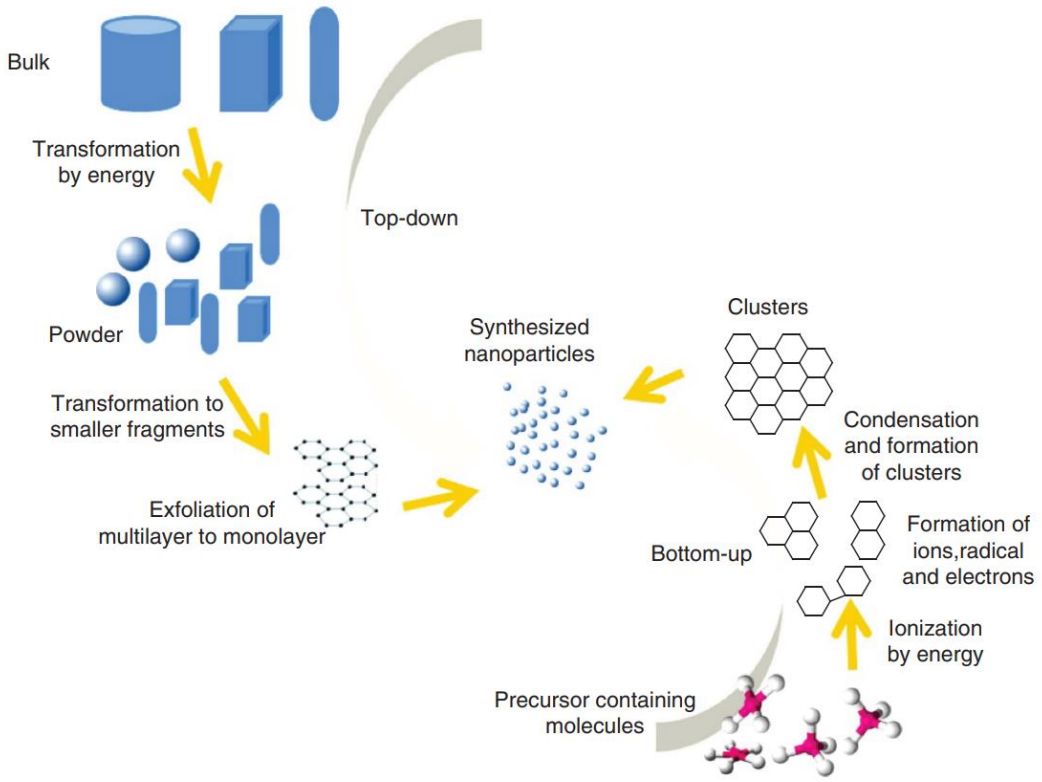

Fig. 2.8: Schematic illustration of the bottom-up and top-down approaches of NPs synthesis [38].

2.2.1.1 Ultrasonication induced liquid phase exfoliation (UILPE)

This method involves sonication of the bulk material in various liquid media to obtain the required nanomaterials [39, 40]. With this method, two factors have a significant impact on the exfoliation process of the bulk material. The first factor is the energy input to the bulk material by the bath sonication, as the material is effectively exfoliated upon exposure to the ultrasonic waves. Shear forces are created from the ultrasonic waves that can generate a high amount of energy with the bubbles in the liquid media that can then change the main structure of bulk material by weakening the intermolecular forces. This weakening of the bond eventually increases the material's interlayer spacing, allowing the stacked sheets to be exfoliated [40–42]. The second essential aspect is the liquid media used (ionic liquids, aqueous solutions of stabilizers, and organic solvents). The liquid media has two main functions; overcome the cohesive energy between the layers in the bulk material and prevent the nanosheets from aggregation [39, 41]. This method has been successful

for the synthesis of graphene sheets [37, 41]. An overview of the liquid phase exfoliation is shown in **Fig. 2.9**.

2.2.1.2 Sputtering

Sputtering is more common among the top-down approaches because of its non-thermal vaporization process [37]. Sputtering is a physical process in which atoms in a solid-state (target material) are ejected by bombardment of high energy ions and pass into the gas phase and are deposited on a substrate surface where they grow into a film [37]. In this approach, two electrodes are employed, one for the target material and the other for the substrate, with inert gas ions in between [37, 43] **Fig. 2.9**. Sputtering is classified as direct current (DC) sputtering, radio frequency (RF) sputtering, or magnetron sputtering, depending on the process of ion formation and the focusing of the ions [43]. In the direct current (DC) sputtering method, a negative voltage is applied to the target material and a positive voltage is applied to the substrate. Once the required vacuum level is obtained, the inert gas is introduced, usually Argon (Ar). Because of the large electric field between the electrodes, energetic electrons collide with the gas, forming ions. These ions then come into contact with target material, causing nanoclusters to sputter and be deposited on the substrate [37, 43]. As a result, DC-sputtering is limited to conducting materials such as metals and doped semiconductors [44, 45]. On the other hand, radio frequency (RF) sputtering method uses high frequency, mostly 13.56 MHz, to adequately ionize the gas and it is typically used when the target is insulating or near insulating materials [43]. In the magnetron sputtering method, a magnetic field is applied simultaneously with the electric field created by DC/RF sputtering to improve the impact of ionization and the focusing of the ions toward the target material [43, 44, 46].

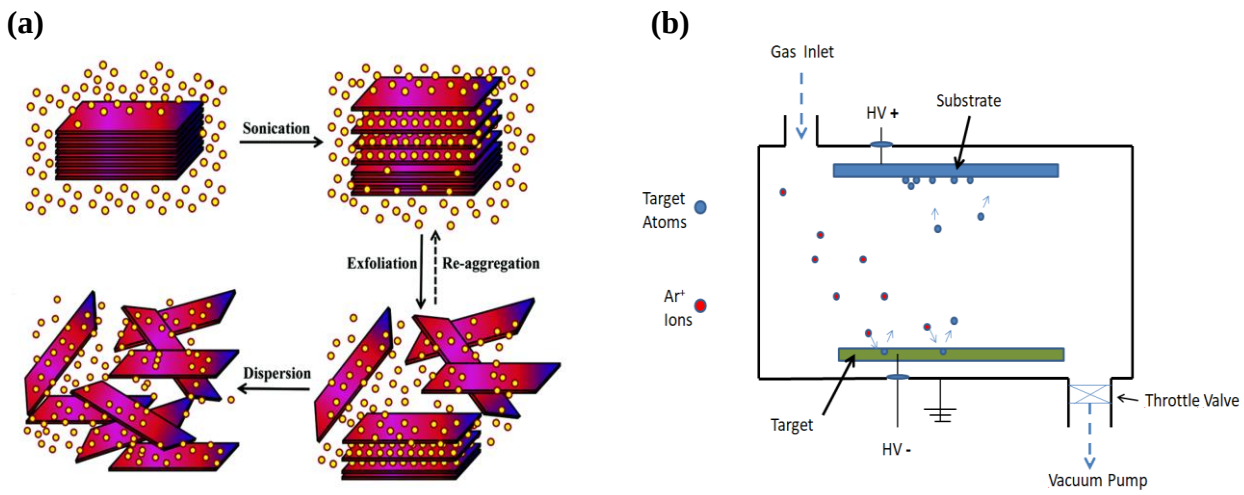

Fig. 2.9: (a) Hierarchal stages involved in UILPE (b) Sputter deposition of target material on the substrate [40, 46].

2.2.2 Bottom-up synthesis approaches

The bottom-up synthesis approach involves putting together or self-assembly of atoms and molecules to produce the desired nanomaterial with well-defined structure, size, and chemical content [37, 43]. The bottom-up approaches are mainly regarded as wet chemical synthesis methods. Examples include but are not limited to; chemical vapor deposition (CVD), sol-gel, microwave assisted, and colloidal synthesis. The advantages of the bottom-up approaches are; they are simple approaches that require less instrumentation than physical methods, synthesis can be done at either low or high temperatures, and by manipulating the synthesis parameters, a higher quantity of material can be synthesized at once, with a variety of sizes and shapes [43, 47].

2.2.2.1 Chemical vapour deposition (CVD)

This method involves either the dissociation of a gaseous chemical and/or chemical reactions between gaseous precursors when heated, bombarded by photons, or exposed to a plasma [48, 49]. The product of the reaction is a thin layer of film on a heated substrate that is etched and put to good use [37]. Depending on the source of energy required to initiate and maintain the deposition reaction, there are various types of CVD deposition techniques; thermal layer deposition, atomic laser deposition, or plasma assisted deposition. The CVD process takes place in a vacuum chamber with pressures ranging from the atmospheric-pressure (1 Torr) to ultrahigh-vacuum (100 Torr) [37,

48]. The following are the main steps that occur in a typical CVD process: (1) transport of reacting gaseous precursors to the substrate's surface, (2) adsorption of the precursors on that surface, (3) heterogeneous surface reaction catalyzed by the substrate's surface, (4) surface diffusion of the precursors to growth sites, (5) nucleation and growth of the film on the substrate, and (6) gaseous reaction desorption of the products and transport of these products from the substrate surface [37, 48, 50]. The main CVD process parameters such as temperature, reactant gas concentration, total gas flow and pressure must be controlled to generate predefined nanomaterial [43, 48]. **Fig. 2.10** shows a typical thermal CVD schematic diagram.

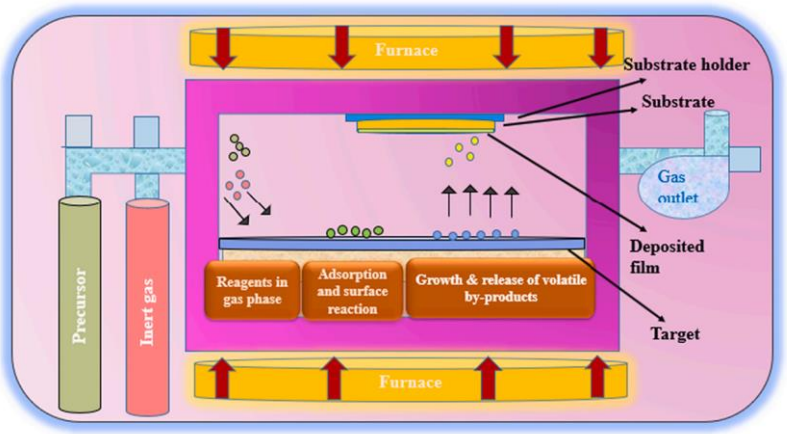

Fig. 2.10: Schematic of a thermal-assisted CVD system [35].

2.2.2.2 Sol-gel

The sol-gel method is a wet chemical approach for the synthesis of different nanostructures, particularly metal oxide nanoparticles [51, 52]. The molecular precursor (typically metal alkoxide) is dissolved in water or alcohol to form a sol (colloidal particles in solvent) that is then transformed to a gel (an integrated network) via hydrolysis and polycondensation reactions. Because the gel resulting from the hydrolysis process is in solution, it must be dried by using various methods to obtain the nanomaterials with the desired qualities and properties. The sol-gel method is a cost-effective technology with good control over the chemical composition of the products due to the low reaction temperatures used [51–53]. The sol-gel method involves three stages: hydrolysis, condensation, and gelation. **Fig. 2.11** is a schematic of all the stages involved in the sol-gel method.

Stage 1: Hydrolysis

Hydrolysis involves the attachment of the hydroxy ions to the metal atoms of the precursor metal alkoxide [52, 54]. An example of a silicon metal alkoxide hydrolysis reaction is shown in equation 2.1.

$$Si(OR)_4 + HOH \longrightarrow HO\text{-}Si(OR)_3 + ROH \quad (2.1)$$

Stage 2: Condensation

The condensation process liberates water/alcohol molecules to create larger molecules by a process called polymerization [52, 54]. Equation 2.2 expresses a condensation reaction with the release of a water molecule.

$$(OR)_3\text{-}Si\text{-}OH + OH\text{-}Si\text{-}(OR)_3 \longrightarrow [(OR)_3Si\text{-}O\text{-}Si(OR)_3] + H_2O \quad (2.2)$$

Stage 3: Gelation

The last step is a polycondensation reaction where a gel (an inorganic continuous network with a liquid phase) is formed. Gel formation is aided by either van der Waals forces, hydrogen bonds or covalent bonds [52, 54].

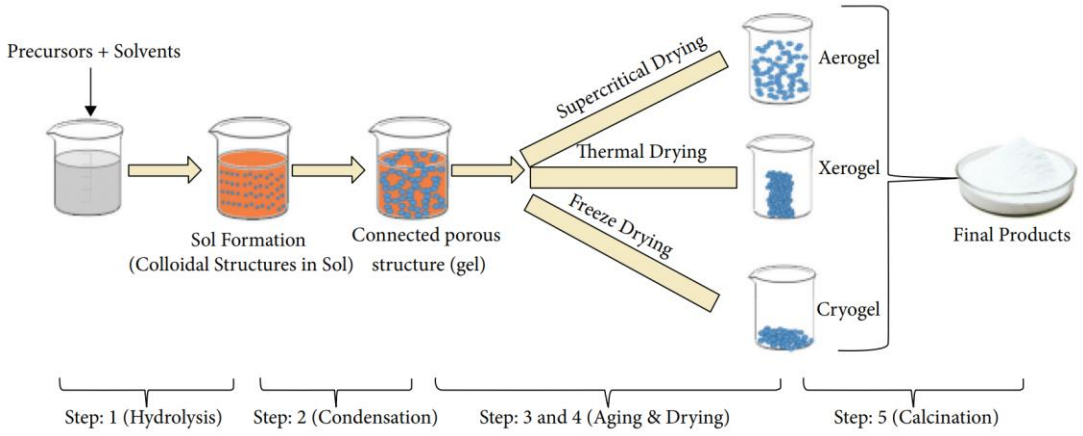

Fig. 2.11: Schematic of the sol-gel process showing all the stages [51].

2.2.2.3 Colloidal synthesis

Colloidal synthesis, among the numerous bottom-up approaches, has significant benefits in the controlled synthesis of diverse nanoparticles where the nanoparticles precipitate out a homogenous solution [55]. The colloidal synthesis method uses a variety of chemical procedures such as thermal decomposition and chemical reduction to produce the atoms required from various precursors to synthesize the desired nanoparticles. The thermal decomposition approach uses organometallic precursors that are decomposed in high boiling organic solvents [56]. The colloidal synthesis approach was adapted from the work of Chestoney et al., who were able to synthesize transition metal chalcogenide semiconductor nanoparticles, however the nanoparticles were not monodispersed [57, 58]. To best explain the fundamental processes involved in colloidal synthesis (nucleation and growth), the theory described by the work of LaMer and Dinegar is used [56, 59].

2.2.2.3.1 Nucleation

The first step in the formation of nanoparticles is the nucleation process, which can be homogeneous or heterogeneous. It is the process by which a small number of ions, atoms, or molecules aggregate from a liquid or gas phase to form a nucleus around which other particles can agglomerate together to form a crystal [60, 61]. The nucleation process is described by the classical nucleation theory, which is a theoretical model first developed by Becker and Döring in the 1930s [56]. The theory describes nucleation as a thermodynamic system that strives to minimize the Gibbs free energy in the formation of the nucleus [56]. The nucleation process can either be homogeneous of heterogenous. Homogeneous nucleation involves the spontaneous and random creation of a nucleus from a supersaturated solution without the necessity for a nucleation site, whereas the heterogeneous nucleation necessitates the presence of a nucleation site [56, 62]. The process of homogenous nuclei formation can be thought of as a thermodynamic process by looking at the total free energy (Gibbs free energy) of a nanoparticle which is defined as the sum of the surface free energy and the bulk free energy [60]. The Gibbs free energy of a nucleus is defined as the sum of a negative and a positive term. The negative term denotes the energy of a favorable bonding between a monomer and a cluster, or potentially between two monomers, resulting in a reduction in Gibbs bulk free energy. On the other hand, the positive term describes an increase in the Gibbs free energy which is because of the unfavorable bonding of a monomer [56, 60]. The Gibbs free energy of a spherical cluster is expressed as:

$$\Delta G = -\frac{4}{3}\pi r^3 \, |\Delta G_v| + 4\pi^2 \gamma \tag{2.3}$$

Where r is the radius, $|\Delta G\, v|$ is the difference in Gibbs bulk free energy per unit volume, and γ is the surface energy per unit area.

A plot of the Gibbs free energy of the cluster with respect to the radius in Fig. 2.10 shows the effect of the surface energy on the positive term and the effect of the bulk free Gibbs energy on the negative term. The figure also shows that there is a maximum Gibbs energy at a critical cluster radius represented as r_c, (the smallest radius of a particle that is stable in solution) whereby the corresponding energy barrier is called the activation energy [60]. If the cluster's radius is less than r_c, the cluster of particles is unstable and will re-dissolve in solution. On the other hand, if the cluster's radius is bigger than r_c, then the particle cluster is stable, and growth is favored [60].
The critical radius is expressed as:

$$r_c = \frac{2\gamma}{|\Delta G_v|} \tag{2.4}$$

By substituting r in equation (2.3) with r_c from equation (2.4), the expression for the critical free energy ΔG_c is given as:

$$\Delta G = \frac{16\pi\gamma^3}{|\Delta G_v|^2} \tag{2.5}$$

The rate of nucleation $J(T, \Delta G_c)$ can be expressed by the Arrhenius equation where the energy barrier for nucleation is related to the activation energy as shown in equation 2.6.

$$J(T, \Delta G_c) = A\, exp\left(\frac{-\Delta G_c}{k_B T}\right) \tag{2.6}$$

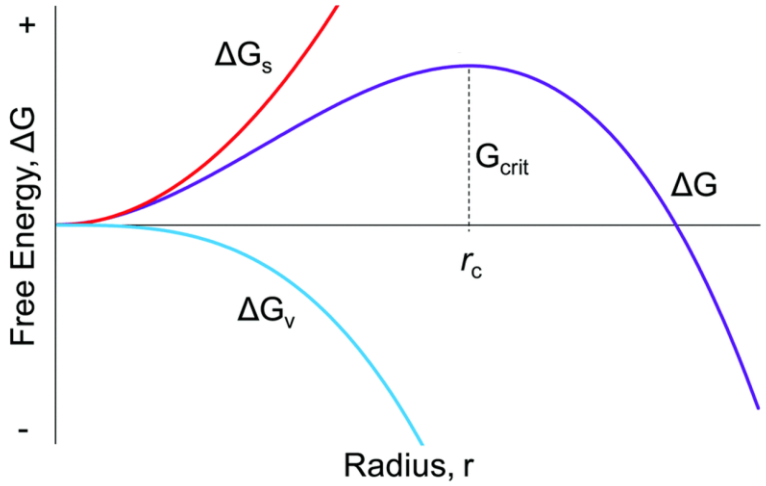

Fig. 2.12: A plot of the Gibbs free energy against the radius of the clusters [63].

In the 1950s, LaMer built on Becker and Doring's approach by applying classical nucleation theory to nanoparticle synthesis and forming the theory of burst nucleation [59, 64]. LaMer showed that in the burst nucleation process, nuclei are formed at the same time due to homogeneous nucleation and subsequently grow without additional nucleation [56, 63, 65]. The nucleation process can be explained in three stages as depicted in **Fig. 2.13**.

Stage 1: The first step involves the decomposition of the precursor, which leads to the formation of monomer, followed by an increase in monomer concentration until the solution reaches a critical supersaturation point (C_s).

Stage 2: The saturation increases and reaches a level (C_{min}) where the energy barrier (activation energy) for nucleation can be overcome resulting in a rapid self-nucleation (the burst nucleation).

Stage 3: In the last step, the nucleation process stops as the monomer concentration falls lowering the supersaturation threshold. At this point, the monomers diffuse to the nucleation site and the nuclei begin to grow.

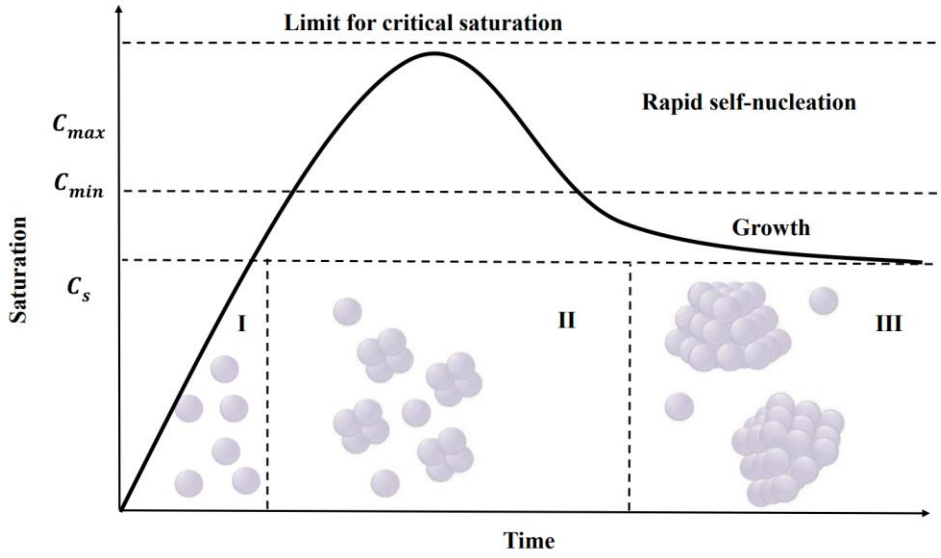

Fig. 2.13: A graphical illustration of LaMer and Dinegar nucleation [56].

The LaMer model remains the only widely accepted model for explaining the general mechanism of nanoparticle formation, however, the model is unable to explain the formation of nanoparticles with broad size distributions [56]. It merely defines the nucleation process, which is followed by the growth of stable nuclei, but the characteristics of the growth are undefined. Thus, theoretical models for the actual growth of the nuclei forming the nanoparticles are required to explain the final size distribution. The Ostwald's ripening process can be used to explain such nanoparticle growth in colloidal synthesis that results in a broad size distribution.

2.2.2.3.2 The Ostwald ripening process

The Ostwald ripening process was discovered by Wilhelm Ostwald in the 1900s, when he was investigating the influence of the size of crystals on their solubility, and he discovered that smaller crystals have higher solubility as compared to larger crystals [66, 67]. Ostwald ripening, named after Wilhelm Ostwald, is a heterogeneous growth process in which smaller crystals in solution re-dissolve and deposit on the surface of larger particles. The driving factor behind this phenomenon is that smaller particles are thermodynamically unstable as they have more interfacial energy resulting in a higher overall Gibbs energy as compared to larger particles [66, 68]. The continued growth of the larger nanoparticles at the expense of the smaller one's results in a system with a broad range of size distribution, which is an undesirable process if a uniform size distribution of

nanoparticles is required. As a result, the burst nucleation stage is considered critical in colloidal synthesis.

2.2.2.3.3 Factors influencing morphology and size in colloidal synthesis

There are several factors that affect the synthesis of nanoparticles that then results in nanoparticles of different morphology and size. These include reaction parameters such as temperature, concentration of the precursors used, the type of precursors used, the capping agents or coordinating ligands used, the reaction time and the protocols that are followed for the synthesis process [69]. An overview of the factors explored in this study and their impact are discussed below.

2.2.2.3.3.1 The role of capping agents or coordinating ligands

In colloidal synthesis, the reactions are normally conducted in organic solvents that bind to the surface of the nanoparticles thereby stabilizing the nuclei and larger nanoparticles against aggregation by a repulsive force, and which typically influence the growth of the nanoparticles in terms of rate, final size, or geometric shape [70, 71]. The ligand molecules are bound to the particle surface by an attractive interaction, such as chemisorption, electrostatic attraction, or hydrophobic interaction, which is most typically given by the ligand molecule's head group. The identity of the head group is critical in nanoparticle synthesis because different functional groups have different affinities to certain crystal facets [70]. The organic solvents or ligands used have an electron-donating head group, such as an amine ($-NH_2$), hydroxy (-OH), thiol (-SH) or phosphine ($-PR_3$) and usually undergo dynamic binding and unbinding processes [70, 72]. As a result, the ligand molecules can be removed by excessive washing, or they might be replaced by another incoming ligand with greater affinity for the surface of the nanoparticles. The properties of the synthesized material are also influenced by the strength of the bond formed between the coordinating ligands and the nanoparticles. Strongly binding molecules form a dense layer that stabilizes the nanoparticles better, thus preventing continual growth of the nanoparticles than weakly binding molecules [70]. Examples of capping agents commonly used include oleic acid, oleylamine, trictylphosphine or oleyl alcohol.

2.2.2.3.3.2 The effect of the nature of the precursor

One of the most significant parameters to consider for colloidal synthesis is the choice of a suitable precursor as the synthesis process relies on the production of free monomers for nucleation and growth of the nanoparticles. The rate at which the monomer is thus made available and how rapidly the monomer reacts to begin the nucleation process affects the size and shape of the nanoparticles [73, 74]. The precursor must undergo a chemical process, usually decomposition to allow for the release of the free monomer into the reaction solution. The reactivity of the monomer is determined by how strongly the ligands bind to the monomer itself. The process of monomer formation due to precursor decomposition is given as:

$$P \overset{K_f}{\rightarrow} M \tag{2.7}$$

Where P is the precursor, K_f represents the formation rate/rate constant of the process and M is the free monomer formed after decomposition. Assuming a first-order reaction, the rate constant will be affected by temperature and activation energy, which can be represented as:

$$\frac{d[M]}{dt} = -\frac{d[P]}{dt} = Aexp\left\{\frac{-Ea}{RT_v}\right\}[P] \tag{2.8}$$

Where A represents the prefactor, T_v is the temperature of the reacting solution and E_a is the activation energy. Monomer formation thus depends on both the temperature of the reaction solution and the activation energy for precursor decomposition. A highly reactive precursor with a low activation energy will allow for rapid monomer production at low temperatures, resulting in rapid supersaturation and immediate nucleation. As a result of the fast nucleation and growth regime, more nuclei develop and continually merge with the free monomers quenching further nucleation. As a result, there is a low nanoparticle yield and a wide particle size distribution [73, 75]. A moderately reactive precursor, on the other hand, allows for a slow nucleation process followed by a stable growth regime, resulting in a good yield of nanoparticles with a narrower size distribution. Finally, when a slow-reacting precursor is utilized, monomer synthesis is delayed until a higher temperature is reached. As a result, monomer production is exceedingly slow, leading nuclei to form later than expected, resulting in nuclei of various sizes. Consequently, the growth regime progresses through the Ostwald ripening process, yielding larger nanoparticles [73].

2.2.2.3.3.3 The effect of reaction time

The quality and type of nanoparticles synthesized using the colloidal synthesis method are greatly influenced by length of time for which the reaction medium is incubated. Prolonging the reaction time improves the crystallinity of the nanoparticles which results in an increase in crystallite size. This is because longer reaction times yield larger particles due to the facilitation of the Ostwald ripening process [76, 77]. Umair and coworkers [78] studied the effect of nucleation time on the synthesis of zinc oxide (ZnO) nanoparticles and demonstrated that as the nucleation time increased, the average particle size also increased. They synthesized ZnO particle sizes of 41 ± 11nm, 84 ± 21 nm and 135 ± 95 nm for nucleation times of 0 min, 2 min and 8 min respectively.

2.2.2.3.3.4 The effect of reaction temperature

Temperature is one of the most important elements that influences the properties of the synthesized nanoparticles. The size of nanoparticles is mainly influenced by temperature because of competition between kinetic and thermodynamic processes during particle growth [79, 80]. **Fig. 2.14(a)** depicts a potential energy graph of the products formed from the thermodynamically controlled reaction (product C) and the kinetically controlled reaction (product D). Both reactions are dependent on the activation energy (E_a) with the kinetically controlled reaction having a lower E_a as compared to the thermodynamically controlled reaction. From the Arrhenius equation, equation 2.9, the rate constant of the reaction is exponentially dependent on the activation energy (E_a). As E_a increases, the rate constant k decreases and therefore the rate of the reaction decreases, resulting in a more stable product (C). But if we increase the temperature from T1 to T2 as shown in **Fig. 2.14(b)** this speeds up the rate of the reaction because the rate constant increases and product D is formed which is less stable.This results in bigger nucleation radius because of the Ostwald ripening process [81]. Sibokoza et al. [82] did a study on the effect of temperature on the synthesis of cobalt sulphide nanoparticles and they reported that as the reaction temperature was increased from 145 ℃ to 210 ℃, the nanoparticle size also increased from 3.40 ± 1.03 nm to 9.26 ± 2.08 nm respectively.

$$k = Ae^{-\frac{Ea}{RT}} \tag{2.9}$$

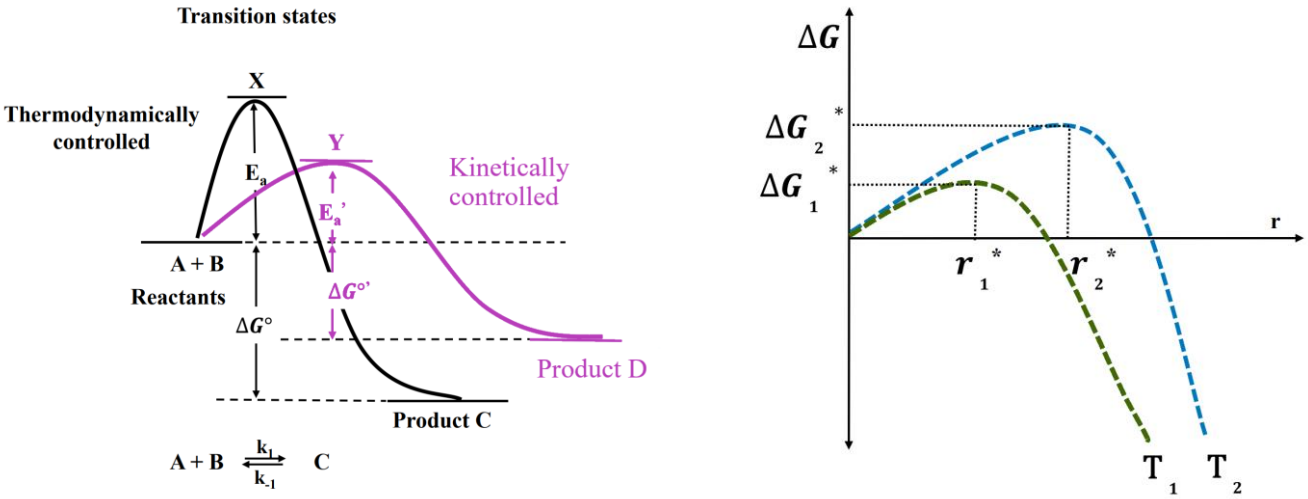

Fig. 2.14: (a) Potential energy graph of the thermodynamically and kinetically controlled reactions and (b) An illustration of the effect of temperature on the size of nanoparticles with an increase in temperature from T1 to T2 [81].

2.2.2.4 Single-source precursor (SSP) method

The synthesis of nanoparticles using single-source precursors was initially reported by Trindade and O'Brien in early 1996 [83, 84]. The single-source precursor method involves the decomposition of a molecular precursor, usually organometallic molecules in high boiling point coordinating solvents to form the desired products, **Scheme 1**. The selected precursor contains both the desired metal and corresponding chalcogen elements, which can therefore decompose under the right conditions to give metal chalcogenide compounds directly [85, 86]. The single-source precursor approach has several advantages over the dual precursor synthesis method. To begin with, the approach is impervious to air and moisture as the method avoids the introduction of precursors once the reaction has started because the precursor contains all the chemical elements required to produce the nanoparticles. Other advantages of the SSP method include safety and simplicity in carrying out the synthesis procedures, ease of separation of nanocrystalline material, better control over the size and shape of the nanoparticles, control over stoichiometry of the synthesized nanoparticles, reduction of impurities in the synthesized nanoparticles and since the molecules are usually organometallic in nature with some as coordination complexes, decomposition can occur at relatively low temperatures [2, 84, 87, 88]. The SSP method is an efficient synthesis method to producing monodispersed, high-quality crystalline semiconducting

nanomaterials. For metal sulfides specifically, there is a wide range of sulfur-containing ligands available, many of which are easily tunable, and changing the nature of these allows for controlled modification of the decomposition kinetics and secondary decomposition products [89]. Examples of commonly used sulphur ligands include thiolates, thioureas, xanthates and dithiocarbamates. Loh and coworkers in 2004 and 2006 [90, 91] were the first to successfully use molybdenum dithiocarbamate complexes as SSP in the synthesis of MoS_2. They found that the dithiocarbamate precursor decomposed cleanly in a wide range of substrates to yield edge-oriented, high crystalline quality MoS_2 two-dimensional nanosheets [90].

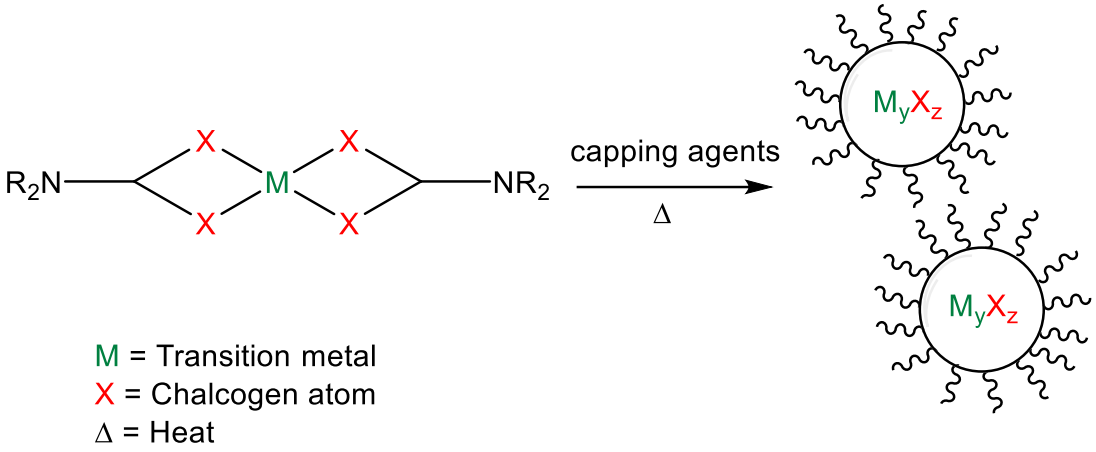

Scheme 2.1: Generic representation of decomposition of SSP to form the nanoparticles.

2.3 Applications of transition metal chalcogenides

Transition metal chalcogenides have sparked a lot of interest among researchers worldwide because of their features such as exceptional optical absorption, magnetism, electron mobility, and catalytic properties, transition metal chalcogenides have attracted a lot of attention around the world [9]. These interesting properties of the TMCs have made them find use in a variety of applications including photocatalysis, bio-sensing, and energy conversion and storage devices like dye-sensitized solar cells (DSSCs) just to mention a few.

2.3.1 Dye-sensitized solar cells

Dye Sensitized Solar Cells (DSSCs) today represent one of the most promising photovoltaic (PV) devices to affordably convert solar energy into electrical energy. The DSSC was first invented in

1991 by O'Regan and Grätzel as a cheaper alternative to traditional silicon photovoltaic cells [92, 93]. Their low solar-to-electrical energy conversion efficiency and photovoltaic performance stability have so far precluded them from successfully competing with existing commercial PV technologies for outdoor bulk electricity generation. Currently, research is ongoing to address the challenges of the DSSCs, which includes thoroughly examining the properties of the DSSC's components and making necessary changes. The DSSC set-up has three major components: the photoanode, the electrolyte and the counter electrode (CE). A schematic depicting the operating principle of DSSCs is shown in **Fig. 2.15**.

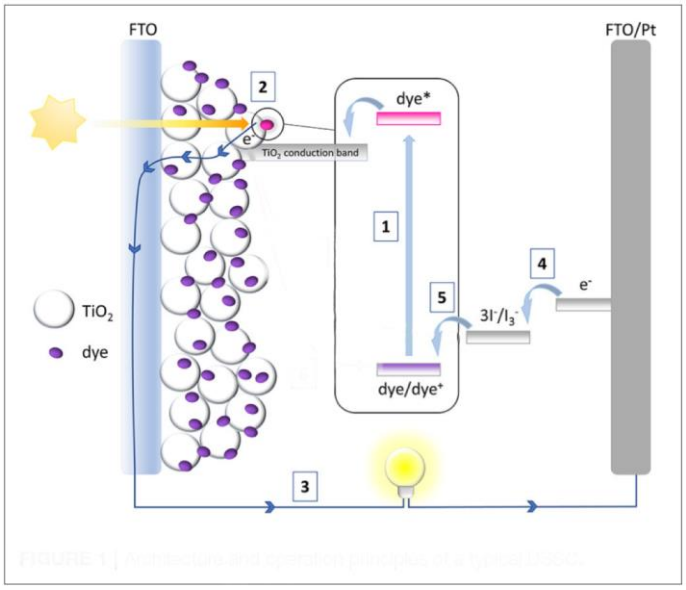

Fig. 2.15: Schematic illustration and operating principles of a DSSC [92].

2.3.1.1 Photoanode

In DSSCs, a typical photoanode is a dye-sensitized semiconductor nanocrystalline film (often TiO_2 or ZnO_2) deposited over a conductive substrate (e.g., FTO or ITO glass). It is responsible for photon harvesting, electron injection and collection, and recombination processes. An ideal photoanode consists of a mesoporous semiconductor with a high surface area, excellent electron transport mobility, and a conduction band with a lower energy than the dye's lowest unoccupied molecular orbital (LUMO) to allow for effective dye loading and electron collecting [94]. When choosing the dye, there are a few things to keep in mind. The dye must have a strong interaction with the oxide material, a high absorption efficiency in the visible region, and be easily reduced

by the electrolyte [95]. A variety of dyes have been studied, ranging from naturally occurring compounds derived from specific plant components to chemically manufactured organic dyes, some of which contain ruthenium metal in the complex [96–98].

2.3.1.2 Electrolyte

The electrolyte constitutes of a redox couple dispersed in an organic solvent and acts as a charge or ion transporter between the counter electrode and the photoanode. The redox couple should be chemically stable, have low viscosity to allow charge carriers to diffuse quickly, should not desorb the dye or disperse the FTO plates semiconductor material [99]. The most common, stable, and highly efficient redox couple used in DSSCs is the iodide/triiodide (I^-/I^-_3) redox couple.

2.3.1.3 Counter electrode

The counter electrode is the most crucial component in the effective operation of the DSSC. The counter electrode has three primary functions, (i) as a catalyst, the CE improves the collection of electrons from the external circuit at the electrolyte/CE interface region and transfer them into the inner cell electrolyte solution. The redox couple is reduced by the addition of electrons from the CE surface. For this process to work, a large surface area is required at the interface region to create more active sites for the reaction, **Fig. 2.16**. (ii) charge collector- the CE must be a good conductor to allow for the easy flow of electrons collected from the external circuit. (iii) as a light reflector, the CE enhances the utilization of sunlight by reflecting unabsorbed light into the cell [100]. To fulfill these basic functions, the counter electrode should have the following properties: high catalytic activity, high conductivity, large internal surface area, chemical corrosion resistance, high reflection, and good adhesiveness toward the FTO/ITO substrate [99, 100]. The role of the CE is to collect electrons from the external circuit and to reduce the triiodide to iodide ions in the electrolyte. The rate of the electrolyte reduction should ideally be comparable with the rate of dye regeneration by the electrolyte at the photoanode to maintain a low overvoltage and reduce energy loss expressed by the short-circuit photocurrent density, J_{sc}, Equation 2.12 [100]. When an ineffective CE is used, the performance of DSSCs significantly decreases which gives high resistance, (R_{ct}) via slow reaction. To date, platinum metal has been used as the counter electrode material because of its high catalytic activity, low R_{ct} and good conductivity. However, platinum is a noble metal thus expensive and scare, and it susceptible to corrosion by the commonly used

liquid iodide-triiodide (I^-/I^-_3) electrolyte which may result in the formation of PtI_4 [101]. These shortcomings of Pt have motivated research studies towards other CE materials with a high surface area, good electron conductivity and catalytic activities that are comparable to, if not better than Pt.

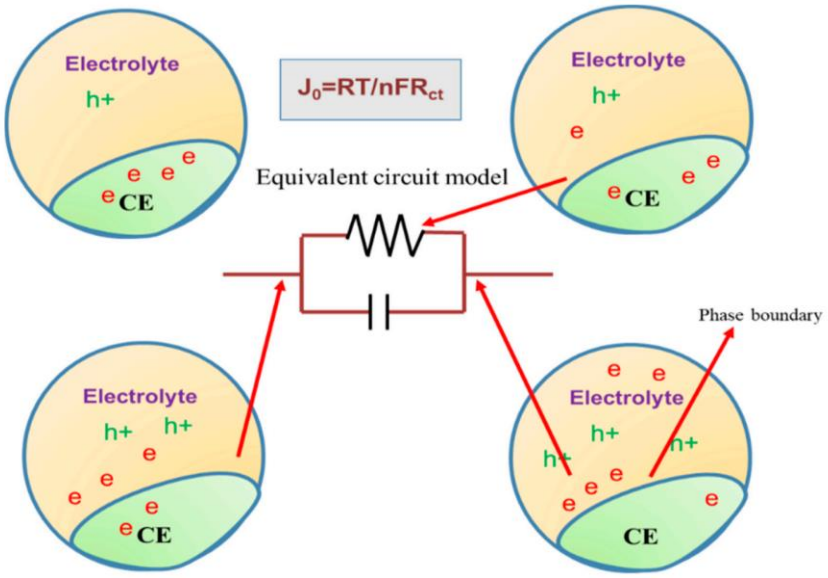

Fig. 2.16: Schematic diagram of the reaction site at the counter electrode (CE)/electrolyte interface region and the electron transfer mechanism from the CE to the electrolyte material [100].

The operation of a DSSC is based on a multistep process as outlined in **Fig. 2.15**. The first step (1) involves light passing through the transparent anode and the absorption of a photon by the sensitizer that determines the promotion of an electron in the excited state. An electron is then injected from the excited sensitizer into the conduction band of the semiconductor, the TiO_2 layer (2), thus leaving the sensitizer in the oxidized state. The injected electron percolates through the mesoporous structure of the semiconductor, driven by a chemical diffusion gradient and it is collected at the transparent conductive electrode and then transferred to the external circuit (3). Through the external circuit the electron reaches the counter-electrode and here interacts with the redox mediator turning it in its reduced form (4). The reduced state of the redox mediator finally reduces the oxidized sensitizer, regenerating the original dye and completing the circuit (5) [92].

2.3.1.3.1 Electrocatalytic performance of the counter electrode

Cyclic voltammetry (CV) is a useful electrochemical technique for determining the counter electrode's electrocatalytic activity in the (I^-/I^-_3) electrolyte. **Fig. 2.17** depicts a typical example of a cyclic voltammogram for the DSSC for various counter electrode materials. The electrocatalytic capability of the counter electrode from the CV provides two useful figures, the reduction current density and the peak-to-peak potential difference (Epp) [102, 103]. The reduction of the triiodide ions is crucial in the operation of the DSSC. The reduction reaction represented by equation 2.10, is characterized by the negative current cathodic peak ($I_p^{reduction}$) and the oxidation reaction, equation 2.11 is associated with the positive current anodic peak ($I_p^{oxidation}$) and the difference between the peak potentials is known as the peak-to-peak separation (Epp).

$$I_3^- + 2e^- \leftrightarrow 3I^- \tag{2.10}$$

$$3I_2 + 2e^- \leftrightarrow 2I_3^- \tag{2.11}$$

The cathodic peak current density ($I_p^{reduction}$) corresponds to the reaction rate of the catalyst for reducing I_3^- ions to I^- ions. In general, a higher cathodic peak current density implies that the catalytic material has better electrocatalytic ability. The Epp, on the other hand, gives information about the reversibility of the redox reaction, the smaller the Epp, the better the reversibility of the redox reaction [104].

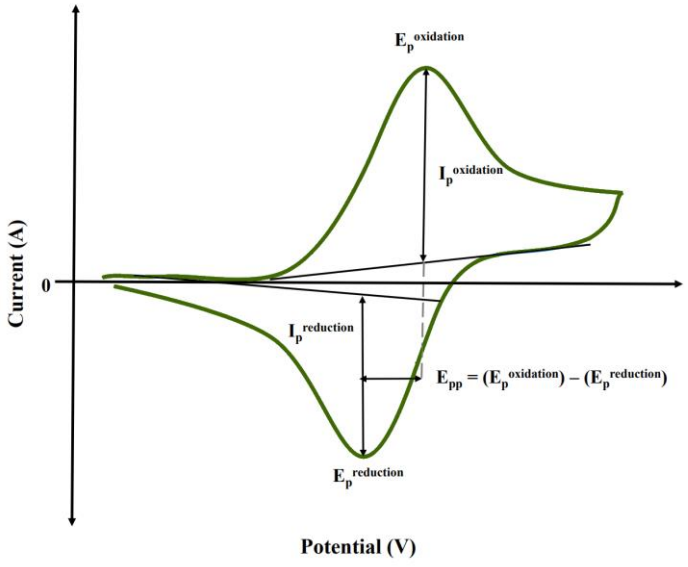

Fig. 2.17: An illustration of a typical cyclic voltammogram for the CE of the DSSC [102].

2.3.1.4 Evaluation of Dye-Sensitized Solar Cell Performance

An essential performance characterization technique for solar cells is the I-V curve measurement as shown in **Fig. 2.18**. The most common method for solar cells I-V measuring is to use a scan based on a stepwise change of bias power supply to the DUT (Device Under Test). The change of the voltage value sweep is fixed with a variable sampling time and during the sweep of the terminals of the DUT from open circuit to short circuit or vice versa, voltage and current should be measured in quasi static conditions [105, 106]. An I-V curve, as shown in **Fig. 2.18**, is a current versus voltage curve that can be used to determine the maximum power output of a cell. The overall performance of the DSSC can be evaluated based on sunlight-to-electric power conversion efficiency (η, %) as shown in equation 2.12, where J_{sc} is the short-circuit current density (mA cm $^{-2}$), V_{oc} is the open circuit voltage (V), FF the fill factor and P_{in} the power of the incident light. The photovoltage (V_{oc}) is the potential difference between the conduction band energy of semiconducting material (TiO_2 film) and the redox potential of the electrolyte under open circuit conditions or simply, the voltage across negative and positive electrodes at zero milliampere (mA) current [107, 108]. The photocurrent (J_{sc}) is determined based on the incident light harvest efficiency (LHE), charge injection and collection efficiencies. P_{max} is the maximum efficiency of the DSSC to convert sunlight into electricity. And FF is given as the ratio of maximum power output ($J_{mp} \times V_{mp}$) to the product of ($V_{oc} \times J_{sc}$) [107, 109].

$$FF = \frac{Area\ A}{Area\ B} = \frac{\mathrm{Jmp} \times \mathrm{Vmp}}{\mathrm{Voc} \times \mathrm{Jsc}} \tag{2.12}$$

And so, the overall efficiency (%) is the percentage of the solar energy (shining on a photovoltaic PV device) converting into electrical energy, where ɳ increases with the decrease in the value of J_{sc} and increase in the values of V_{oc}, FF, and molar coefficient of the dye, respectively [107].

$$\eta\ (\%) = \frac{Jsc\ \times \mathrm{Voc} \times \mathrm{FF}}{Pin} \tag{2.13}$$

External quantum efficiency (also known as IPCE) is the ratio of number of electrons flowing through the external circuit to the number of photons incident on the cells surface at any wavelength λ [91]. It is given as:

$$IPCE\%\ (\lambda)\ = 1240 \times \frac{Jsc}{Pin\lambda} \tag{2.14}$$

IPCE values are also related to LHE, φE1, and ηEC. As shown in Eq. 3:

$$IPCE\ (\lambda, nm) = LHE\varphi E1\eta EC \tag{2.15}$$

Where LHE is the light harvesting efficiency, φE1 is electron injection quantum efficiency, and ηEC is the efficiency of collecting electrons in the external circuit [107]. In general, the overall conversion efficiency of dye-sensitized solar cells is tested under standard irradiation conditions (100 mW/cm^2, AM 1.5) [109].

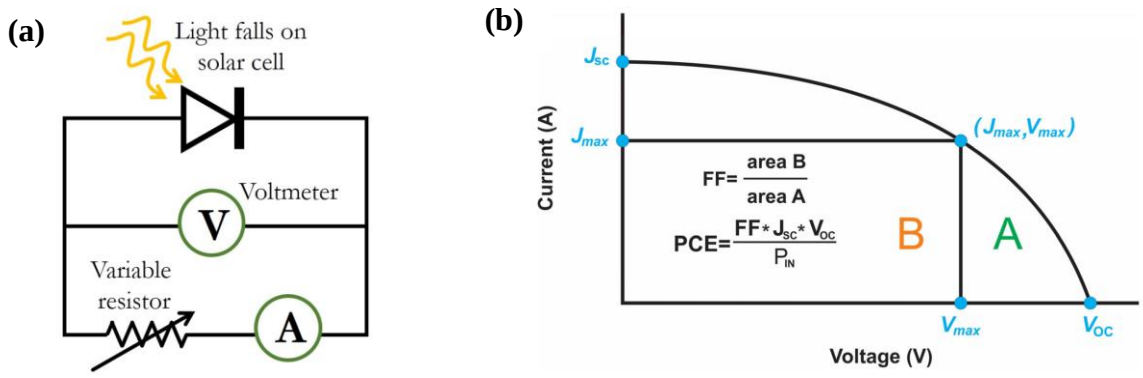

Fig. 2.18: (a) Set up for the measurement of an I-V curve (b) typical I-V curve for the DSSC [105, 107].

2.4 References

[1] P.D. Matthews, P.D. McNaughter, D.J. Lewis, P. O'Brien, *Chemical Science Journal*, 8 (2017) 4177–4187.

[2] M.R. Gao, Y.F. Xu, J. Jiang, S.H. Yu, Chemical Society Reviews, 42 (2013) 2986–3017.

[3] Y. Jing, B. Liu, X. Zhu, F. Ouyang, J. Sun, Y. Zhou, *Nano Letters*, 9 (2020) 1675–1694.

[4] T. Edvinsson, *Royal Society Open Science*, 5 (2018) 180387.

[5] G. Ramalingam, P. Kathirgamanathan, G. Ravi, T. Elangovan, B. Arjunkumar, N. Manivannan, K. Kasinathan, *Quantum dots-Fundamentals and Applications*, 9 (2020) 90140.

[6] J. Chang, E.R. Waclawik, *RSC Advances*, 4 (2014) 23505-23527.

[7] D.K. Seo, R. Hoffmann, *Theoretical Chemical Accounts*, 102 (1999) 23-32.

[8] J.A. Scher, J.M. Elward, A. Chakraborty, Journal of Physical Chemisty C, 120 (2016) 24999-25009.

[9] S. Yadav, S.R. Yashas, H.P. Shivaraju, *Environmental Chemistry Letters*, 19 (2021) 3683–

3700.

[10] T. Kippeny, L.A.Swafford, S.J. Rosenthal, *Journal of Chemistry Education*, 79 (2002) 1094-1100.

[11] D. Kuang, J. Brillet, P. Chen, M. Takata, S. Uchida, H. Miura, K. Sumioka, S.M. Zakeeruddin, M. Grätzel, *ACS Nano*, 2 (2008) 1113-1116.

[12] R.B. Schoolar, J.R. Dixon, *Physical Reviews*, 137 (1965) 667-670.

[13] W.W. Scanlon, *Journal of Physics and Chemistry of Solids*, 8 (1959) 423-428.

[14] E. Sathiyaraj, S. Thirumaran, *Chemical Physics Letters*, 739, (2020) 136972.

[15] C. Balischewski, H.S. Choi, K. Behrens, A. Beqiraj, T. Körzdörfer, A. Geßner, A. Wedel, A. Taubert, *ChemistryOpen*, 10, (2021) 272–295.

[16] S. Gross, A. Vittadini, N. Dengo, *Crystals*, 7 (2017) 7040110.

[17] A. Rodriguez, J. Dvorak, T. Jirsak, G. Liu, J. Hrbek, Y. Aray, C. Gonza, N. York, C. Quı, *American Chemical Society*, 125 (2003) 276–285.

[18] D.F. Cox, G.V. Gibbs, N.L. Ross, *Physics and Chemistry of Minerals*, 44 (2017) 561–566.

[19] J. Gopalakrishnan, T. Murugesan, M.S. Hegde, C.N.R. Rao, *Journal of Physical Chemistry Solid State Physics*, 12 (1979) 5255–5261.

[20] R.L. Kift, T.J. Prior, *Journal of Alloys and Compounds*, 505, (2010) 428–433.

[21] Openstax CNX 2020 https://phys.libretexts.org/@go/page/4543 accessed February 10, 2022.

[22] Vedantu 2019 https://www.vedantu.com/question-answer/the-compound-cucl-has-a-zinc-blende-structure-class-12-chemistry-cbse-5fd238687182ee79763e24f7 accessed February 10 2022.

[23] C.N.R. Rao, K.P.R. Pisharody, *Progress in Solid State Chemistry*, 10 (1976) 207–270.

[24] A.B. Kaul, *Journal of Materials Research*, 29 (2014) 348–361.

[25] M.J. Dunlop, R. Bissessur, *Journal of Materials Science*, 55 (2020) 6721–6753.

[26] U. Shamraiz, R.A. Hussain, A. Badshah, *Journal of Solid State Chemistry*, 238 (2016) 25–40.

[27] M. Achimovi, E. Dutková, E. Tóthová, Z. Buj, J. Brian, *Frontiers in Chemistry*, 13 (2019) 164–170.

[28] A. Singh, R. Manivannan, S.N. Victoria, *Arabian Journal of Chemistry*, 12 (2019) 2439–2447.

[29] D. Santamaría-Pérez, D. Daisenberger, J. Ruiz-Fuertes, T. Marqueño, R. Chulia-Jordan, C. Muehle, M. Jansen, P. Rodriguez-Hernandez, A. Muñoz, E.R. Johnson, A. Otero-De-La-Roza, *Chemical Science Journal*, 10 (2019) 6467–6475.

[30] K. Ishikawa, T. Isonaga, S. Wakita, Y. Suzuki, Y, *Solid State Ionics*, 79, (1995) 60–66.

[31] T. Morris, H. Copeland, G. Szulczewski, *Langmuir*, 18 (2002) 535–539.

[32] P. Jennings 2020 https://slideplayer.com/slide/12124442/ accessed February 13, 2022.

[33] H. Wen, Y.R. Liu, T. Huang, K.M. Xu, W.J. Zhang, W. Huang, L.S. Wang, *Journal of Chemical Physics*, 138 (2013) 174303.

[34] R.D. Averitt, D. Sarkar, N.J. Halas, *Physics Reviews Letters*, 78 (1997) 4217–4220.

[35] Y. Yu, T. Yang, T. Sun, *Nanomedicine*,15 (2020) 1127–1145.

[36] K. Habiba, VI. Makarov, B.R. Weiner, G. Morell, *Manufacturing Nanostructures*, 10 (2014) 263-292.

[37] N. Abid, A.M. Khan, S. Shujait, K. Chaudhary, M. Ikram, J. Haider, M. Khan, Q. Khan M. Maqbool, *Advances in Colloid Interface Science*, 300 (2022) 102597.

[38] I. Kammakakam, B. Nadeem, F. Wail, *Materials Advances*, 2 (2021) 1821–1871.

[39] Z. Li, R.J. Young, C. Backes, W. Zhao, X. Zhang, A.A. Zhukov, E. Tillotson, A.P. Conlan, F. Ding, S.J. Haigh, K.S. Novoselov, J.N. Coleman, *ACS Nanoscience*, 14 (2020) 10976–10985.

[40] T.K. Mukhopadhyay, A. Datta, *Physical Chemistry Chemical Physics*, 22 (2020) 22157–22179.

[41] A. Amiri, M. Naraghi, G. Ahmadi, M. Soleymaniha, M. Shanbedi, *FlatChem*, 61 (2018) 101016.

[42] X. Gu, Y. Zhao, K. Sun, C.L.Z. Vieira, Z. Jia, C. Cui, Z. Wang, A. Walsh, S. Huang, *Ultrasonics. - Sonochemistry*, 58 (2019) 104630.

[43] K.D. Sumanth, J.B. Kumar, H.M. Mahesh, *Elsevier* (2018) 59-88.

[44] M. Braun, *Handbook of Manufacturing Engineering Technologies*, 1 (2015) 2929–2957.

[45] P. Asanithi, S. Chaiyakun, P. Limsuwan, *Journal of Nanomaterials*, 2012 (2012) 963609.

[46] D. Muller 2020 https://www.vacuumscienceworld.com/blog/vacuum-coating-sputter-technology accessed February 12 2022.

[47] Y. Wang, Y. Xia, *NanoLetters*, 4 (2004) 2047–2050.

[48] R.J. Martín-Palma, A. Lakhtakia, *Elsevier*, 15 (2013) 383–398.

[49] Y.H. Lee, X.Q. Zhang, W. Zhang, M.T. Chang, C. Lin, K. Di. Chang, Y.C.Yu, J.T.W. Wang, C.S. Chang, L.J. Li, T.W. Lin, *Advance Materials*, 24 (2012) 2320–2325.

[50] L. Sun, B.H. Hong, *Nature Reviews*, 34 (2021) 0123456789.

[51] D. Bokov, A. Turki Jalil, S. Chupradit, W. Suksatan, M. Javed Ansari, I.H. Shewael, G.H. Valiev, E. Kianfar, *Advances in Materials Science and Engineering*, 2021 (2021) 5102014.

[52] R. Yarbrough, K. Davis, S. Dawood, H. Rathnayake, *RSC Advances*, 10 (2020) 14134–14146.

[53] U.G. Akpan, B.H. Hameed, *Applied Catalysis A: General*, 375 (2010) 1–11.

[54] G.V. Aguilar 2019 https://www.intechopen.com/chapters/64744 accessed February 14, 2022.

[55] X. Zhao, Q. Yang, Z. Quan, *Chemical Communications journal*, 55 (2019) 8683–8694.

[56] J. Polte, *Crystal Engineering Communication*, 17 (2015) 6809–6830.

[57] N. Chestnoy, T.D. Harris, R. Hull, L.E. Brus, *Journal of Physical Chemistry*, 90 (1986) 3393–3399.

[58] C.B. Murray, D.J. Norris, M.G. Bawendi, *Journal of American Chemical Society*, 115 (1993) 8706–8715.

[59] V. LaMer, R. Dinegar, *Journal of American Chemical Society*, 72 (1950) 4847–4854.

[60] N.T.K. Thanh, N. Maclean, S. Mahiddine, *Chemistry Reviews*, 114 (2014) 7610–7630.

[61] J. Lee, J. Yang, S.G. Kwon, T. Hyeon, *Nature Reviews*, 1, (2016) 101038.

[62] X.Y. Liu, *Journal of Chemical Physics*, 112 (2000) 9949–9955.

[63] C.B. Whitehead, S. Özkar, R.G. Finke, *Materials Advances* 2, (2021) 186–235.

[64] V.K. LaMer, *Industrial and Engineering Chemistry Research*, 44 (1952) 1270–1277.

[65] A. Naik, P. Sabyasachi, S. Debasis, G. Asok, *Physical Chemistry Chemical Physics*, 3 (2019) 101039.

[66] C.C. Yec, H.C. Zeng, *Journal of Materials Chemistry A*, 2 (2014) 4843–4851.

[67] C.J. Gommes, *Nanoscale*, 11 (2019) 7386–7393.

[68] G. Madras, B.J. McCoy, *Journal of Chemical Physics*, 119 (2003) 1683–1693.

[69] J.K. Patra, K.H. Baek, *Journal of Nanomaterials*, 2014, (2014) 417305.

[70] R.A. Sperling, W.J. Parak, *Philosophical Transactions of the Royal Society A: Mathematical Physical Engineering Science*, 368 (2010) 1333–1383.

[71] S. Gulati, M. Sachdeva, K.K. Bhasin, *AIP Conference Proceddings*, 1953, (2018).

[72] S. Campisi, M. Schiavoni, C.E. Chan-Thaw, A. Villa, *Catalysts*, 6 (2016) 1–21.

[73] J. Van Embden, A.S.R. Chesman, J.J. Jasieniak, *Chemistry of Materials*, 27 (2015) 2246–2285.

[74] H. Chang, B.H. Kim, S.G. Lim, H. Baek, J. Park, T. Hyeon, *Inorganic Chemistry*, 60 (2021) 4261–4268.

[75] K.L. Sowers, B. Swartz, T.D. Krauss, *Chemistry of Materials*, 25 (2013) 1351–1362.

[76] Y. Mastai, R. Polsky, Y. Koltypin, A. Gedanken, G. Hodes, *Journal of American Chemical Society*, 121 (1999) 10047-10052.

[77] N. Moloto, M.J. Moloto, N.J. Coville, S. Sinha Ray, *Journal of Crystal Growth*, 324 (2011) 41-52.

[78] U. Manzoor, F. Tuz Zahra, S. Rafique, M.T. Moin, M. Mujahid, *Journal of Nanomaterials*, 2015 (2015) 189058.

[79] N. Moloto, N. Revaprasadu, P.L. Musetha, M.J. Moloto, *Journal of Nanoscience and Nanotechnology*, 9 (2009) 4760-4766.

[80] D.P. Bisen, R. Sharma, N. Brahme, R. Tamrakar, *Chalcogenide Letters*, 6 (2009) 427-431.

[81] C.J. Dalmaschio, C. Riberio, E.R. Leite, *Nanoscale*, 2 (2010) 2336-2345.

[82] S.B. Sibokoza, N. Moloto, M.J. Moloto, P.N. Sibiya, *Chalcogenide Letters*, 14 (2017) 69-78.

[83] M.A. Malik, N. Revaprasadu, P. O'Brien, *Chemistry of Materials*, 13 (2001) 913–920.

[84] N. Boadi, A. Malik, P. O'Brien, J. Awudza, *Journal of Chemical Society Dalton Transactions*, 41 (2012) 10497–10506.

[85] N. Moloto, M.J. Moloto, N.J. Coville, S. Sinha Ray, *Journal of Crystal Growth*, 311 (2009) 3924–3932.

[86] N. Maiti, S.H. Im, Y.H. Lee, C.H. Kim, S. Seok, *Crystal Engineering Communication*, 13 (2011) 3767–3772.

[87] P. Marchand, S. Sathasivam, B.A.D. Williamson, D. Pugh, S.M. Bawaked, S.N. Basahel, A.Y. Obaid, D.O. Scanlon, I.P. Parkin, C.J. Carmalt, *Journal of Materials Chemistry C*, 4 (2016) 6761–6768.

[88] A.K. Sahoo, S.K. Srivastava, *Journal of Nanoparticle Research*, 15, (2013) 151591.

[89] J.C. Sarker, G. Hogarth, *Chemistry Reviews*, 121 (2021) 6057–6123.

[90] H. Zhang, K.P. Loh, C.H. Sow, H. Gu, X. Su, C. Huang, Z.K. Chen, *Langmuir*, 20 (2004)

6914–6920.

[91] K.P. Loh, H. Zhang, W.Z. Chen, W. Ji, *Journal of Physical Chemistry B*, 110 (2006)1235–1239.

[92] M. Yilmaz, S.H. Hsu, S. Raina, S., Howell, M., Kang, W.P., Huang, *Journal of Renewable and Sustainable Energy*, 10 (2018) 063501.

[93] M. Kokkonen, P. Talebi, J. Zhou, S. Asgari, S.A. Soomro, F. Elsehrawy, J. Halme, S. Ahmad, A. Hagfeldt, S.G. Hashmi, *Journal of Materials Chemistry A*, 9 (2021) 10527–10545.

[94] M. Ye, X. Wen, M. Wang, J. Iocozzia, N. Zhang, C. Lin, Z. Lin, *Materials Today*, 18 (2015) 155–162.

[95] S. Shalini, R. Balasundaraprabhu, T.S. Kumar, N. Prabavathy, S. Senthilarasu, S. Prasanna, *International Journal of energy Research*, 40 (2016) 1303–1320.

[96] N.A. Ludin, A.M. Al-Alwani Mahmoud, A. Bakar Mohamad, A.A.H. Kadhum, K. Sopian, N.S. Abdul Karim, *Renewable and Sustainable Energy Reviews*, 31 (2014) 386–396.

[97] A. Mahmood, *Solar Energy*, 123, (2016) 127–144.

[98] F. Gao, Y. Wang, D. Shi, J. Zhang, M. Wang, X. Jing, R. Humphry-Baker, P. Wang, S.M. Zakeeruddin, M. Grätzel, *Journal of American Chemical Society*, 130 (2008) 10720–10728.

[99] S.N. Karthick, K.V. Hemalatha, S.K. Balasingam, F. Manik Clinton, S. Akshaya, H.J. Kim, *Interfacial Engineering in Functional Materials for Dye-sensitized Solar Cells*, 1 (2019) 1–16.

[100] M.R. Samantaray, A.K. Mondal, G. Murugadoss, S. Pitchaimuthu, S. Das, R. Bahru, M.A. Mohamed, *Materials*, 13 (2020) 2779.

[101] E. Olsen, G. Hagen, S. Eric Lindquist, *Solar Energy Materials and Solar Cells*, 63 (2000) 267–273.

[102] E. Meyer, A. Bede, N. Zingwe, R. Taziwa, *Materials (Basel)*, 12, (2019) 1980.

[103] P.W. Chen, C.P. Lee, L.Y. Chang, J. Chang, M.H. Yeh, L.Y. Lin, R. Vittal, J.J. Lin, K.C. Ho, *RSC Advances*, 3 (2013) 5871–5881.

[104] X. Qian, H. Li, L. Shao, X. Jiang, L. Hou, *ACS Applied Materials and Interfaces*, 8 (2016) 29486–29495.

[105] A.E. Touihri, A. Torchani, R. Gharbi, *Institute of Electrical and Electronics Engineers*, 2 (2015) 4799730.

[106] N. Koide, L. Han, *Review of Scientific Instruments*, 75 (2004) 2828–2831.

[107] K. Sharma, V. Sharma, S.S. Sharma, *Nanoscale Research Letters*, 13, (2018) 13381.

[108] Z. Jin, M. Zhang, M. Wang, C. Feng, Z. Wang, *Accounts of Chemical Research*, 50 (2017) 895–904.

[109] J. Gong, K. Sumathy, Q. Qiao, Z. Zhou, *Renewable and Sustainable Energy Reviews*, 68 (2017) 234–246.

CHAPTER 3

Synthesis and characterization of gold dithiocarbamate complexes single-source precursors

3.1 Introduction

The chemistry of dithiocarbamate (DTCs) ligands could be dated to have started in the early twentieth century, around the 1930s. Dithiocarbamates are a well-studied class of ligands with applications in a wide range of fields including vulcanization accelerators, agriculture (pesticide and fungicides) and high-pressure lubricants [1, 2]. Recently its use in the preparation of dithiocarbamate metal complexes and then semiconducting nanoparticles has drawn more attention in the field of material sciences, technology, and engineering [3]. Dithiocarbamates (DTCs) are organosulfur ligands, with the general formula $N{-}CS_2$, which form stable complexes with all transition metals stabilizing both high and low oxidation states [1]. The ability of the ligands to stabilize a variety of metal oxidation states is due to the two resonance forms of dithiocarbamate functional group, **Fig. 3.1**. In the 'dithiocarbamate' resonance form there is a single bond between the nitrogen atom and the carbon atom bearing the sulfur, and there is delocalization of the -1 charge between the carbon and two sulfur atoms. With the 'thioureide', resonance form, the lone pair on the nitrogen atom is delocalized, resulting in a double bond character between the nitrogen and the carbon atom bearing the sulphur, while the two sulfur atoms both possess negative charges. The former form is described as a strong-field ligand that stabilizes low-valent metal centers and the latter form which is a weak-field ligand that stabilizes high-valent metal centers [1, 2, 4].

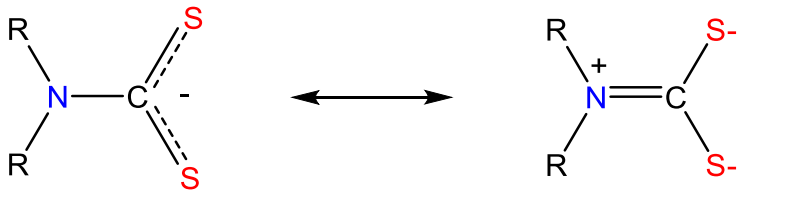

Dithiocarbamate Thioureide

Fig. 3.1: Resonance forms of the dithiocarbamates.

DTCs can bind to metals in a variety of ways, but the bidentate chelate is by far the most prevalent. Chelation improves the complex's thermodynamic stability and increases the coordination number as compared to simple monodentate ligands. The chelating abilities are due to their possession of two donor sulfur atoms in the ligands, **Fig. 3.1** [1, 4]. A large variety of DTCs ligands with different substituents are commercially available and can be subdivided into three groups: (i) symmetrically disubstituted, (ii) unsymmetrically disubstituted, and (iii) monosubstituted. Symmetrically substituted DTCs are dominated by dialkyl-substituents, unsymmetrically disubstituted DTCs have different alkyl substituents, or they may have one alkyl and one aryl substituent and monosubstituted DTCs have either an alkyl or an aryl substituent, **Fig. 3.2** [4].

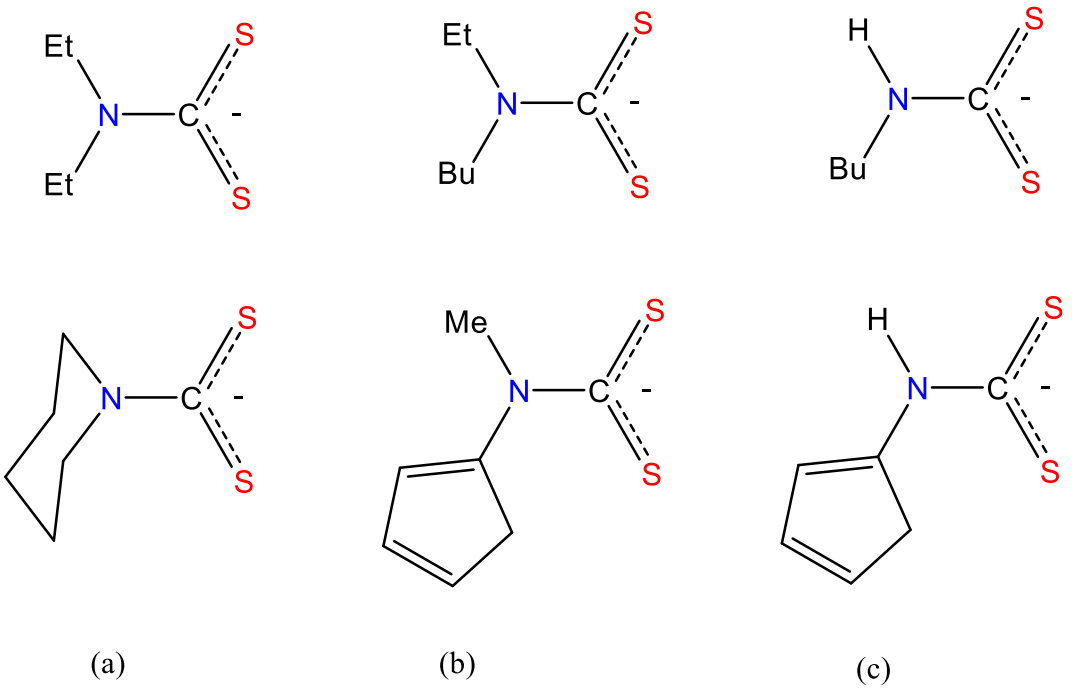

Fig. 3.2: Examples of some different types of DTCs (a) symmetrically disubstituted, (b) unsymmetrically disubstituted, and (c) monosubstituted.

Metal dithiocarbamate complexes can be synthesized using different methods such as direct addition and one pot synthesis. The most typical procedure is to add the dithiocarbamate ligand directly to the metal salt, and a typical example is shown in **Scheme 3.1**.

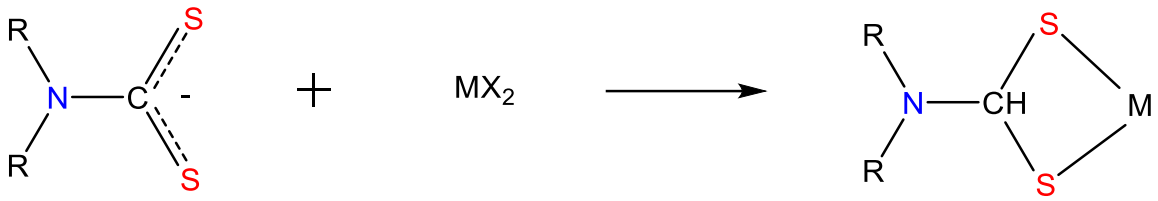

Scheme 3.1: Synthesis of metal dithiocarbamate complexes by direct ligand addition.

In a one pot synthesis procedure, the amine and carbon disulfide in suitable solvents are allowed to react for a short time before adding the aqueous solution of metal salt [5] **Scheme 3.2**.

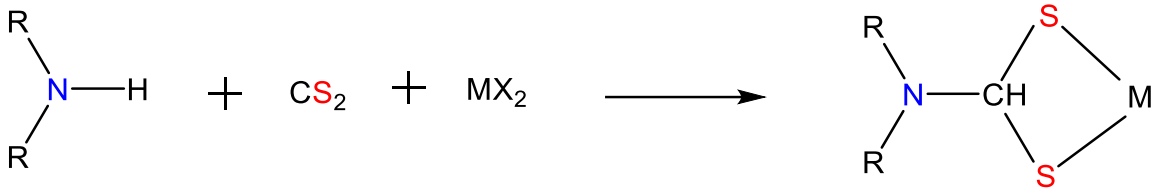

Scheme 3.2: Synthesis of metal dithiocarbamate complexes by one-pot synthesis.

Most transition metal dithiocarbamate complexes are synthesized by adding a water-soluble metal salt to an aqueous solution of DTC salt and have been frequently used as single-source precursors (SSPs) for metal sulphide nanoparticles by several groups. O'Brien and co-workers carried out pioneering work in the synthesis of semiconducting cadmium sulphide and zinc sulphide nanoparticles from the solvothermal decomposition of metal dithiocarbamate precursors [6, 7]. Herein, we report the synthesis and characterization of gold dithiocarbamate complexes from three different symmetrically disubstituted DTCs ligands and perform studies on their effectiveness as SSPs for the synthesis of gold (I) sulphide nanostructures.

3.2 Experimental section

3.2.1 Materials

Gold (III) chloride hydrate (99%), sodium diethyldithiocarbamate trihydrate (DTC), sodium pyrrolidine dithiocarbamate ($PDTC^1$), ammonium pyrrolidine dithiocarbamate ($PDTC^2$), dichloromethane (anhydrous, 99.8%), and dimethyl sulfoxide-d6 (99.9 atom % D) were purchased from Sigma Aldrich and were used without any purifications and the absolute ethanol (99%) was purchased from ACE chemicals.

3.2.2 Synthesis of gold dithiocarbamate complexes

3.2.2.1 Synthesis of gold diethyldithiocarbamate {Au(DTC)} complex

In a two-necked round bottom flask, gold (III) chloride hydrate (0.02 g, 0.05 mmol) was dissolved in dichloromethane (10 mL). Sodium diethyldithiocarbamate trihydrate (0.01 g, 0.05 mmol) was dissolved in ethanol (15 mL) and slowly added to the reaction mixture. The reaction mixture was stirred at room temperature and maintained under nitrogen gas flow for 3 h. The solvent was removed using a rotary evaporator and the product was dried in vacuo yielding a yellow solid and stored in a desiccator for further characterization. To obtain crystals, after the 3 h reaction time elapsed, the precipitate was filtered off, and the solution was left for crystallization. After 3 - 4 days, needle-like orange crystals formed in the mother-liquor and were characterized.

Yield 86%; M.pt 218-222 ℃. FT-IR (cm^{-1}): υ (N-H) 3495-3264, υ (C-N) 1549, υ (C-S) 1086. ^{1}H NMR (500 MHz, d-DMSO) δ (in ppm), 1.04-1.07 (t, 12H, $C\underline{H}_3$), 3.75-3.81(qd, 8H, $C\underline{H}_2CH_3$). ^{13}C NMR δ (in ppm), 12.56 ($\underline{C}H_3$), 46.92 ($\underline{C}H_2CH_3$), 194.20 ($N\underline{C}SS$). Anal cal for $C_{10}H_{20}AuN_2S_4$ (493.491) C, 24.34; H, 4.09; N, 5.68; S, 25.96. Found: C, 23.79; H, 5.46; N, 2.74; S, 25.23. ESI-MS m/z $[M+H]^+$ = 493.0248.

3.2.2.2 Synthesis of gold pyrrolidinedithiocarbamate {Au(PDTC[1])} complex from the sodium salt

To an *in situ* formed solution of the gold precursor, a solution of sodium pyrrolidine dithiocarbamate (0.008 g, 0.05 mmol) in ethanol (15 mL) was added dropwise and the mixture was stirred for 3h. A rotary evaporator was used to extract the solvent, and the result was then dried in vacuo, yielding a yellow solid that was stored in a desiccator for further analysis. To obtain crystals, after the 3 hours of reaction time had passed, the precipitate was filtered out and the solution was left undisturbed for crystallization. After 3 - 4 days, needle-like orange crystals formed in the mother liquor, which were then characterized.

Yield 78%; M.pt 195-198 ℃. FT-IR (cm^{-1}): υ (N-H) 3338-3185, υ (C-N) 1555, υ (C-S) 1018. ^{1}H NMR (500 MHz, d-DMSO) δ (in ppm), 2.12-2.15 (d, 4H, $C\underline{H}_2$), 3.88-3.92(d, 4H, $NC\underline{H}_2$). ^{13}C NMR δ (in ppm), 23.97 ($\underline{C}H_2$), 51.63 ($\underline{C}H_2CH_2$), 189.21 ($N\underline{C}SS$). Anal cal for $C_{10}H_{18}AuN_2S_4$ (491.47) C, 24.44; H, 3.66; N, 5.70; S, 26.03. Found: C, 24.47; H, 3.87; N, 4.76; S, 23.68. ESI-MS m/z $[M+H]^+$ = 491.0046.

3.2.2.3 Synthesis of gold pyrrolidinedithiocarbamate {Au(PDTC^2)} complex from the ammonium salt

To an *in situ* formed solution of the gold precursor, a solution of ammonium pyrrolidine dithiocarbamate (0.008 g, 0.05 mmol) in ethanol (15 mL) was added dropwise and the mixture was stirred for 3h. A rotary evaporator was used to extract the solvent, and the result was then dried in vacuo, yielding a yellow solid that was stored in a desiccator for further analysis. To obtain crystals, after the 3 hours of reaction time had passed, the precipitate was filtered out and the solution was left undisturbed for crystallization. After 3 - 4 days, needle-like orange crystals formed in the mother-liquor which were then characterized.

Yield 70%; M.pt 189-192 ℃. FT-IR (cm^{-1}): υ (C-N) 1563, υ (C-S) 1146. ^{1}H NMR (500 MHz, d-DMSO) δ (in ppm), 1.97-2.02 (d, 4H, C$\underline{H}_2$), 3.73-3.79 (d, 4H, NC$\underline{H}_2$). ^{13}C NMR δ (in ppm), 23.63 ($\underline{C}H_2$), 51.59 ($\underline{C}H_2CH_2$), 185.27 (N$\underline{C}$SS). Anal cal for $C_{10}H_{18}AuN_2S_4$ (491.47) C, 24.44; H, 3.66; N, 5.70; S, 26.03. Found: C, 25.19; H, 3.83; N, 4.89; S, 24.49. ESI-MS m/z $[M+H]^+$ = 491.0034.

3.3 Characterization techniques

The synthesized gold dithiocarbamate complexes were characterized using the following techniques: Fourier transform infrared spectroscopy (FTIR), nuclear magnetic resonance spectroscopy (NMR), Single crystal X-ray crystallography, high-resolution mass spectrometry (HRMS), elemental analysis (EA), ultraviolet visible spectroscopy (UV-Vis) and thermogravimetric analysis (TGA). The FT-IR spectra were recorded on a Bruker Tensor 27 spectrometer equipped with a diamond attenuated total reflectance crystal. The NMR spectra were recorded on a 500 MHz Bruker AVANCE III spectrometer for both ^{1}H and ^{13}C nuclei using d-DMSO. A suitable crystal was selected from the mother liquor and analysed on a Bruker APEX-II CCD diffractometer. The crystals were kept at 173.15 K during data collection. Using Olex2, the structures were solved with the ShelXT structure solution program using Intrinsic Phasing and refined with the ShelXL refinement package using Least Squares minimisation. High resolution mass spectra were recorded on a Bruker Compact Q-TOF mass spectrometer (Bruker Daltonics, Bremen, Germany) with ESI in positive ionization mode using acetonitrile as matrix and a detection range of 50-1300 m/z. The absorption measurements were carried out using a Specord 210 Analytik Jena UV-vis spectrophotometer after dispersing the complexes in DMSO. The

elemental compositions (C, H, N and S) were measured using a Vario Elementar III microcube CHN. Thermogravimetric analysis (TGA) was performed with a Perkin Elmer 4000 thermogravimetric analyser under a nitrogen gas flow and heating rate of 5 ℃/min.

3.4 Results and discussion

3.4.1 Purity of the complexes

Melting point and elemental analysis was done to check the purity of the synthesized gold dithiocarbamate complexes and the results are summarized in **Table 3.1**. The melting point of a solid compound is the temperature at which it changes into a liquid and any compound can be considered as pure if it has a melting point range of less than 3 ºC [8]. From the results, all the three complexes have a temperature range equal to or above 3 ºC, indicating the presence of impurities. Despite the complexes being made from similar sources, there is a wide range in the melting points determined due to the presence of impurities. Elemental analysis was done to determine the weight percentage of carbon (C), hydrogen (H), nitrogen (N) and sulphur (S) in the complexes and to also check the purity of the complexes. The accepted deviation of elemental analysis results from the calculated is 0.5% [8]. From the results summarized in **Table 3.1**, all the values obtained show a large difference (> 0.5%) between the actual and theoretical values. The differences can be attributed to the presence of impurities as also determined from the melting point. From the HRMS spectra shown in **Fig. S1 - S3** of the complexes, the most intense ion peaks were assigned as the base peaks and the results are summarized in **Table 3.1.** The base peaks, correlates with the $Au(C_5H_{10}NS_2)_2$ fragment in the Au(DTC) complex which, correspond to gold bonded to two diethyldithiocarbamate ligands and for the Au(PDTC^1) and Au(PDTC^2) complexes, they correspond to gold bonded to two pyrrolidinedithiocarbamate ligands. For the Au(DTC) complex, the parent peak is different from the base peak. The possible presence of impurities, while not desired, have little effect on the synthesis of nanoparticles as the important thing is the Au-S bond and the rest undergoes decomposed.

Table 3.1: Analytical data for the synthesized complexes

					Elemental Analysis (%): Found (Cal.)			
Complex	**Color**	**Melting point (℃)**	**HRMS (m/z)**	**Yield (%)**	**C**	**H**	**N**	**S**
Au(DTC)	yellow	218-222	493.0248 494.0255 496.0215	86	23.79 (24.34)	5.46 (4.09)	2.74 (5.68)	25.23 (25.96)
Au(PDTC[1])	yellow	195-198	491.0046 488.9906 489.9224 492.0068	78	24.47 (24.44)	3.87 (3.66)	4.76 (5.70)	23.68 (26.03)
Au(PDTC[2])	yellow	189-192	491.0034 488.9907 489.9922 492.0050	70	25.19 (24.44)	3.83 (3.66)	4.89 (5.70)	24.49 (26.03)

3.4.2 Infrared spectral studies of the complexes

The important absorptions obtained from FT-IR spectroscopy for the DTC ligands and complexes are due to the υC=NS_2 (thioureide band), υC−S and υN−H and υO−H stretching modes. The stretching vibration of the thioureide band, is observed around 1450–1580 cm^{-1}, the stretching vibration for the υC−S is around 950–1050 cm^{-1} and the stretching vibration mode for the υN−H and υO−H is observed around 3100–3400 cm^{-1} for the DTC ligands [1, 9, 10]. The stretching vibrational modes of the ligands and their respective complexes are presented in **Table 2**. **Fig. 3.2 (a, b, and c)** exhibit overlaid FT-IR spectra of the dithiocarbamate ligands and complexes, respectively. In all three complexes, it can be observed that there is an increase in the wavenumbers of the complexes as compared to the ligands, which is a clear indication of complex formation. The υC−N (thioureide band) values shifting to higher wave numbers are attributed to the shift in electron density towards the gold atom through the thioureide bond from the dithiocarbamate. The

thioureide band usually occurs as a single high intensity peak with bond order between a (C−N) single bond around 1250−1350 cm^{-1} and a (C=N) double bond around 1640−1690 cm^{-1} [9]. All the three complexes have the thioureide band around 1546−1561 cm^{-1}, suggesting a double bond character (C=N). For the υC−S band, the number of signals and 'multiplicity' is related to the nature of coordination of the DTC ligand to the metal center atom as either bidentate or monodentate. A single band usually indicates bidentate coordination, whereas splitting of the band by ± 20 cm^{-1}, indicates monodentate coordination [11, 12]. The υC−S band, which was around 923–971 cm^{-1} without any splitting in all the complexes, suggested symmetrically bidentate coordination of the $-CS_2$ moiety to the metal center. The metal ligand bond (υM−S) is not observed as it is present in the far IR region of the electromagnetic spectrum, i.e., in the fingerprint region. The obtained IR results are like those obtained from the work done by Sulaiman et al on similar gold dithiocarbamate complexes. They reported the υC−N stretch around 1480−1483 cm^{-1}, and the υC−S stretch around 993−1067 cm^{-1} [13].

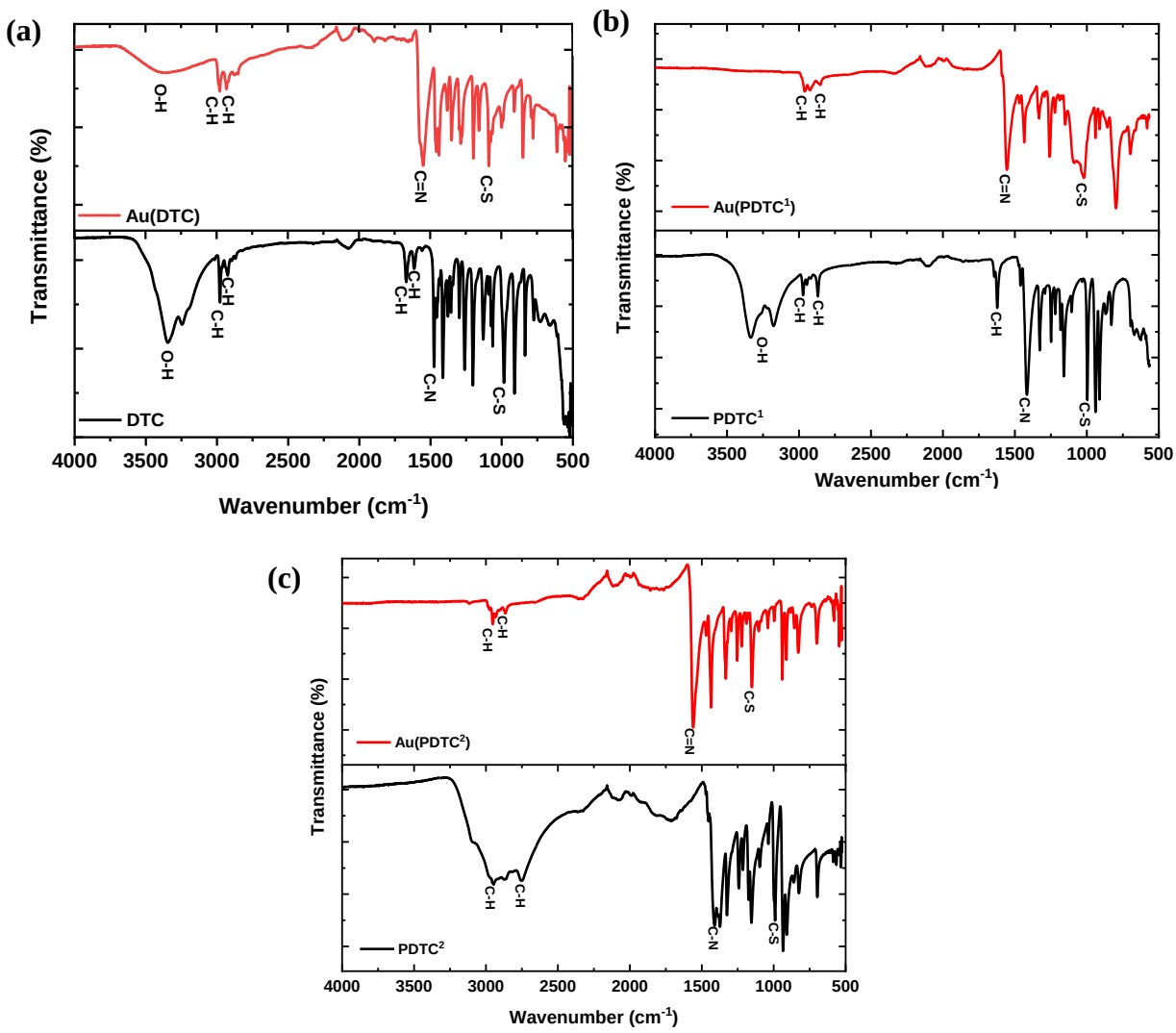

Fig. 3.3: FT-IR spectra of the dithiocarbamate ligands with their respective gold complexes, (a) Au(DTC) complex, (b) Au(PDTC^1) and (c) Au(PDTC^2) complexes.

Table 3.2: FT-IR assignments for the synthesized gold dithiocarbamate complexes

Assignment	Na(DTC) (cm^{-1})	Au(DTC) (cm^{-1})	Na(PDTC^1) (cm^{-1})	Au(PDTC^1) (cm^{-1})	Na(PDTC^2) (cm^{-1})	Au(PDTC^2) (cm^{-1})
C-N	1472	-	1414	-	1407	-
C=N	-	1549	-	1555	-	1563

C-S	982	1086	992	1018	990	1146
C-H	2983	2976	2971	2976	2945	2974
	2928	2932	2867	2932	2748	2861
N-H	3346	3495	3338	-	-	-
	3250	3264	3185	-	-	-

3.4.3 NMR Spectral studies

DTC ligands and complexes show characteristic NMR spectral features that can be used to confirm complexation and two nuclei can be used, the ^{1}H and ^{13}C. The ^{13}C nuclei is the most important as it gives more information about the ligands and the complexes. The ^{13}C chemical shifts of the $N^{13}CS_2$ group of the DTCs (ligands and complexes) are detected in the range of 185-220 ppm. Upon complexation, the chemical shift of the carbon atom in the $-NCS_2$ moiety of the dithiocarbamate ligand varies with the coordinated atom (normal or high oxidation state transition metals) [14]. For normal oxidation state transition metal complexes, the $\delta(N^{13}CS_2)$ is observed in the range 202-213 ppm and for high oxidation state transition metal complexes this is observed between 190-200 ppm [14]. From these observations, a correlation between ^{13}C chemical shifts of the $-NCS_2$ moiety and the $\upsilon C{-}N$ stretching vibration in the infrared spectra has been established. Low $\delta(N^{13}CS_2)$ values correlate to high $\upsilon C{-}N$ values, and high $\delta(N^{13}CS_2)$ values correlate to low $\upsilon C{-}N$ values [14].

The ^{13}C NMR spectra of the free ligands and the complexes are shown in **Fig. 3.7, 3.8 and 3.9**. In all spectra of the complexes, there are three signals of the carbon atoms of the alkyl chain and pyrrolidine ring. The signal due to the $-NCSS_2$ group (~190) showed a reduced intensity in all complexes as compared to the other carbon atoms because it is a quaternary carbon [9]. In the ^{13}C spectrum of the DTC ligand and complex **Fig. 3.7**, the three signals σ = 212.33 ppm was attributed to the carbon atom of the $-NCSS_2$ group of the DTC ligand, σ = 47.01 ppm attributed to the methylene carbon and σ = 12.96 ppm for the methyl carbon atom of the DTC ligand. Upon complexation, the signals shifted up-field to σ = 194.20 ppm, 46.92 ppm and 12.56 ppm respectively. **Fig. 3.8** shows the ^{13}C of the $PDTC^1$ and $Au(PDTC^1)$ complex with the three signals, σ = 209.51 ppm for the carbon atom of the $-NCSS_2$ moiety, σ = 53.32 ppm and σ = 26.19 ppm

attributed to the carbon atoms of the pyrrolidine ring. After complex formation, an up-field shift was observed to σ = 189.21 ppm, σ = 51.63 ppm and σ = 23.97 ppm respectively. The ^{13}C spectrum of the $PDTC^2$ ligand and Au($PDTC^2$) complex is presented in **Fig. 3.9**. The three prominent signals, σ = 209.08 ppm for the carbon atom of the $-NCSS_2$ moiety, σ = 53.29 ppm and σ = 26.15 ppm are attributed to the carbon atoms of the pyrrolidine ring. As a result of complexation, the signals showed an up-field shift to σ = 185.27 ppm, σ = 51.59 ppm and σ = 23.67 ppm respectively. The ^1H NMR spectra of the free ligands and the complexes are shown in **Fig. 3.4, 3.5 and 3.6.** From all the three complexes, the δ($N^{13}CS_2$) values are ~ 185-194 ppm, which then correlates to the high values of the υC−N stretching mode from the FT-IR spectra, confirming a double bond character (C=N). In the ^1H NMR spectrum of the ligands and complexes there are two persistent peaks, one at ~ 2.52 ppm which is due to the dimethylsulfoxide solvent used and the peak at ~3.50 ppm which is due to water as DMSO is very hygroscopic.

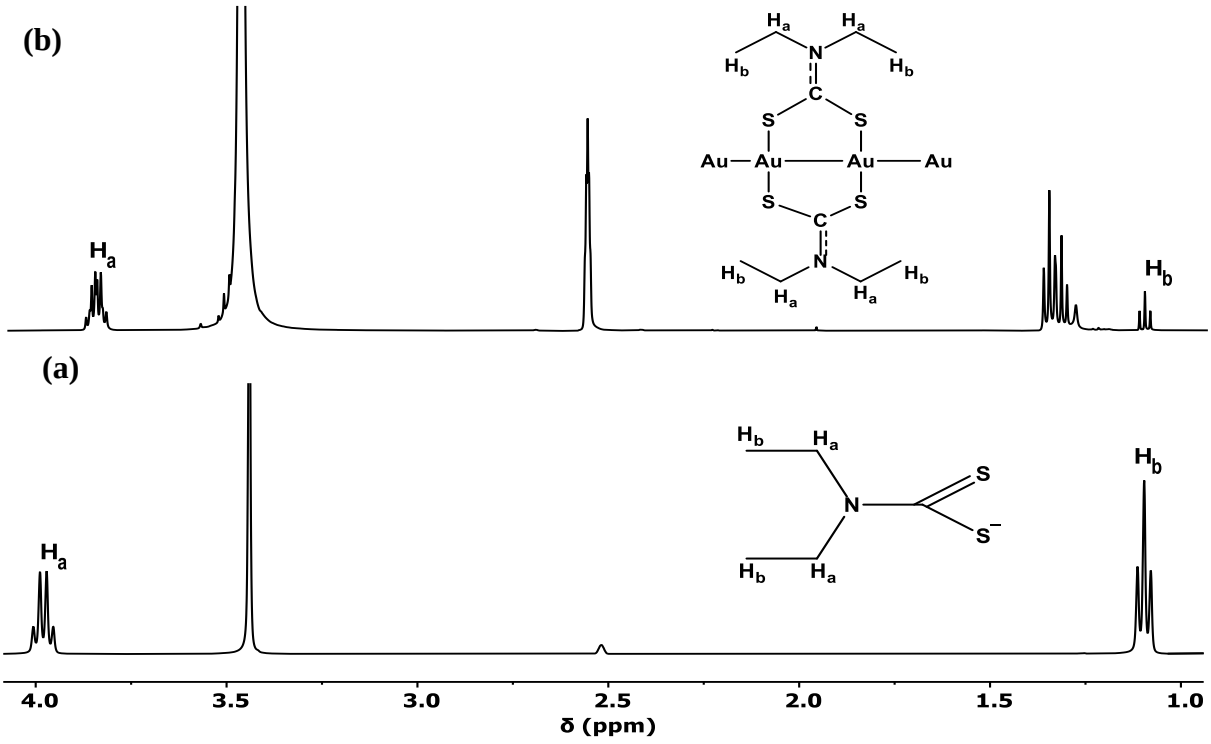

Fig. 3.4: ^1H NMR spectra of (a) Na-DTC ligand and (b) Au(DTC) complex

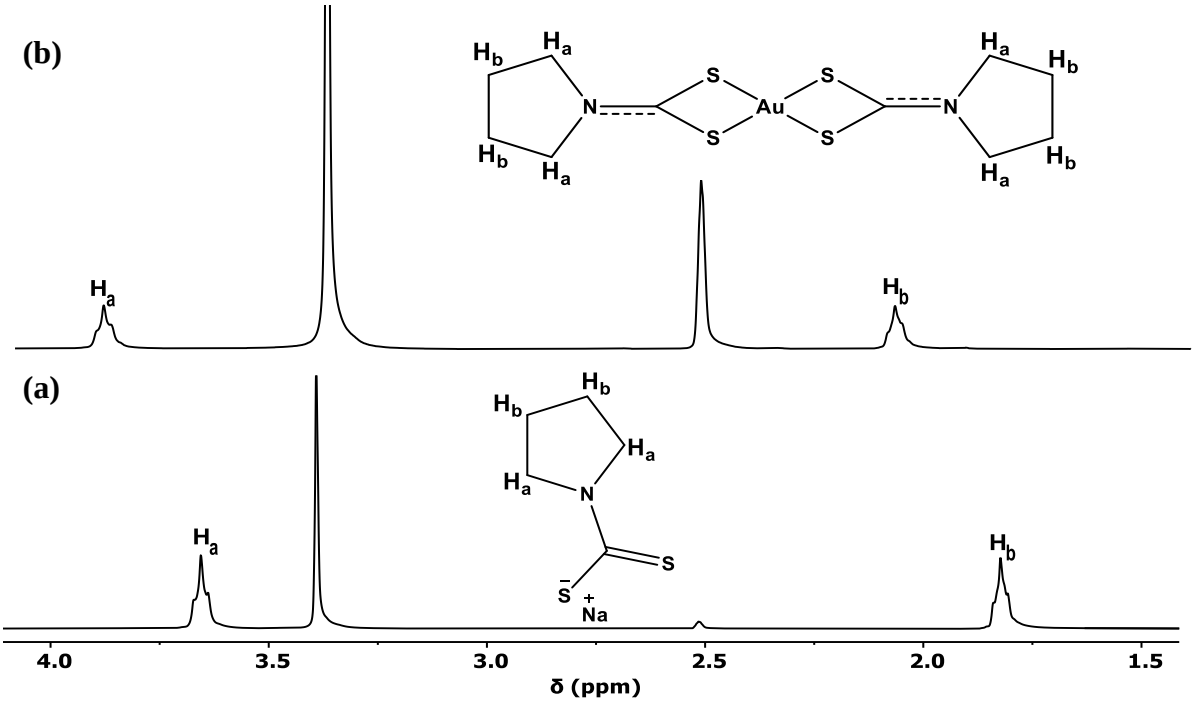

Fig. 3.5: ^{1}H NMR spectra of (a) Na-PDTC ligand and (b) Au(PDTC^{1}) complex.

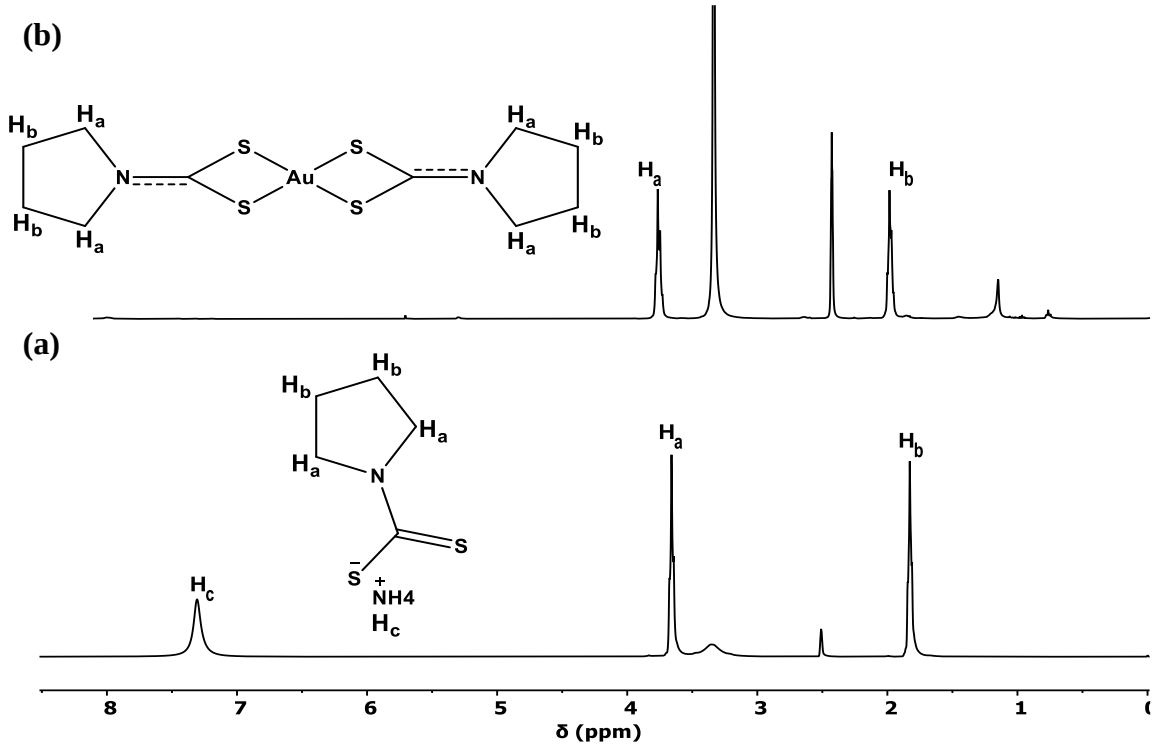

Fig. 3.6: ^{1}H NMR spectra of (a) NH_4-PDTC ligand and (b) Au(PDTC^{2}) complex.

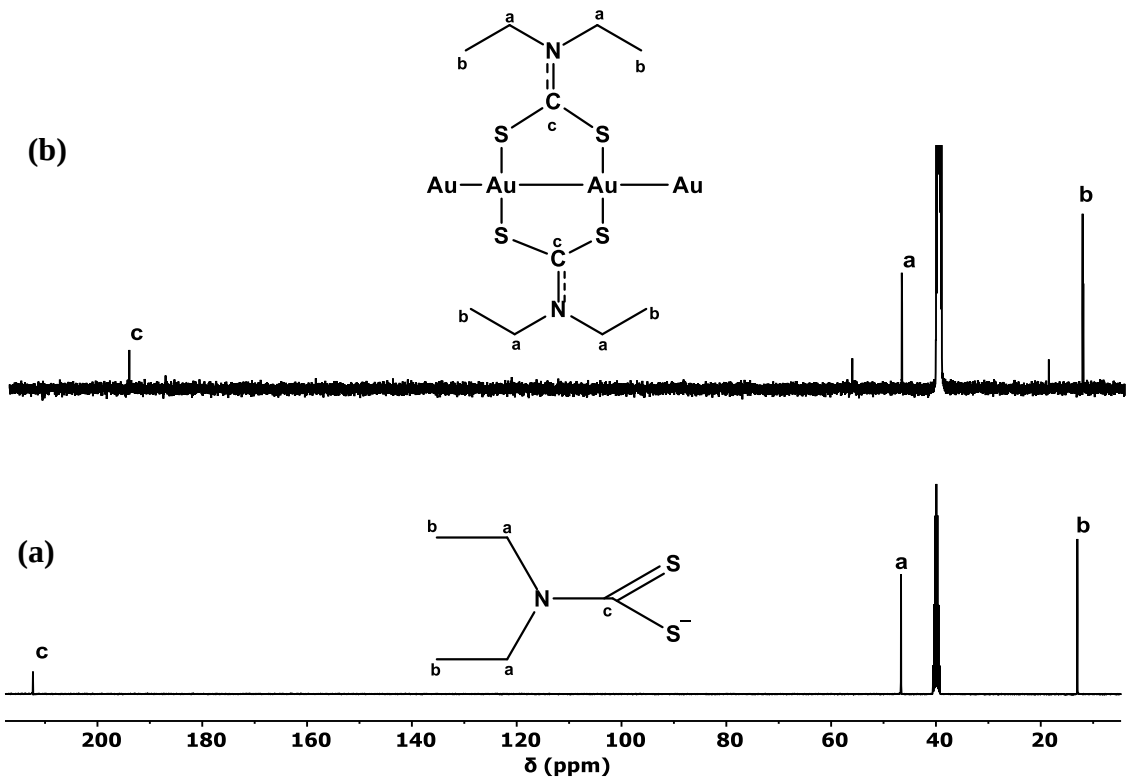

Fig. 3.7: ^{13}C NMR spectra of (a) Na-DTC ligand and (b) Au(DTC) complex

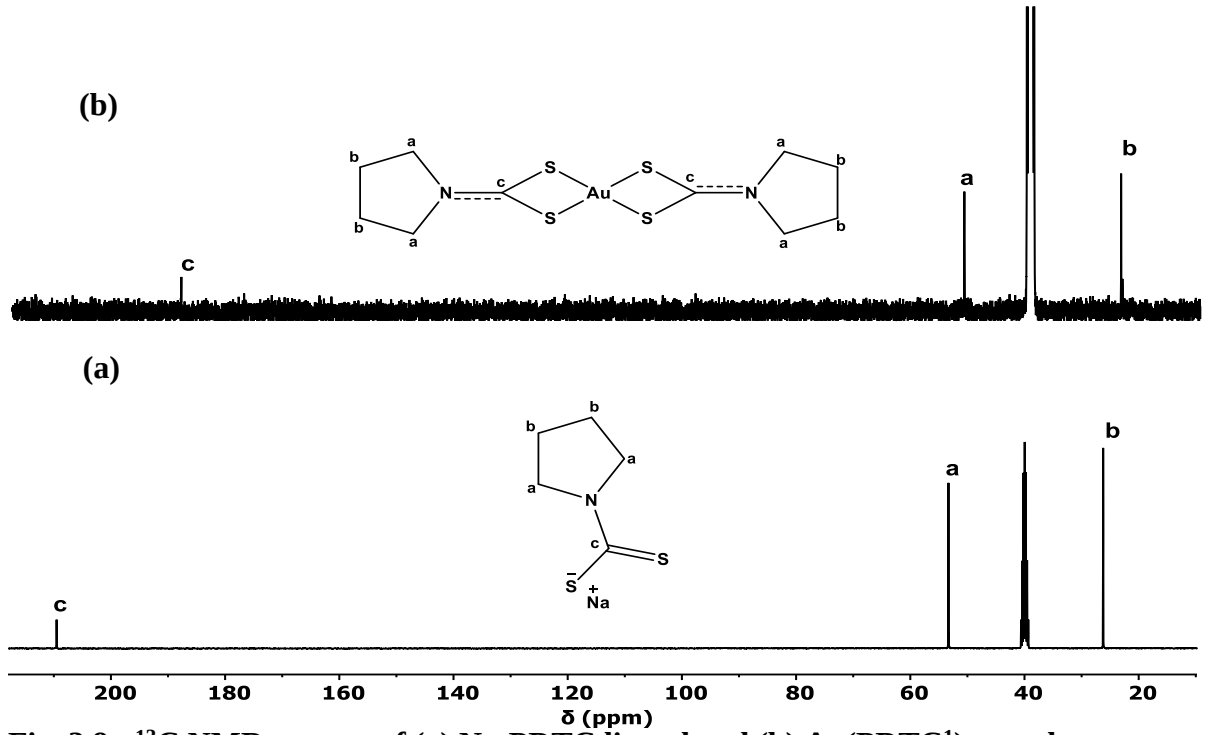

Fig. 3.8: ^{13}C NMR spectra of (a) Na-PDTC ligand and (b) Au(PDTC[1]) complex.

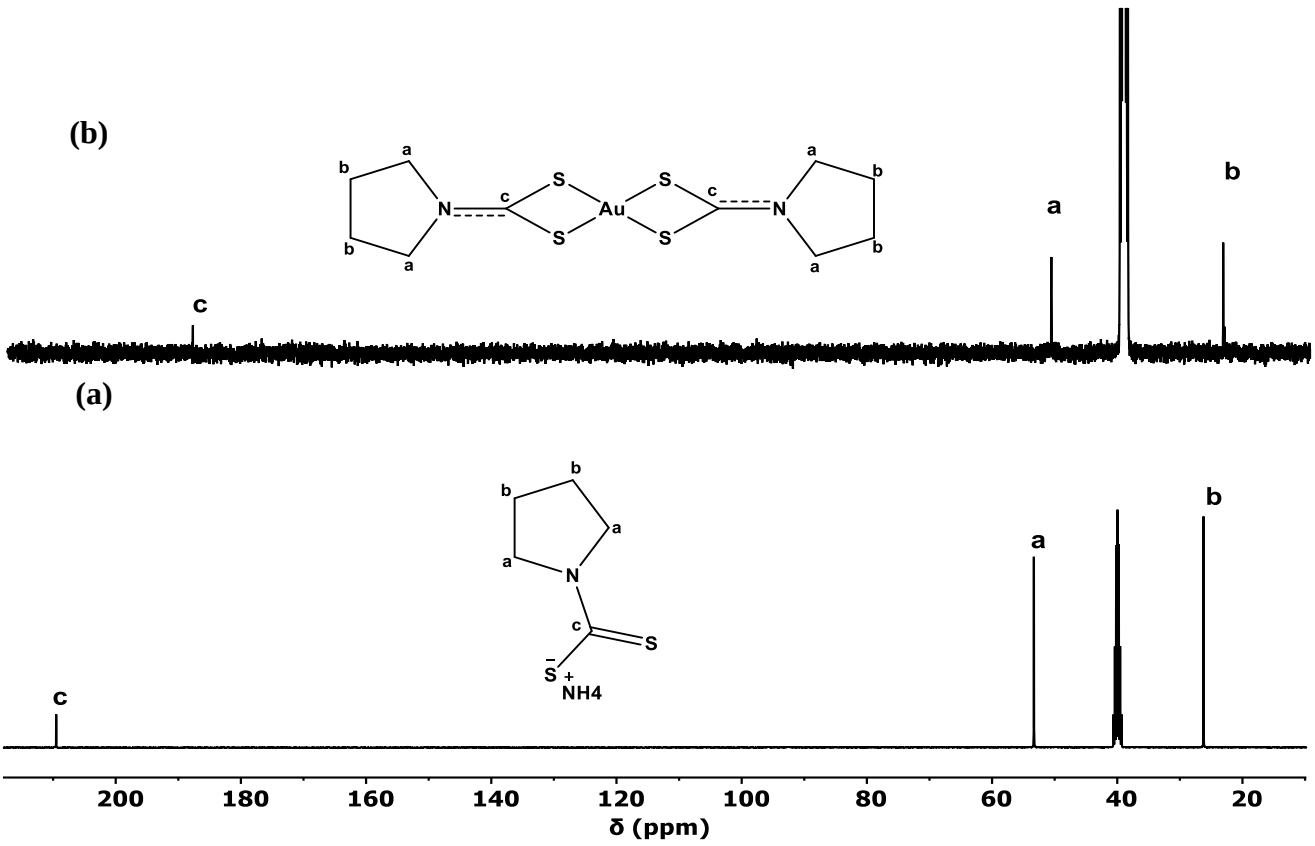

Fig. 3.9: ^{13}C NMR spectra of (a) NH_4-DTC ligand and (b) Au(PDTC^2) complex.

3.4.4 Description of crystal structures

Single crystals of the gold dithiocarbamte complexes suitable for X-ray diffraction were grown from the solution mixture of EtOH and DCM at room temperature by gradual evaporation of the solvent. Details on the crystallographic properties, experiments, and structure refinement for the complexes are summarized in **Table 3.3**. Selected bond distance and angles are summarized in **Table 3.4(a and 4b)** for the Au(DTC) and Au(PDTC) complexes, respectively. The Au(DTC) is a 1-D polymeric chain, as shown in **Fig. 3.10(a)** that crystallizes in the Fddd space group with an orthorhombic crystal system. Within the polymer, $[Au_2(C_4H_{10}NCS_2)_2]$ monomers are joined into $Au^+ \cdots Au^+$ bonded helical filaments, as shown in **Fig. 3.10(b)**. The Au–S bond distance varies between 2.2882(19) Å and 2.2987(18) Å, and the geometry surrounding the Au(I) metal atom is pseudo linear, with the S–Au–S bond angle ranging from 174.72° to 177.97°, like other Au(I) complexes similar to the synthesized Au(DTC) complex as reported in previous work done by Paliwoda et al [11, 15]. The Au(PDTC) complexes crystallize in the triclinic crystal system and P-1 space group, the most disordered of all the crystal systems and the molecular structure is shown

in **Fig. 3.11**. The unit cell is defined by three axes of varying lengths, each with a distinct angle and none of which is equal to 90°. As can be seen, the complex crystallizes with two independent molecules in the asymmetric unit, denoated as molecule I having atom Au1 and molecule II with atom Au2. In both the molecules, two independent pyrollidine dithiocarbamate ligands are bidentately coordinated to the gold atom. The gold atom assumes a distorted square planar geometry with four S atoms belonging to two pyrollidine dithiocarbamte ligands. The distortion arises because of the small S–Au–S bite angles, [S1–Au1–S2 = 75.64 (5), S3–Au2–S3 = 75.90 (5)]. The molecules have an average Au–S bond distance of 2.34 Å is which is similar to that of other gold (III) complexes [16, 17]. For both complexes, Au(DTC) and Au(PDTC), because of the π-delocalization in the S–C–S group, the C–S bond lengths of the N–CS_2 moeity (1.715–1.743 Å) are nearly equal and slightly shorter than usual C–S single bond length (ca. 1.81 Å). To add on, the C–N bond length (1.284–1.329 Å) of the N–CS_2 group in both complexes are in the range of those established for the C=N partial double bond [18]. Both complexes however show voids that are partly filled by CH_2Cl_2 molecules, which may affect the crystal structures, however there is no conclusive evidence for this suggestion.

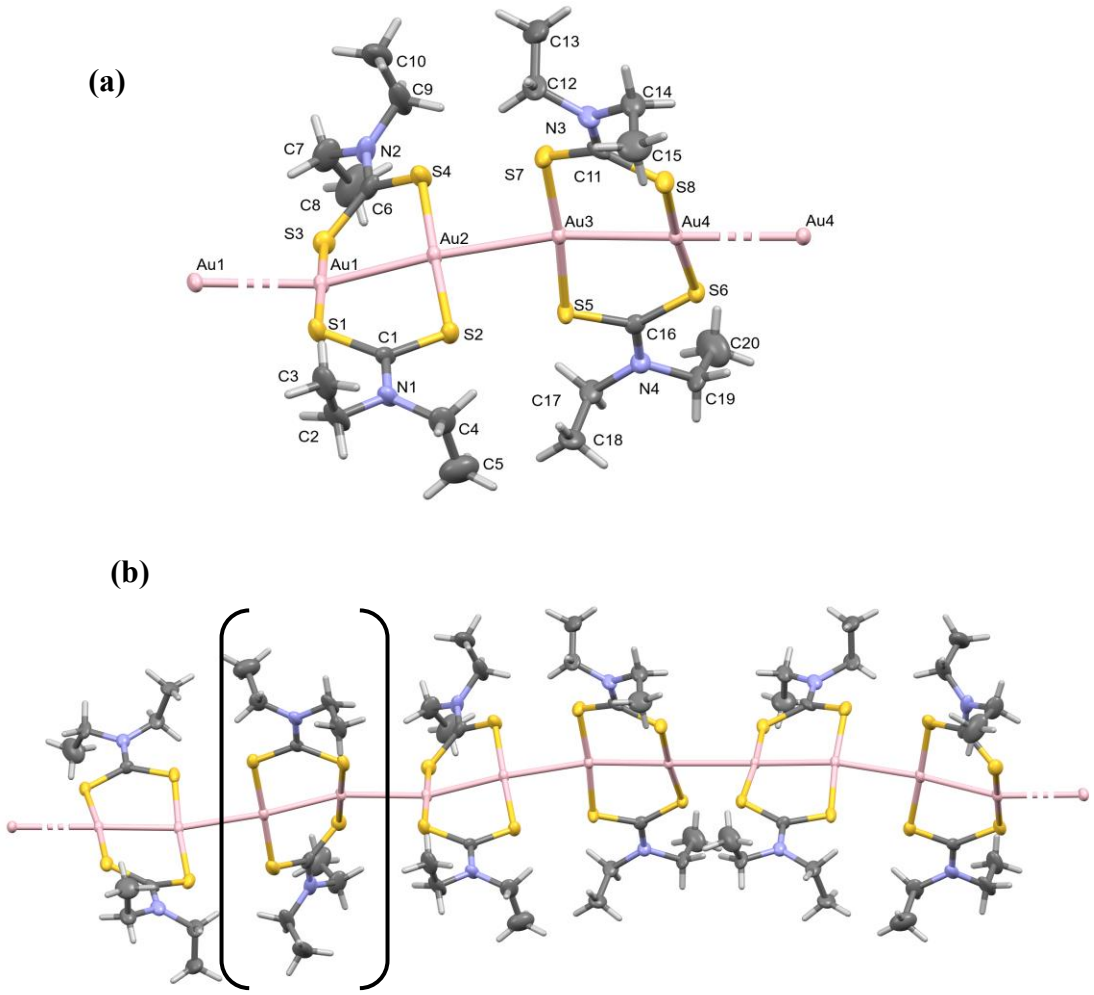

Fig. 3.10: (a) A perspective view of the molecular structure of Au(DTC) complex showing the atom numbering scheme. Atomic displacement parameters are shown at the 50% probability level and (b) Single turns of helix-modulated $Au^{+}\cdots Au^{+}$ bonded filaments viewed perpendicularly and the Au(DTC) monomer has been enclosed in brackets.

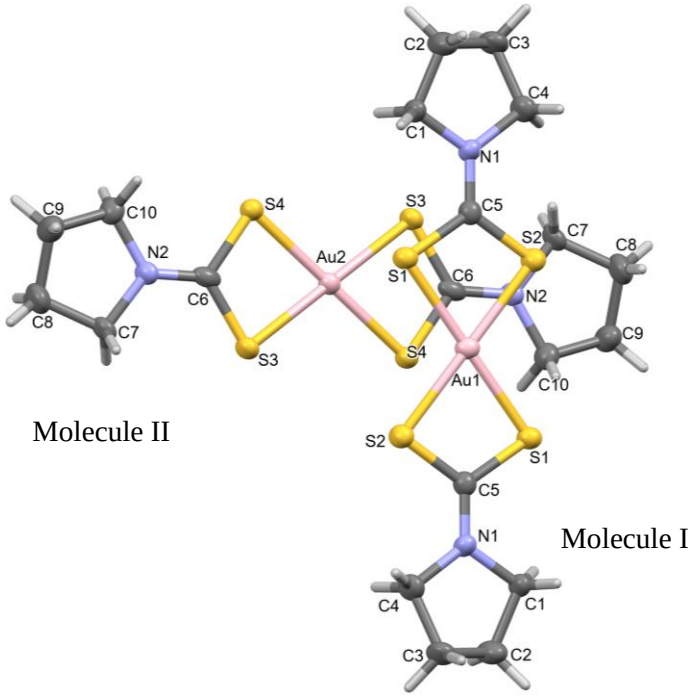

Fig. 3.11: A perspective view of the molecular structure of Au (PDTC) complex showing the atom numbering scheme. Atomic displacement parameters (ADP's) are shown at the 50% probability level.

Table 3.3: Crystallographic characteristics, experimental and structure refinement details for the Au(DTC) and the Au(PDTC) complexes

	$[AuEt_2DTC]_2$	**Au(PDTC)**
Empirical formula	$C_{80}H_{160}Au_{16}N_{16}S_{32}$	$C_{10}H_{16}Au_2N_2S_4$
Formula weight	5523.61	686.35
Temperature/K	173.15	173.00
Crystal system	Orthorhombic	Triclinic
Space group	Fddd	P-1
a/Å	24.6017(4)	8.0509(8)
b/Å	26.1874(4)	10.7595(13)
c/Å	44.9143(7)	10.9033(12)
α/°	90	84.543(4)
β/°	90	87.807(4)

γ/°	90	77.340(4)
V/Å^3	28936.2(8)	917.20(18)
Z	8	2
D_{calc} (g/cm^3)	2.575	2.742
μ/mm^{-1}	16.691	16.714
F (000)	20560.0	692.0
Crystal size (mm^3)	0.158 x 0.121 x 0.064	0.373 x 0.068 x 0.047
Radiation	MoKα (λ = 0.71073)	MoKα (λ = 0.71073)
Reflections collected	86186	55528
Independent reflections	7127 [R_{int} = 0.0928, R_{sigma} = 0.0443]	4601[R_{int}= 0.0890, R_{sigma} = 0.0410]
Goodness-of-fit on F^2	1.057	1.130
Final R indexes [I>=2σ (I)]	R1 = 0.0290, wR2 = 0.0507	R1= 0.0302, wR2 = 0.0693
Largest diff. peak/hole/eÅ^{-3}	0.93/-0.99	1.38/-1.89

Table 3.4a: Selected bond lengths and bond angles for the Au(DTC) complex

Bond	**Distance (Å)**	**Bond**	**Angles (°)**
Au1–Au1^1	2.9453(5)	S1–Au1–Au2	90.92(4)
Au1–S1	2.2928(19)	S1–Au1–S3	176.38(7)
Au1–Au2	2.7660(4)	Au2–Au1–Au1^1	161.685(15)
Au1–S3	2.297(2)	C1–S1–Au1	109.0(3)
S1–C1	1.739(7)	C1–N1–C2	122.7(6)
C1–N1	1.327(8)	C4–N1–C2	113.9(6)
N1–C2	1.575(9)	N1–C1–S1	116.5(5)
N1–C4	1.472(8)	Au1–Au1–Au3	172.282(14)
C1–S2	1.726(7)		
C2–C3	1.521(11)		

Table 3.4b: Selected bond lengths and bond angles for the Au(PDTC) complexes

Bond	**Distance (Å)**	**Bond**	**Angles (°)**
Au1–S1^1	2.3346(15)	S1^1–Au1–S1	180.0
Au1–S1	2.3347(15)	S1–Au1–S2^1	104.36(5)

Au1–S2	2.3388(15)	S1–Au1–S2	75.64(5)
Au1–S2[1]	2.3389(15)	C5–S1–Au1	86.2(2)
S1–C5	1.729(6)	C4–N1–C1	110.9(4)
S2–C5	1.726(6)	C5–N1–C1	123.2(5)
N1–C1	1.492(7)	C5–N1–C4	125.9(5)
N1–C4	1.483(7)	C5–S2–Au1	86.12(19)
N1–C5	1.284(7)	S2–C5–S1	112.0(3)
C1–C2	1.506(8)	N1–C5–S1	123.4(5)
C2–C3	1.531(10)		
C3–C4	1.505(9)		

3.4.5 Electronic spectra of the ligands and complexes

In the ultraviolet region of the electromagnetic spectrum, dithiocarbamate ligands show three bands in relation to intramolecular charge transfer. Band I which corresponds to $\pi \rightarrow \pi^*$ transitions of the N–C=S group, band II which is assigned to $\pi \rightarrow \pi^*$ of S–C=S group and Band III which is assigned to the $n \rightarrow \pi^*$ transitions located on the sulphur [1, 19]. In coordination complexes, the two transitions are from ligands and excitation of metal ions. The transitions from ligands are $\pi \rightarrow \pi^*$ and $n \rightarrow \pi^*$ while transitions because of excitation of the metal ions are d-d transitions [1]. It is usually considered that for gold(I) complexes Au(DTC), the intense peak seen in UV is due to an intramolecular ligand-to-metal charge-transfer transition S(p)→Au(p). On the other hand, gold(III) square-planar complexes [Au(PDTC)], usually show a weak band attributed to d→d metal orbital transitions. This band can be assigned to $^1A_{2g} \leftarrow {}^1A_{1g}$ and $^1E_g \leftarrow {}^1A_{1g}$ transitions (spin allowed but symmetry forbidden) corresponding to the $d_{x^2-y^2} \leftarrow d_{xy}$ and $d_{x^2-y^2} \leftarrow d_{xz,yz}$ transitions, respectively [20, 21]. However, the assignment of this band is still a matter of debate as most authors have ascribed it to intramolecular metal-to-ligand charge transfer from the d orbitals of the metal to the π^* system of the ligands. **Fig 3.12(a)** shows the UV spectra of the DTC and Au(DTC) complex. The ligand shows three bands that are assigned to $\pi \rightarrow \pi^*$ transition (357 nm) attributed to the N–C=S group, $\pi \rightarrow \pi^*$ transition (365 nm) which is due to the S–C=S group and $n \rightarrow \pi^*$ transition (372 nm) which is due to the lone pairs of electrons on the sulfur atoms. The complex showed a shoulder at 362 nm and a band at 523 nm, which was assigned to ligand to metal charge transfer transitions. **Fig. 3.12(b and c)** are similar as they are for the PDTC ligands and complexes. Both

ligands show a peak and a shoulder ascribed to the $\pi \rightarrow \pi^*$ transition attributed to the N–C=S group and the $\pi \rightarrow \pi^*$ transition which is due to the S–C=S group. These are at 322 nm and 430 nm for the $PDTC^1$ ligand and 327 nm and 439 nm for the $PDTC^2$ ligand. The associated complexes show a broad band for the intramolecular transitions and a weak band at a higher wavelength for the d-d transitions. The intramolecular transitions and d-d transitions are at 460 nm, 575 nm for the $Au(PDTC^1)$ complex and 472 nm, 590 nm for the $Au(PDTC^2)$ complex.

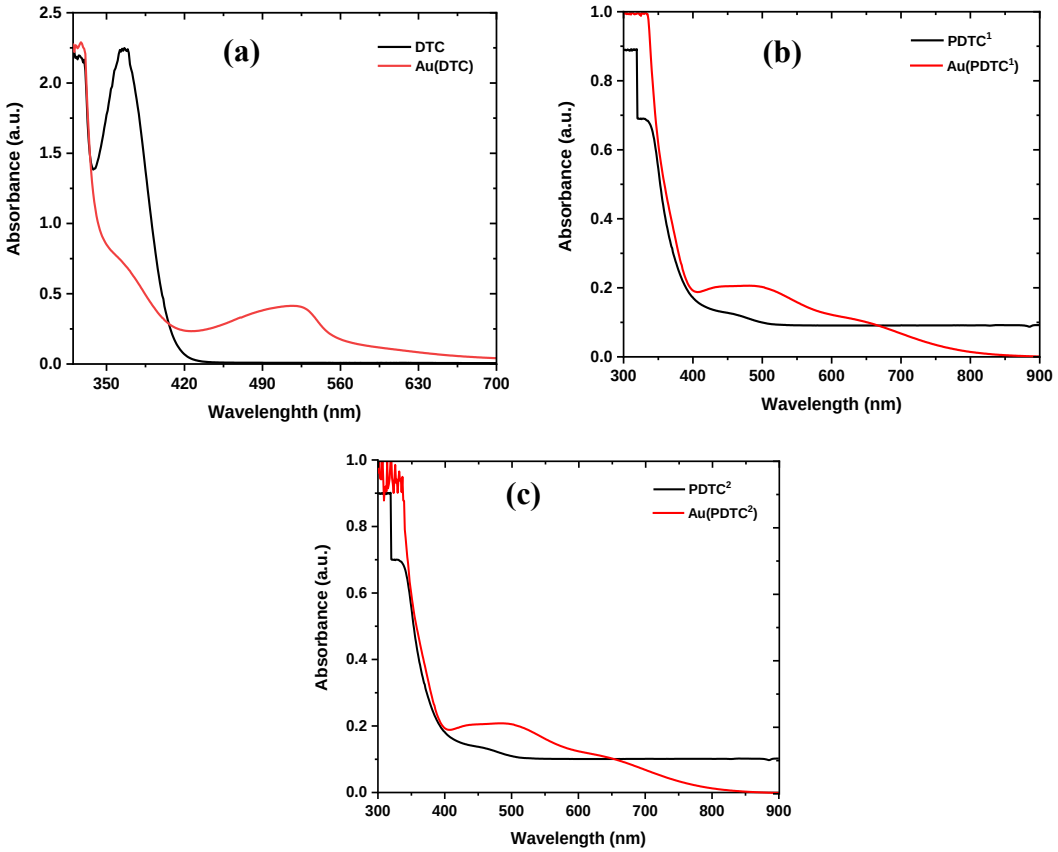

Fig. 3.12: UV-vis absorption spectra of (a) DTC ligand and Au(DTC) complex, (b) Na-$PDTC^1$ and $Au(PDTC^1)$ complex and (c) NH_4-$PDTC^2$ and $Au(PDTC^2)$ complex.

3.4.6 Thermal studies of the complexes

TGA and DTG were used to investigate the thermal characteristics of the complexes at temperatures ranging from 35 to 900 ℃ in a nitrogen environment. **Fig. 3.13(a, b and c)** show the overlapped TGA/DTG graphs of the complexes. The weight per cent graph provided by the TGA illustrates how the quantity of weight changes as the decomposition process advances and on the

other hand, the derivative weight change (DTG) graph displays the rate of each decomposition stage as well as the highest temperature at which each decomposition stage occurs [22]. **Fig. 3.13(a)**, shows the overlapped TGA/DTG graph of the Au(DTC) complex. The TGA curve shows that the decomposition of the complex proceeds in a single step at ~248 ℃, with about 52 % of the complex decomposing to yield the gold (I) sulphide nanostructures. Above 250 °C, no further weight loss was detected, indicating that the gold (I) sulphide is highly stable. **Fig. 3.13(b and c)** show the Au(PDTC) complexes' overlapped TGA/DTG plots. According to them, the two complexes decompose in three stages. The first stage begins at a temperature above 100 °C, meaning that neither water nor solvent molecules are attached to the complexes. The first stage of decomposition is completed at ~213-215 °C where the mass % of 38 and 28 corresponds to the formation of the Au_2S nanostructures for the $PDTC^1$ and $PDTC^2$ respectively [23]. The second stage of decomposition at ~ 290-310 °C involves the decomposition of the remaining organic moiety which constitutes approximately 16 and 26 % of mass of the complex for the $PDTC^1$ and $PDTC^2$ respectively [24]. The third decomposition stage at ~ 430-450 °C results in the expulsion of the remaining organic moiety leaving behind the metal sulfide as the product [25]. However, the third decomposition could be ascribed to the oxidation of some of the sulphur atoms to sulphur dioxide (SO_2). No further weight loss was observed above 450 ℃ for the Au(PDTC) complexes, indicating high stability of the gold (I) sulphide nanostructures.

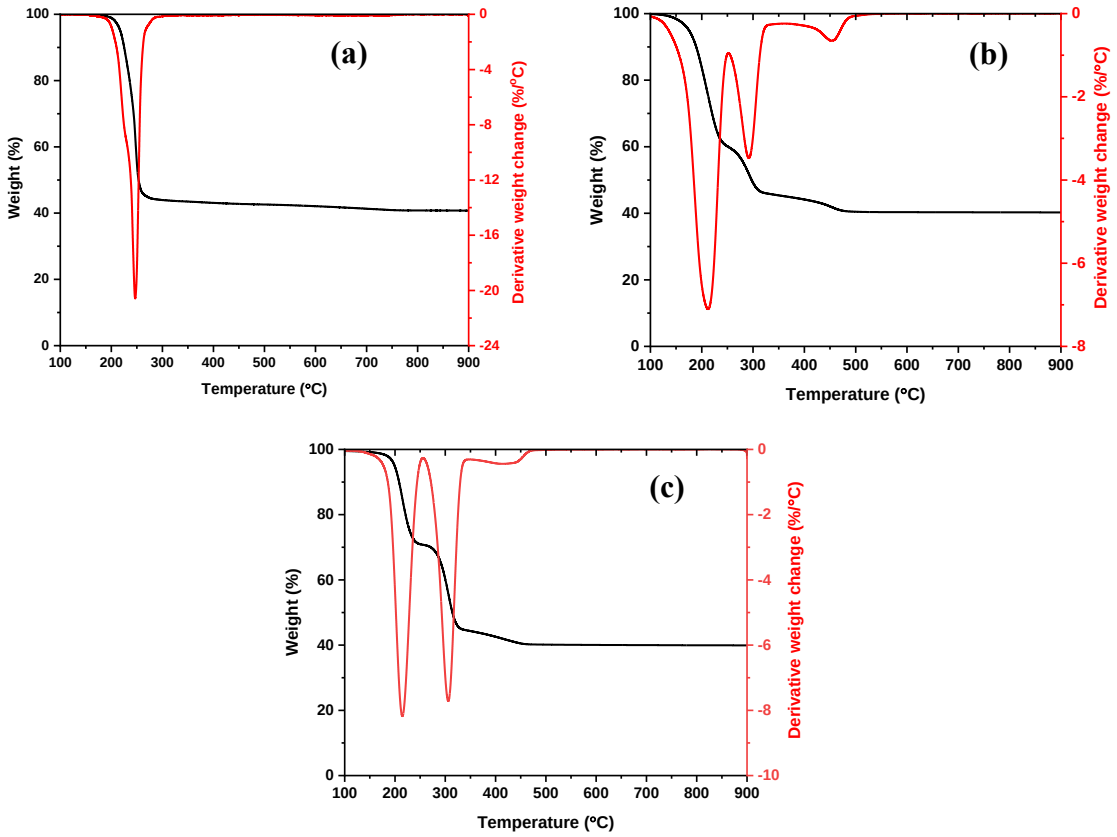

Fig. 3.13: TGA and DTG thermogramse of the dithiocarbamte complexes, (a) Au(DTC), (b) Au(PDTC^1) and (c) Au(PDTC^2).

3.5 Conclusion

Air stable gold dithiocarbamate complexes were sucessfully synthesized and fully characterized by elemental analysis, NMR, and IR spectroscopy, just to mention a few. It has been observed that the dithiocarbamato moiety is symmetrically bonded to the gold metal atom via both sulfur atoms of the –NCS2 group. X-ray crystal structures of the complexes revealed that the gold atom assumes two different oxidation states, gold (I) and gold (III) due to the favourable valence electron arrangements d^{10} and d^8 respectively in the synthesized complexes. Both NMR and FT-IR confirmed successful synthesis of the complexes and it was established that the ^{13}C chemical shifts of the N–CS_2 moiety and the υC−N stretching vibration in the infrared spectra of the complexes were in great correlation. From the TGA curves, the complexes show great potential as single source precursors for the synthesis of gold (I) sulphide nanostructures.

3.6 References

[1] T.A. Odularu, P.A. Ajibade, *Bioinorganic Chemistry and Applications*, 2019, (2019) 8260496.

[2] A.R. Roffey, N. Hollingsworth, H. Islam, M. Mercy, G. Sankar, C.R. Catlow, *Nanoscale*, 8 (2016) 11067-11075.

[3] P. Valarmathi, S. Thirumaran, P. Ragi, S. Ciattini, *Journal of Coordination Chemistry*, 64 (2011) 4157–4167.

[4] J.C. Sarker, G. Hogarth, *Chemical Reviews*, 121 (2021) 6057–6123.

[5] Q. Sha, Y.Y. Wei, *Organic and Biomolecular Chemistry*, 11(2013) 5615–5620.

[6] M.A. Malik, P. O'Brien, N. Revaprasadu, *Chemistry of Materials*, 14 (2002) 2004–2010.

[7] B. Ludolph, M.A. Malik, P. O'Brien, N. Revaprasadu, *Chemical Communications*, 3 (1998) 1849–1850.

[8] W. Kandioller, J. Theiner, B.K. Keppler, C.R. Kowol, Inorganic Chemistry Frontiers, 9 (2022) 412–416.

[9] F.F. Bobinihi, J. Osuntokun, D.C. Onwudiwe, *Journal of Saudi Chemical Society*, 22 (2018) 381–395.

[10] A. Manohar, K. Karpagavel, A. Murugan, *International Journal of ChemTech Research*, 6 (2014) 474–480.

[11] S.S. Al-Jaroudi, M. Altaf, A.A. Seliman, S. Yadav, F. Arjmand, A. Alhoshani, H.M. Korashy, S. Ahmad, A.A. Isab, *Inorganica Chimica Acta*, 464 (2017) 37–48.

[12] D.C. Onwudiwe, P.A. Ajibade, *Polyhedron*, 29 (2010) 1431–1436.

[13] A.A. Sulaiman, A. Muhammad, A. Anvarhusein, A. Isab, A. Alawad, S. Altuwaijri, S. Ahmad, *Journal of inorganic and general chemistry*, 00 (2016) 00278.

[14] H.L.M.V. Gaal, J.W. Diesveld, F.W. Pijpers, J.G.M.V.D. Linden, *Inorganic Chemistry*, 18 (1979) 3251–3260.

[15] D. Paliwoda, P. Wawrzyniak, A. Katrusiak, *Journal of Physical Chemistry Letters*, 5 (2014) 2182–2188.

[16] M. Baron, A. Dall'Anese, C. Tubaro, L. Orian, V. Di Marco, S. Bogialli, C. Graiff, M. Basato, *Dalton Transactions*, 47 (2018) 935–945.

[17] A.H. Mageed, B.W. Skelton, M.V. Baker, *Dalton Transactions*, 46 (2017) 7844–7856.

[18] E. Sathiyaraj, S. Thirumaran, S. Ciattini, S. Selvanayagam, *Inorganica Chimica Acta*, 498,

(2019) 119162.

[19] M.R.L. Oliveira, V.M. De Bellis, *Transition Metal Chemistry*, 24 (1999) 127–130.

[20] L. Ronconi, L. Giovagnini, C. Marzano, F. Bettìo, R. Graziani, G. Pilloni, D. Fregona, *Inorganic Chemistry*, 44 (2005) 1867–1881.

[21] F. Forghieri, C. Preti, L. Tassi, G. Tosi, *Polyhedron*, 7 (1988) 1231–1237.

[22] PerkinElmer, 1960, http://las.perkinelmer.com/Catalog/TechLibDetails.htm?expand=Application%20Notes&ObjectId=Thermogravimetry+%5bTGA%2c+TG%2fDTA%5d&CategoryID=Thermogravimetry+%5bTGA%2c+TG%2fDTA%5d&type=CATEGORY.com accessed on 5 January 2022.

[23] S. Singhal, A.N. Garg, K. Chandra, *Journal of Thermal Analysis and Calorimetry*, 78 (2004) 941–952.

[24] K.S. Siddiqi, S.A.A. Nami, S. Lutfullah, Y. Chebude, *Journal of Brazilian Chemical Society*, 17 (2006) 107–112.

[25] S. Khan, S.A.A. Nami, K.S. Siddiqi, *Journal of Molecular Structure*, 875 (2008) 478–485.

CHAPTER 4

Synthesis of Au_2S nanostructures from a dithiocarbamate gold complex as a single-source precursor: the effect of the nature of the precursor, temperature, time, and concentration on the properties of Au_2S nanostructures

4.1 Introduction

The development of metal sulfide nanoparticles has sparked a surge in interest in nanoscience and nanotechnology in the domains of materials science and engineering due to their interesting properties and applications [1, 2]. Metal sulphides are semiconductors with size-dependent properties that have found use in various applications such as fuel cells, solar cells, light emitting diodes, sensors, lithium ion batteries and supercapacitors [3, 4]. In spite of the wide applications of the metal sulphides, some sulphides such as gold sulphide have been less explored. Gold sulphide was of particular interest because firstly the bulk material is a p-type semiconductor, secondly, gold and sulfur salts are utilized to assist the photographic process by sensitizing silver halide crystals, thirdly, ab initio calculations show that the Au-S bond in Au_2S dimers is more covalent than ionic, which could affect the properties of their small particles and fourthly, contrasting and comparing the optical characteristics of Au_2S nanostructures with other coinage metal sulphides such as copper (Cu) and silver (Ag) would be fascinating [5–7]. In addition, the nature of gold-sulfur bonding because alkanethiol monolayers on gold surfaces [8] have sparked a lot of curiosity in recent research.

There have been numerous methods used to synthesize metal sulphide nanoparticles. The colloidal method employing the use of metal complexes as single-source precursors have gained prominence over the last decades due to their advantages over the dual-precursor method. The single-source precursor method is insensitive to air and moisture since it avoids adding precursors after the reaction has begun because the precursor already includes all the chemical elements needed to make the nanoparticles. In addition, with the single-source precursor method there is better control over the size and shape of the nanoparticles, ease of separation of the nanocrystalline

material and decomposition of the organometallic complexes usually occurs at relatively low temperatures [9–11]. Metal dithiocarbamate complexes have been widely used in the synthesis of metal sulphide nanoparticles and some examples are summarized in **Table 4.1**. However, in spite of the diethyldithiocarbamate gold complex being reported [12, 13] no studies on its use in the synthesis of Au_2S nanostructures has been reported, hence herein, we study the use of gold diethyldithiocarbamate complex as a single-source precursor for the synthesis of Au_2S nanostructures.

Table 4.1: Summarized examples of metal dithiocarbamates and their respective metal sulphides

Complex	Nanoparticle	Reference
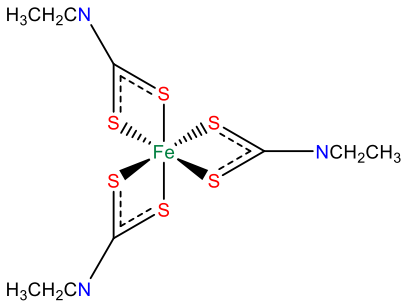	FeS_2	[14]
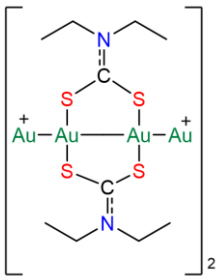	Au(DTC)	[13]
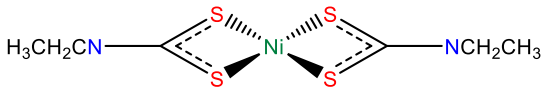	Ni_3S_4	[15]

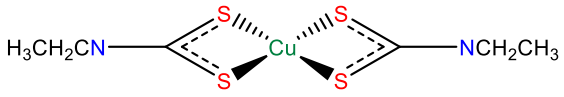

Cu_2S [16]

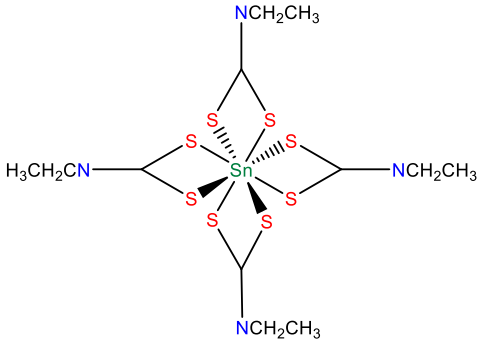

SnS_2 [17]

Various factors have been shown to affect the properties of nanoparticles. The growth mechanism in the colloidal synthesis of nanocrystals is that described by Lamer and Dinegar. The precursors are first transformed to monomers, then nuclei and ultimately stable nanocrystals are formed through the Ostwald ripening process. The nature of the precursor therefore controls the formation of the monomers, which in turn result in the formation of the nuclei. The formation of the nuclei must be rapid to minimize the formation of nuclei with different sizes hence resulting a polydispersed sample, secondly an appropriate precursor will result in a decoupled nucleation and growth phase. This ensures that the particles grow in a controlled manner and no polydispersity is observed [18, 19]. Kolokoto et al. [20] studied the effect of changing selenium precursors on the properties of Nb_2Se_9 nanoparticles and they found that the Nb_2Se_9 nanoparticles changed from flower-like morphologies to rod-like morphologies when the selenium precursor was changed from elemental selenium to selenide oxide and selenourea. In another study, Sreekumari et al. [21] studied the effects of single molecule precursors on the synthesis of CdS nanoparticles. They report that well defined spherical shaped nanoparticles of CdS were synthesized from bis(methylhexyldithiocarbamato) cadmium (II), $[Cd(S_2CNMeHex)_2]$ and rod-like shaped CdS nanoparticles were synthesized from a thiosemicarbazide complex of cadmium $Cd(NH_2CSNHNH_2)_2Cl_2$. In addition to the nature of the precursor, temperature also plays a critical role on the growth dynamics of the nanoparticles. For example, Ghamsari et al. [22] found that the temperature of the reaction has a significant effect on the nucleation and growth of nanoparticles

as increasing the temperature leads to a decrease in supersaturation of the precursors and thus resulting in an increase in the size of the nucleus. A similar effect of temperature on the properties of nanoparticles was reported by Akinbami et al. [23] who reported an increase in the size of $CsZnBr_2$ perovskite nanocrystals with increasing reaction temperature. Reaction time is one other factor that greatly influences the properties of synthesized nanoparticles. For example, Manzoor et al. and Akinbami et al. [23, 24] reported that longer reaction times (higher nucleation times) yield larger nanoparticles, and this is because of the Ostwald ripening process. Precursor concentration additionally affects the properties of the synthesized nanoparticles as higher concentrations favor larger nanoparticles and lower concentrations favor smaller nanoparticles. This has been demonstrated by the work done by Sibokoza et al. and Moloto et al. [25, 26] who were able to synthesize nanoparticles at various precursor concentrations and found that as the precursor concentration was decreased, the nanoparticles size decreased and became mono-dispersed. Therefore, herein, we further study the influence of the nature of the precursor, temperature, reaction time and concentration on the properties of Au_2S nanostructures.

4.2 Experimental Section

4.2.1 Materials

Gold diethyldithiocarbamate Au(DTC), gold pyrrolidine dithiocarbamate Au($PDTC^1$), gold pyrrolidine dithiocarbamate Au($PDTC^2$), oleylamine (70%), oleic acid (90%), 1-octadecene (90%), toluene (anhydrous, 95%), chloroform-d (99.8 atom % D) were purchased from Sigma Aldrich and used without any purification.

4.2.2 Synthesis of Au_2S nanostructures

To a mixture of 10 mmol of OLA, 10 mmol of OA and 20 mmol of 1-ODE in a three-necked round bottom flask, 0.1 mmol of either Au(DTC) or Au(PDTC) was added at room temperature. The slurry was then heated to 100 ℃ to remove any residual water and oxygen with vigorous magnetic stirring under nitrogen for 20 min. Then the solution was heated to 170 ℃ under nitrogen and held there for 45 min. After the time elapsed, the final solution was allowed to cool down naturally to 80 ℃ before adding ethanol and collecting the nanostructures by centrifugation, (yield 63 %). The nanostructures were washed with ethanol twice and allowed to air dry before characterization.

Each of the following reaction parameters: nature of precursor, temperature, reaction time, and precursor concentration were varied as shown in **Table 4.2**.

Table 4.2: Summary of the reaction conditions for the synthesis of Au_2S nanostructures

Single-source Precursor	Temperature (℃)	Time (min)	Concentration (M)	Capping Agent
Au(DTC)	140	45	3.837	OLA, OA
	170	30	3.837	OLA, OA
	170	45	3.837	OLA, OA
	170	60	3.837	OLA, OA
	170	45	1.918	OLA, OA
	170	45	0.837	OLA, OA
	170	45	7.674	OLA, OA
	200	45	0.837	OLA, OA
Au($PDTC^1$)	170	45	3.821	OLA, OA
Au($PDTC^2$)	170	45	3.821	OLA, OA

4.2.3 Characterization

The as-synthesized nanostructures were characterized using powder X-ray diffraction (PXRD) on a Bruker MeasSrv D2-205530 diffractometer using secondary graphite monochromated Cu-Kα radiation (λ = 1.54060 Å) at 30 kV/10 mA. Measurements were taken using a glancing angle of incidence detector at an angle of 2°, for 2θ values between 10 - 90° in steps of 0.026° with a step time of 37 s and at a temperature of 25 °C. The sample morphologies were determined using FEI Technai T12 Transmission Electron Microscope (TEM), operated at 120 kV with a beam spot size of 3 in TEM mode. After dispersing the samples in ethanol and sonicating them for 30 minutes, a drop of the suspended nanostructures was placed on a lacey-carbon copper grid and allowed to dry

at room temperature before analysis. The absorption measurements were carried out using a Specord 210 AnalytikJena UV-vis spectrophotometer after dispersing the nanoparticles in toluene and placing them in a quartz cuvette (1 cm path length). A HORIBA QM8000 spectrofluorometer with a PPD-850 detector was used to measure the photoluminescence of powdered samples. The X-ray photoelectron spectroscopy (XPS) measurements of the powdered samples were obtained using a Physical Electronics PHI 5700 spectrometer using non-monochromatic Mg Kα x-rays (300 W, 15 kV, and 1253.6 eV) as the excitation source and a pressure of $<10^{-8}$ mBar. The spectrometer energy scale was calibrated using Cu 2p3/2, Ag 3d5/2, and Au 4f7/2 photoelectron lines at 932.7, 368.3, and 84.0 eV, respectively. The FT-IR spectra were measured on a Bruker Tensor 27 FT-IR and the nuclear magnetic resonance (NMR) data was obtained using a 500 MHz Bruker AVANCE III; the samples were run using $CDCl_3$ as a solvent at room temperature. The Raman spectrum was obtained by placing the sample on a glass slide and viewed under the microscope using the Bruker Raman Senterra Spectrophotometer using the 785 nm excitation laser and at a very low laser power of 0.04 mW. Scanning electron microscopy (SEM) was carried out on a FEI Nova Nanolab 600 FIB/SEM microscope equipped with an EDX detector. The powder samples were coated with gold and mounted on aluminium stubs with carbon tape.

4.2.4 Results and discussion

4.2.4.1 Synthesis of Au_2S nanostructures

The single-source precursor method involves the decomposition of a molecular precursor, usually organometallic molecules to form the desired products **Scheme 4.1**. The selected precursor contains both the desired metal and corresponding chalcogen elements, which can therefore decompose under the right conditions to give metal chalcogenide compounds directly. The decomposition of the gold diethyldithiocarbamate complex is depicted in **Scheme 4.1**.

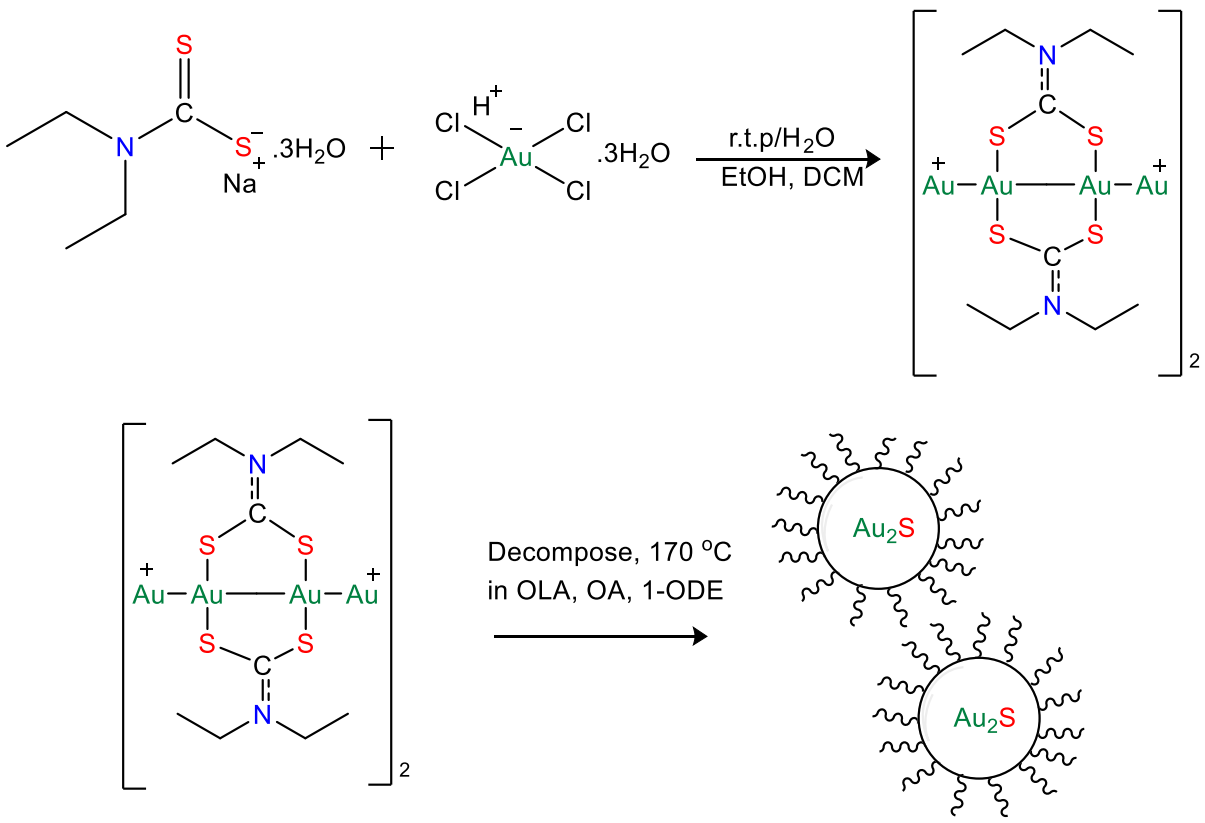

Scheme 4.1: The synthesis of Au_2S nanostructures from gold diethyldithiocarbamate single-source precursor.

4.2.4.2 Characterization of Au_2S nanostructures

X-ray powder diffraction (XRD) analysis was used for confirmation and phase identification of the synthesized Au_2S nanostructures. The XRD pattern of the synthesized Au_2S nanostructures with the standard reference pattern is presented in **Fig. 4.1(a)**. The pattern showed peaks at 2θ values of 30.82°, 35.74° and 51.44° which were assigned to the diffraction planes (111), (200) and (220), respectively. The Au_2S nanostructures were indexed to a pure Au_2S (PDF: 01-085-1997) with cubic crystal phase and space group Pn-3m (224). The diffraction peaks are broad indicating the small size of the synthesized Au_2S nanostructures. The particle size was estimated by the Debye Scherrer equation and the sizes were estimated to be 3.8 nm.

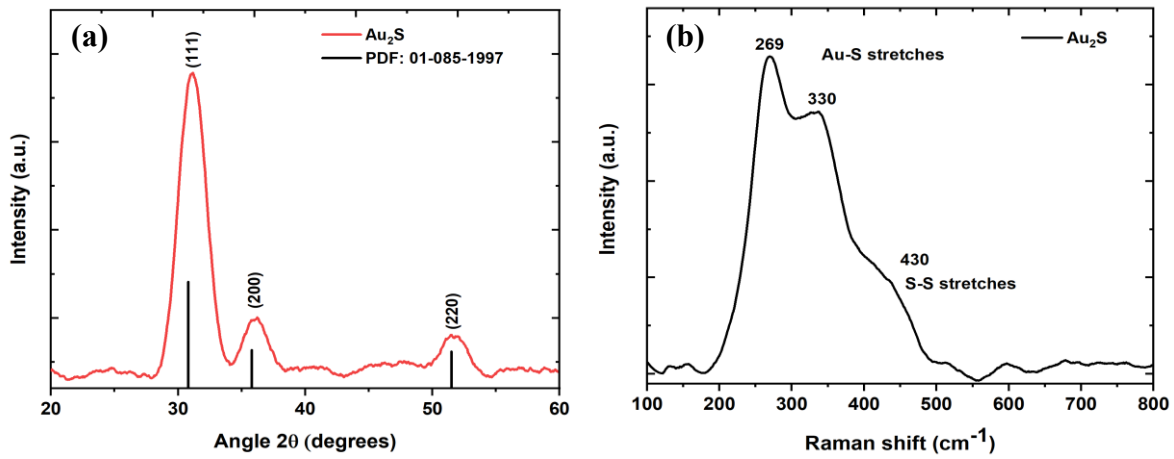

Fig. 4.1: (a) Powder X-ray diffraction patterns of Au_2S matched to standard powder pattern of Au_2S and (b) Raman spectrum of the Au_2S nanostructures.

To understand the chemical structure and molecular interactions of the Au_2S nanostructures, Raman spectroscopy was conducted, and the spectrum is shown in **Fig. 4.1(b)**. The Raman spectrum showed a surface enhanced peak at 269 cm^{-1} and another peak at 330 cm^{-1} attributed to the Au-S stretching vibration. The shoulder peak at 430 cm^{-1} was attributed to the S-S stretching vibration. The Au-S stretching vibrations have shown to be consistent with the formation of Au_2S nanostructures [27]. The size and shape of the particles was analysed by TEM, and the results are depicted in **Fig. 4.2(a)**. From the TEM images, the synthesized Au_2S nanostructures showed a quasi-spherical morphology, and the nanostructures were polydispersed and some agglomeration was observed. The histogram of the Au_2S nanostructures **Fig. 4.2(b)** indicated an average particle size of $3\pm$ 0.8 nm and this was in agreement with the sizes estimated from XRD.

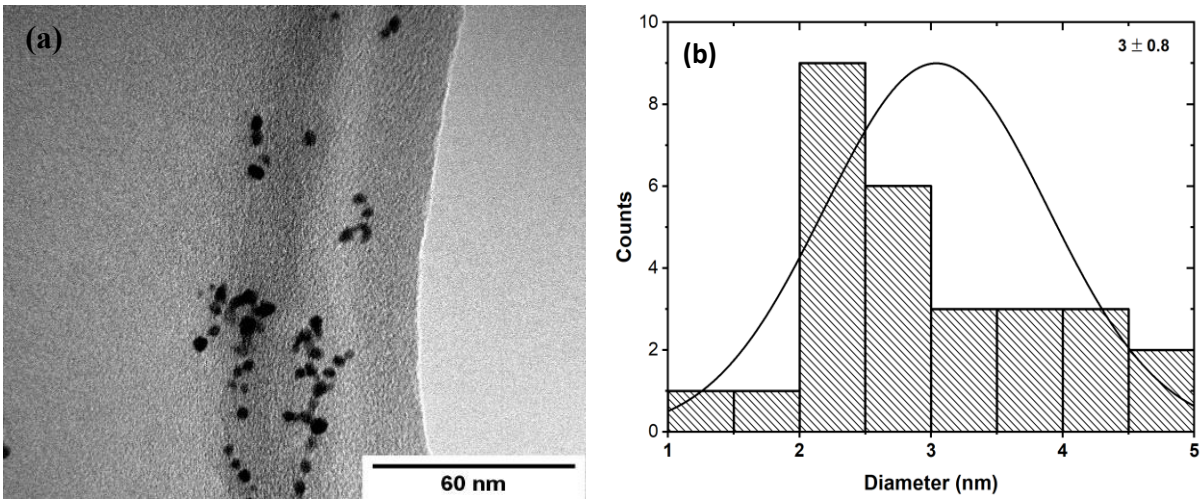

Fig. 4.2: (a) TEM image and (b) corresponding size distribution of Au_2S nanostructures.

To further investigate the morphology of the synthesized Au_2S nanostructures, in particular the surface morphology, the scanning electron microscopy (SEM) technique was employed. However, as with the TEM, the synthesized nanostructures were highly agglomerated, and it was impossible to obtain clear images. A closer look at **Fig. 4.3(a)** shows the synthesized nanostructures as quasi-spherical in shape, despite their agglomeration. Elemental composition of the Au_2S nanostructures was confirmed by EDS analysis as illustrated in **Fig. 4.3(b)** and only the Au and S peaks were observed. The atomic percentages of Au and S are 87.6 % and 12.4 % respectively. As can be seen from the EDX spectrum, the Au and S appear at about the same peak position. From the periodic energy table for EDX analysis, Au and S have peaks at 2.120 and 2.307 keV respectively, and since these peaks are separated by 187 eV, the software cannot tell the difference, as the resolution in EDX is roughly 120-130 eV [28].

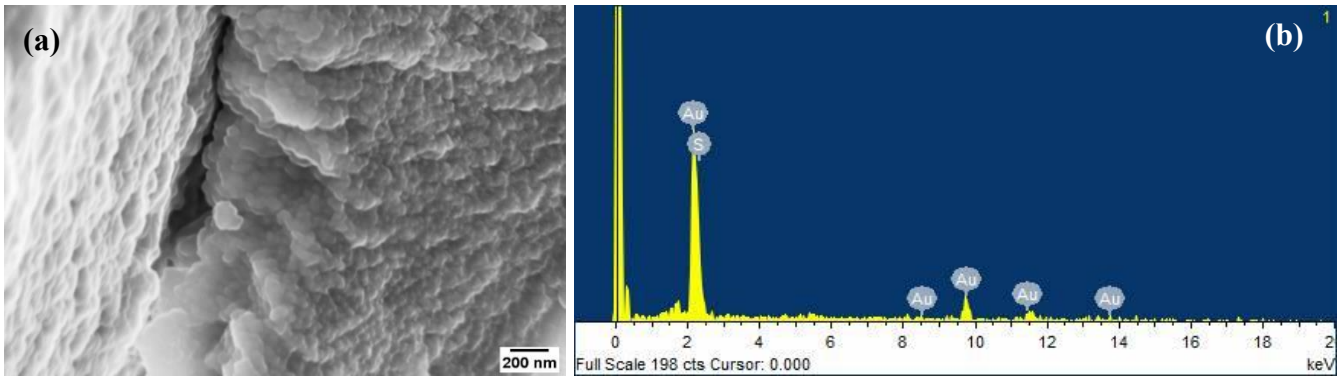

Fig. 4.3: (a) SEM image and (b) EDS spectrum of the synthesized Au_2S nanostructures.

XPS was carried out on the synthesized Au_2S nanostructures to evaluate the surface chemistry and the bonding involved in the nanostructures. Shown in **Fig. 4.4(a)** is the survey spectrum that showed the elemental composition of the Au_2S nanostructures including the N 1s, and C 1s associated with the capping agents OLA and OA. The O 1s observed in the survey spectrum was due to the OA capping agent or the oxidation of the capping agent and not the oxidation of Au_2S as no oxide peaks were observed in XRD [29]. The high-resolution spectrum of the C 1s was deconvoluted to two main peaks corresponding to C-C and C-O of the capping agents **(Fig. 4.4b)**. The existence of the C-C at 284.6 eV was attributed to the capping agents' lengthy alkyl chains whereas the C-O at 285.8 was likely from the oxidation of the capping agents on the surface of the nanostructures. The 400.7 eV N 1s peak was attributed to organic N **(Fig. 4.4c)** [29], which is derived from the OLA utilized in the Au_2S synthesis. This is proof that OLA was successfully capping the nanostructures' surface. The Au 4f high-resolution spectrum showed two peaks at 87.1 eV and 83.4 eV for the Au($4f_{5/2}$) peak and the Au($4f_{7/2}$) peak respectively **(Fig. 4.4d)**. Interestingly, the binding energy for the Au($4f_{7/2}$) peak of Au_2S is the same as that of metallic gold (Au^0). This observation is surprising as it would suggest that the gold atoms in the clusters must be present largely as Au^0, suggesting that the Au^+ in Au_2S gets reduced to Au^0, however theoretical calculations on the binding energy of the Au_2S suggest a partial positive charge on the Au atom. As a result, there is a small transfer of electronic density from Au to S atoms in the Au_2S owing to covalent bonding, which results in the binding energies close to that of elemental Au [26, 28, 29]. The high-resolution spectrum of S 2p **(Fig. 4.4e)** was deconvoluted into two peaks, $2p_{1/2}$ and $2p_{3/2}$ with binding energies of 162.9 eV and 161.6 eV. The S ($2p_{3/2}$) binding energy in the Au_2S is consistent with a less negative charge on the sulphur atom. This is consistent with a comparison

with other metal sulphides. For example, in metal sulphides, such as PbS, HgS, and CdS, the S atom is formally assigned an oxidation number of 2-, and the S($2p_{3/2}$) binding energy is ~161-162 eV [30]. Thus, the XPS measurements give a supposition that the Au_2S exhibits a significant amount of covalent bond character. Due to the low intensity of the O 1s peak **(Fig. 4.4f)** and an atomic composition of 2.7%, no additional information regarding the nature of the capping agents could be conclusively deduced. The percentage compositions of the present species are shown in **Table 4.3**.

Table 4.3: Summary of the bonding configuration and elemental composition data obtained from the XPS spectra of Au_2S

Element	Assignment	Binding energy (eV)	Atomic %
Au	Au $4f_{5/2}$	87.1	10.8
	Au $4f_{7/2}$	83.4	10.8
S	S $2p_{1/2}$	162.9	7.9
	S $2p_{3/2}$	161.6	8.4
C	C-C	284.6	71.2
	C-O	285.8	4.1
N	Organic N	400.9	2.8
O	Organic O	532.3	2.7

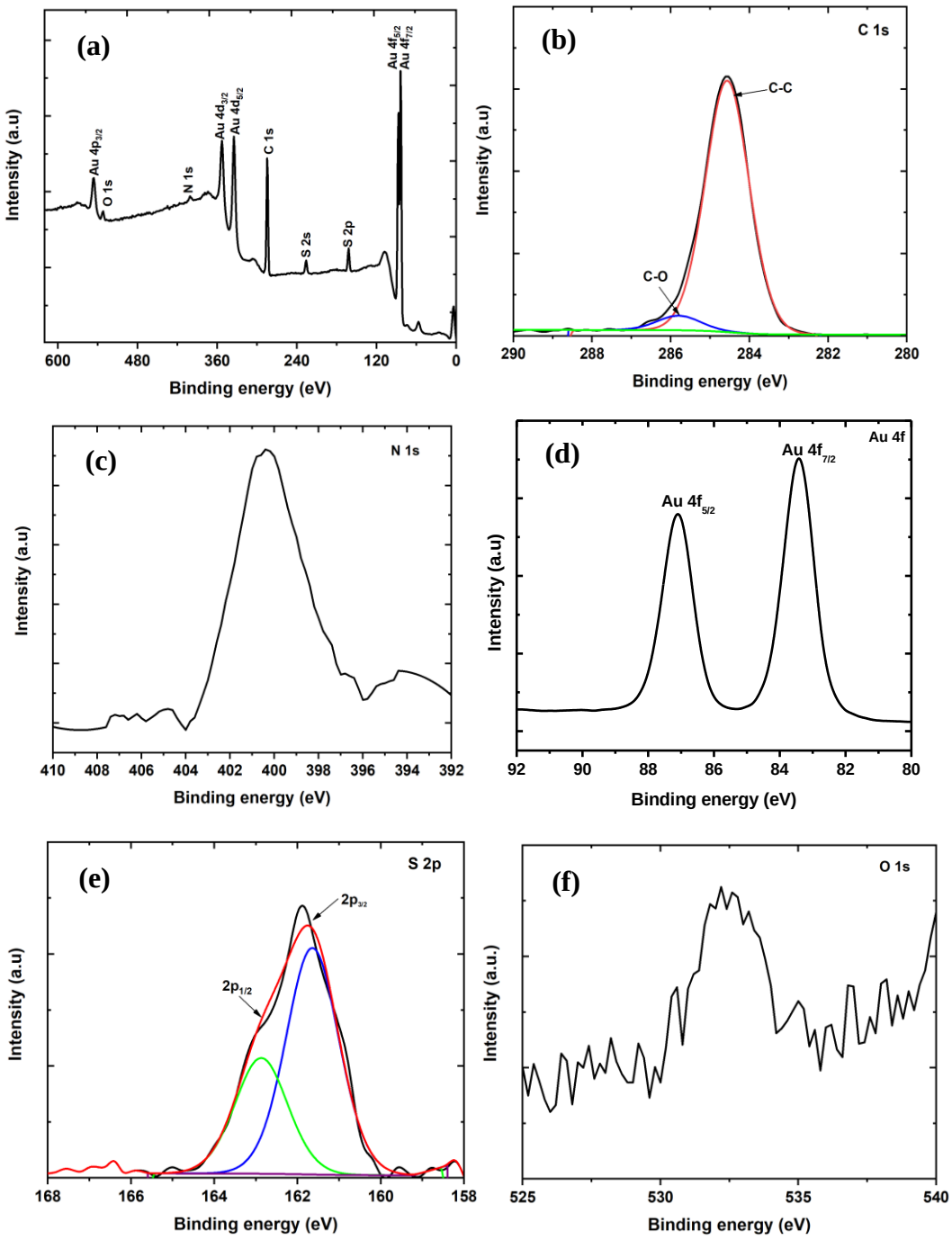

Fig. 4.4: (a) XPS survey spectrum, (b) C 1s, (c) N 1s, (d) Au 4f, (e) S 2p and (f) O 1s high-resolution spectra of capped of Au_2S nanostructures.

To further investigate the surface composition of the ligands that are attached to the surface of nanoparticles, FT-IR and NMR spectroscopy were used. The FT-IR spectra of pure samples of the capping agents (OLA and OA) and the as-synthesized Au_2S nanoparticles are shown in **Fig. 4.5**

and the results are summarized in **Table 4.4**. The two capping agents have similar C=C and CH_2/CH_3 functional groups. However, the characteristic functional groups that distinguish the two capping agents are the C=O and the NH_2 for the OA and OLA respectively. The characteristic peak associated with the C=O stretching vibration in pure OA was found at 1710 cm^{-1}, while the characteristic N-H band of OLA was positioned at 1620 cm^{-1}. The absence of the C-O or C=O bands in the Au_2S spectrum, suggests that the OA was not capped to the Au_2S surface as shown by the FT-IR spectra in **Fig. 4.5**. However, the OLA's N-H band showed a weak signal in the Au_2S spectra, indicating that OLA was successfully capped to the surface of the nanostructures through the amine group. The stronger nucleophilicity of the OLA than that of the acid may explain why it bonds to the nanostructures preferentially.

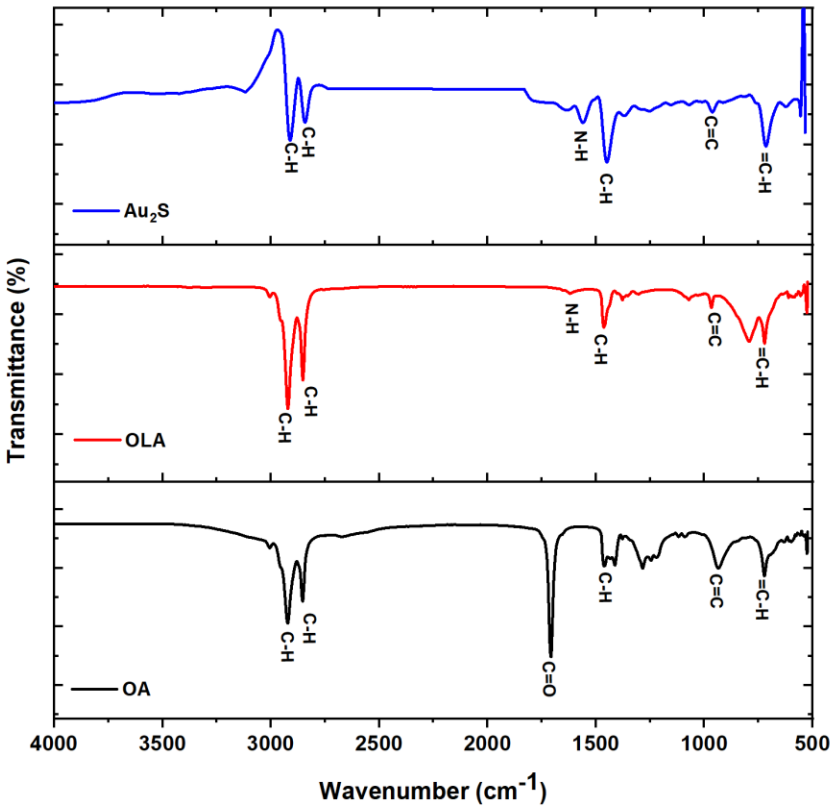

Fig. 4.5: FT-IR spectra of OA, OLA and Au_2S capped nanostructures.

Table 4.4: FT-IR assignments for oleic acid, oleylamine and Au_2S nanostructures

Assignment	OA (cm^{-1})	OLA (cm^{-1})	Au_2S (cm^{-1})
=C-H	719	719	719
C=C	931	968	970
C-H	1466 2850, 2925	1468, 2850, 2922	1450, 2837, 2921
C-O	1282	-	-
C=O	1710	-	-
N-H	-	1613	1576

NMR spectroscopy was done to further elucidate on the capping of the nanostructures and the ^1H spectra are shown in **Fig. 4.6** and the results are summarized in **Table 4.5**. The ^{13}C NMR spectrum is shown in **Fig. S4**. From the ^1H and ^{13}C NMR spectra of pure OLA and OA, all the protons and carbons were accounted for. The characteristic peaks for OLA were the $-NH_2$ (1.18 ppm) and the $-CH_2-NH_2$ (2.65 - 2.67 ppm) in the ^1H NMR spectrum and the $-CH_2-NH_2$ (42.26 ppm) in the ^{13}C NMR spectrum. On the other hand, the characteristic peaks for the OA were the $-CH_2-C=O$ (2.32 - 2.36 ppm) in the ^1H NMR spectrum and the C=O (180.70 ppm) in the ^{13}C NMR spectrum. The ^1H NMR spectrum of Au_2S showed the $-CH_2-NH_2$ (2.01 ppm) peak, suggesting that only the OLA is capped on the nanostructures surface. From the NMR spectra, only the N-H bands are visible which is consistent with the FTIR data. In general, both OA and OLA are assumed to be bonded to the surface of the nanostructures as independent entities, but a condensation reaction between the carboxylic acid (OA) and the amine (OLA) can, however, occur [31]. The reaction can result in a carboxylate salt as an intermediate before the formation of an amide as shown in **Scheme 4.2**. This could be the reason why it seems as though only the OLA is capping on the surfaces of the nanostructures. Further to that, this shows to confirm that the O detected in the XPS came from the OLA's surface oxidation [29].

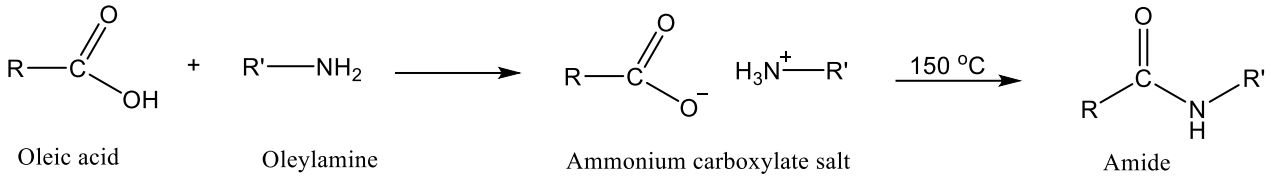

Scheme 4.2: Amide bond formation from the OLA and OA.

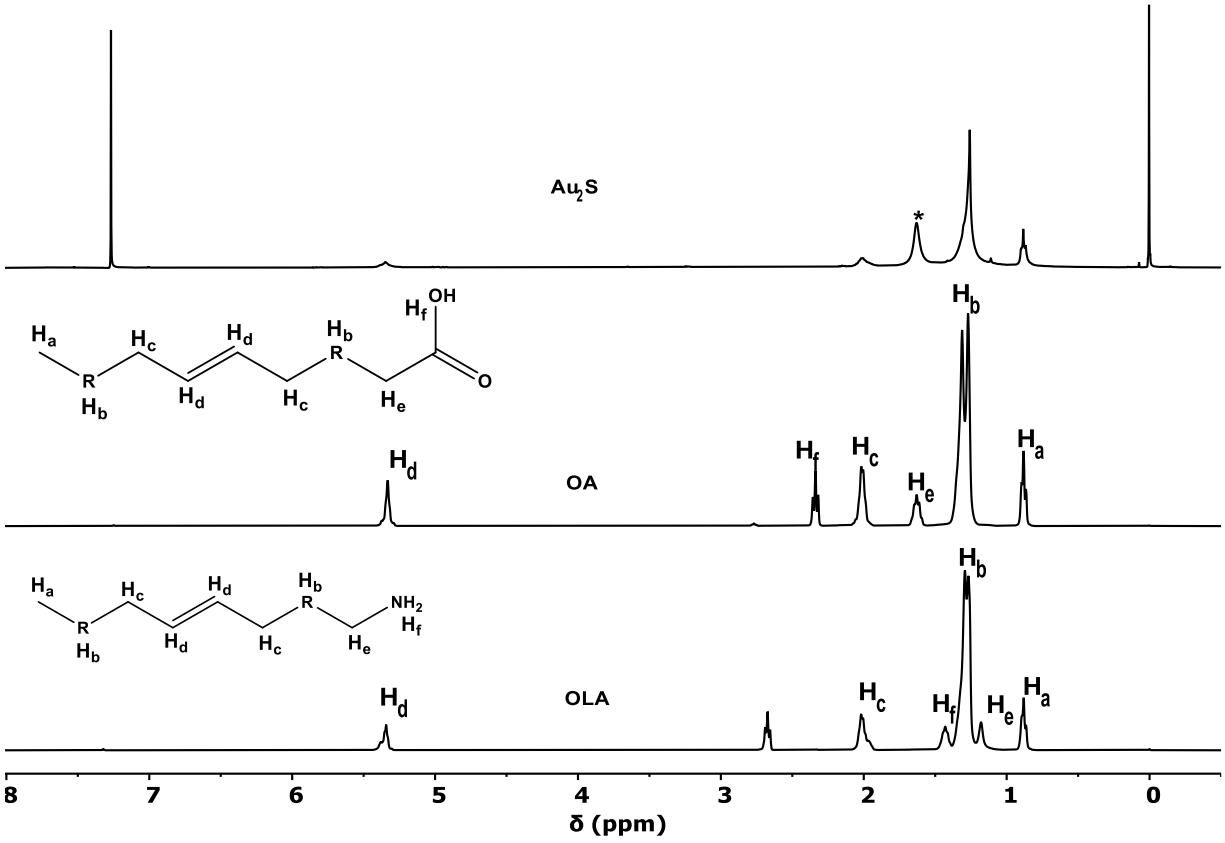

Fig. 4.6: ^{1}H NMR spectra of OA, OLA and Au_2S nanostructures, R=CH_2CH_2.

Table 4.5: NMR assignments for oleic acid, oleylamine and Au_2S nanostructures

Sample	Type of H	Free Chemical shift (δ)	Capping Chemical shift (δ)
OLA	$-CH_3$	0.86-0.88	0.88-0.90
	$-CH_2-$	1.27-1.29	1.26-1.30
	R-CH=CH-R	1.95-2.02	2.00-2.01
	$-NH_2$	1.43-1.46	1.62-1.63
	$R-NH_2$	2.65-2.67	-
	CH=CH	5.30-5.34	5.35-5.37
	R_1-NH_2	1.33-1.37	-
OA	$-CH_3$	0.87-0.89	0.88-0.90
	$-CH_2-$	1.27-1.31	1.26-1.30
	$R_1-C=O$	1.59-1.62	-
	R-CH=CH-R	1.98-2.08	2.00-2.01
	R-C=O	2.32-2.36	-
	CH=CH	5.31-5.36	5.35-5.37

✓ *$R = CH_2$ and $R_1 = CH_2-CH_2$* , [ref]

UV-vis and PL spectroscopy were used to determine the optical characteristics of the Au_2S nanostructures, and the UV-vis spectra are given in **Fig. S5**. From the UV-vis spectra, the Tauc plot was obtained **Fig 4.7(a)** and used to determine the bandgap of the Au_2S nanostructures which was found to be 2.66 eV. The optical properties of the Au_2S nanostructures were compared to Cu_2S and Ag_2S nanoparticles. The work done by Saraf and Saranya et al. [32, 33] found the band gaps of Cu_2S and CuS to be 2.66 eV and 1.65 eV respectively which is comparable to the Au_2S. The band gap of Ag_2S on the other hand is lower as compared to both the Cu_2S and Au_2S. Zamiri et al and Sankapal et al. [34, 35] reported a bandgap of 0.96 eV and 1.1 eV for the Ag_2S nanoparticles respectively. An ideal solar cell has a direct band gap of 1.4 eV to absorb the maximum number of photons from the sun's radiation. However, Jarosz et al. [36], did a study on the effect of bandgap on power conversion efficiency and their results showed that the higher the bandgap, the better chance of better power conversion efficiency. The power conversion efficiency of a material with a band gap of 1.8 eV (optimal bandgap) is two times higher than at 1.1 eV, and this explains why crystalline silicon with its band gap equal 1.12 eV is not an adequate material for

indoor photovoltaics [36]. With the higher bandgap of the Au_2S, the power conversion efficiency could be affected however the results obtained should be able to give more insight on the materials properties. The emission spectrum of the Au_2S nanostructures, **Fig. 4.7(b)** showed a bathochromic shift in the emission wavelength to 2.49 eV.

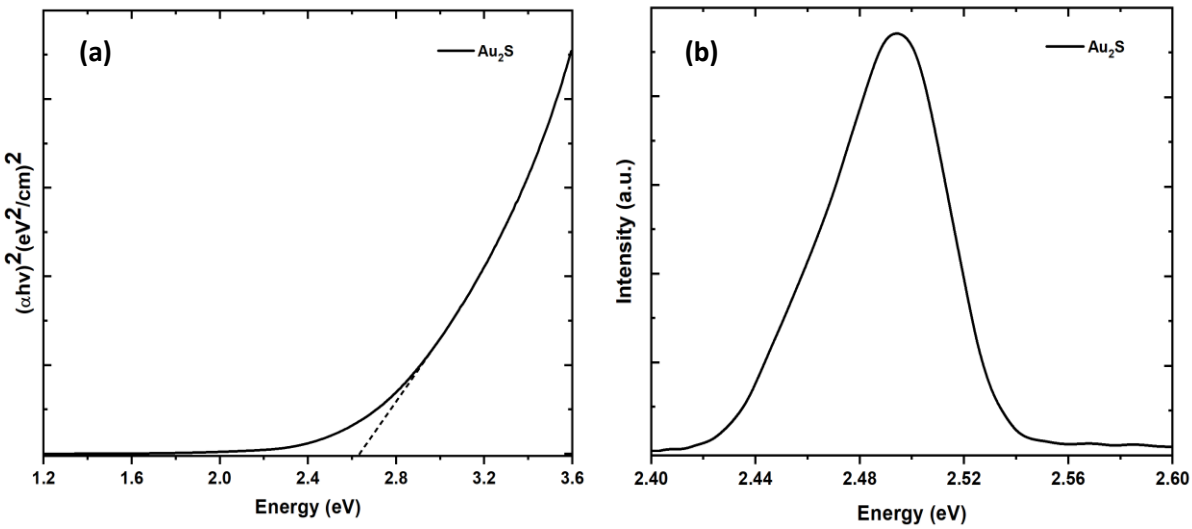

Fig. 4.7: (a) Tauc plot and (b) photoluminescence spectra of Au_2S nanostructures.

4.2.3 Effect of the nature of the single-source precursor on the synthesis of Au_2S nanostructures

The XRD pattern of the synthesized Au_2S nanostructures synthesized using the different single-source precursor with the respective reference peaks are shown in **Fig. 4.8**. The XRD patterns showed the respective peaks at 2θ values of 30.82°, 35.74° and 51.44° which were assigned to the diffraction planes (111), (200) and (220), respectively. The Au_2S nanostructures were indexed to a pure Au_2S (PDF: 01-085-1997) with cubic crystal phase and space group Pn-3m (224). From the XRD pattern, there was no observable difference in the synthesized Au_2S nanostructures from the different gold dithiocarbamate single-source precursors.

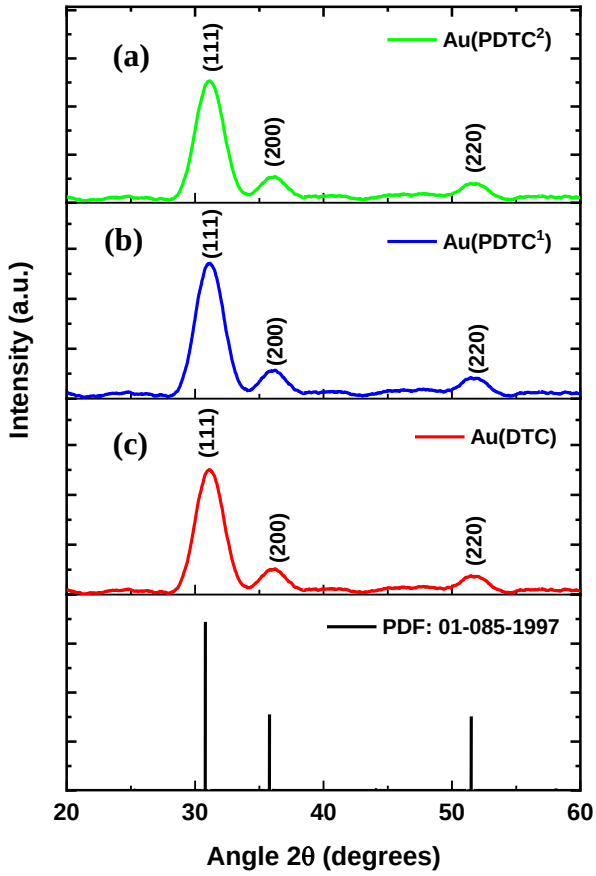

Fig. 4.8: X-ray diffractogram patterns of the Au_2S nanostructures synthesized using (a) gold (ammonium) pyrrolidine dithiocarbamate complex (b) gold (sodium) pyrrolidine dithiocarbamate complex and (c) gold diethyldithiocarbamate complex.

To study the morphological properties of the Au_2S nanostructures, TEM studies were done. Shown in **Fig. 4.9** are TEM images of the nanostructures synthesized using the different single-source precursor complex with their corresponding distribution curves. All samples showed a quasi-spherical morphology, and the average size of the nanostructures was between 2.9 and 3.1 nm. From the XRD and TEM analysis, the change in the different precursors did not have an influence on the synthesized Au_2S nanostructures. Jagodish et al. [37] reported that variations in the length-nature of the alkyl group of the dithiocarbamte ligands do not have a substantial impact on the chemical characteristics of the complexes formed, they do have a considerable impact on the physical properties, particularly melting temperatures, solubility, and volatility. This explains why

we did not observe any difference in the synthesized nanostructures, despite the change in the dialkyl ligands. From the above obtained results and the percent yield of the synthesized complexes only the gold diethyldithiocarbamate complex was used for further studies on the different reaction parameters.

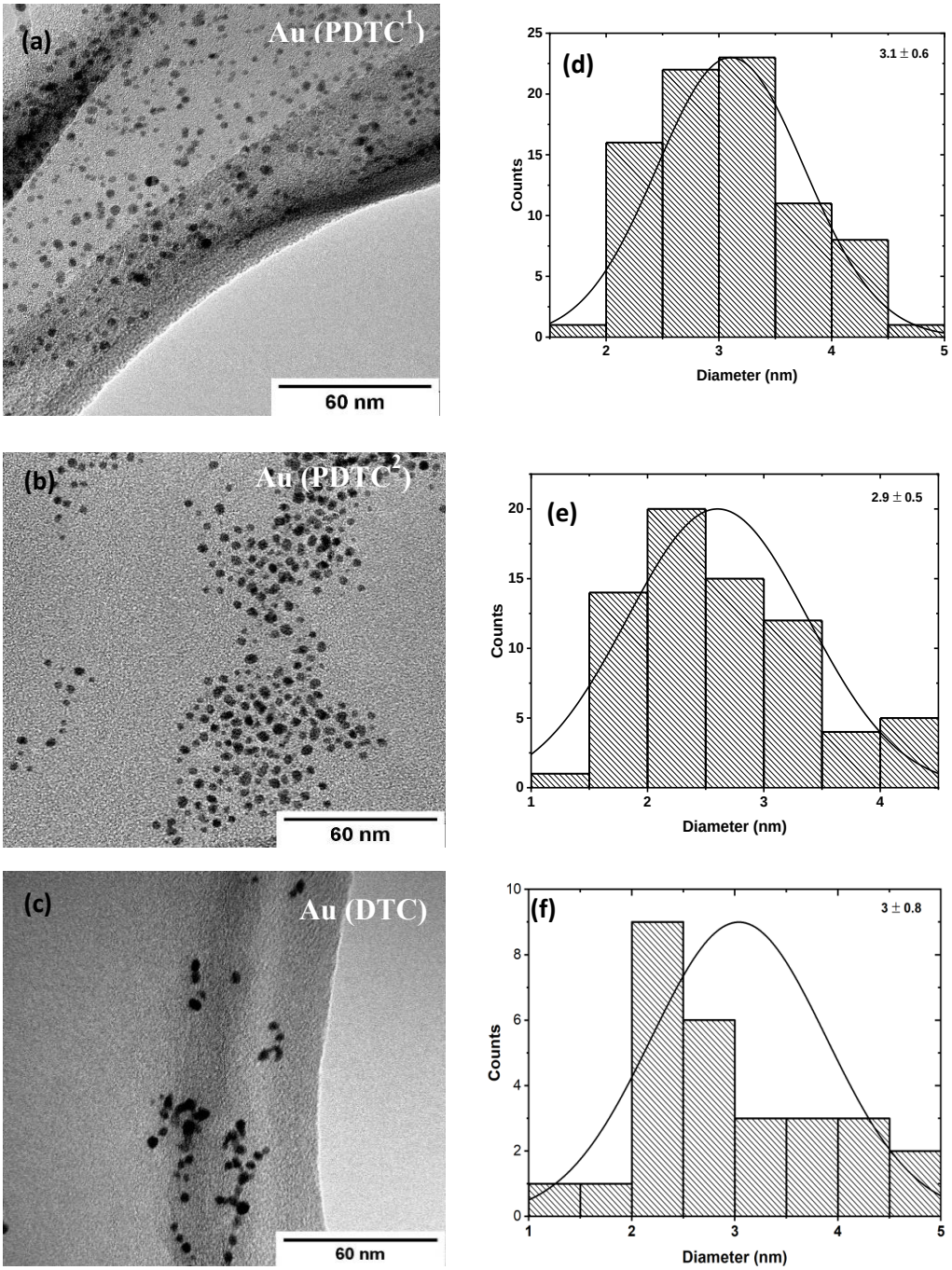

Fig. 4.9: (a-c) TEM images (d-f) corresponding size distribution of the Au_2S nanostructures synthesized using different single-source precursors.

4.2.4 Effect of temperature

Temperature is one of the most important elements that influences the size, shape, and phase of nanoparticles. The size of nanoparticles is greatly influenced by the temperature reaction, since higher temperatures favor larger particle sizes. Temperature influences the form of nanoparticles due to a conflict between the kinetic and thermodynamic regimes as explained in chapter 2, section 2.2.2.3.3.4 [25, 26]. The effect of temperature on the reaction was investigated by changing the temperature of the reaction, (140, 170 and 200 ℃). The temperature range was chosen based on the TGA decomposition curves of the precursor complex, which shows that the gold complex decomposes within the range 200 – 250 ℃. The XRD pattern of the synthesized Au_2S nanostructures synthesized at the different temperatures with the respective reference peaks are shown in **Fig. 4.10**. At 140 ℃, the synthesized nanostructures do match the Au_2S (PDF: 01-085-1997), with broad peaks as compared to the other synthesized nanostructures. However, the peak at standard Bragg reflection 220 shows a relatively low intensity, hence the temperature could not be considered ideal for the synthesis of the Au_2S nanostructures. At a higher temperature (200 ℃), gold impurities indexed to card number (PDF: 01-077-9662) were observed in the XRD pattern of the synthesized Au_2S nanostructures. The peaks that are from elemental gold have been marked with an asterisk (*) for easy identification. The presence of the elemental gold at higher temperatures is an indication that the sulfur from the Au_2S is becoming oxidized to SO_2. The temperature of 170 ℃ was then chosen as the optimal temperature as the synthesized Au_2S matched the reference card (PDF: 01-085-1997), with more distinct clear peaks without any gold impurities. The particle size of the samples prepared at 140 ℃, 170 ℃ and 200 ℃ was calculated based on Scherrer's equation, and the mean sizes of the particles prepared was 1.48, 3.82 and 3.94 nm respectively.

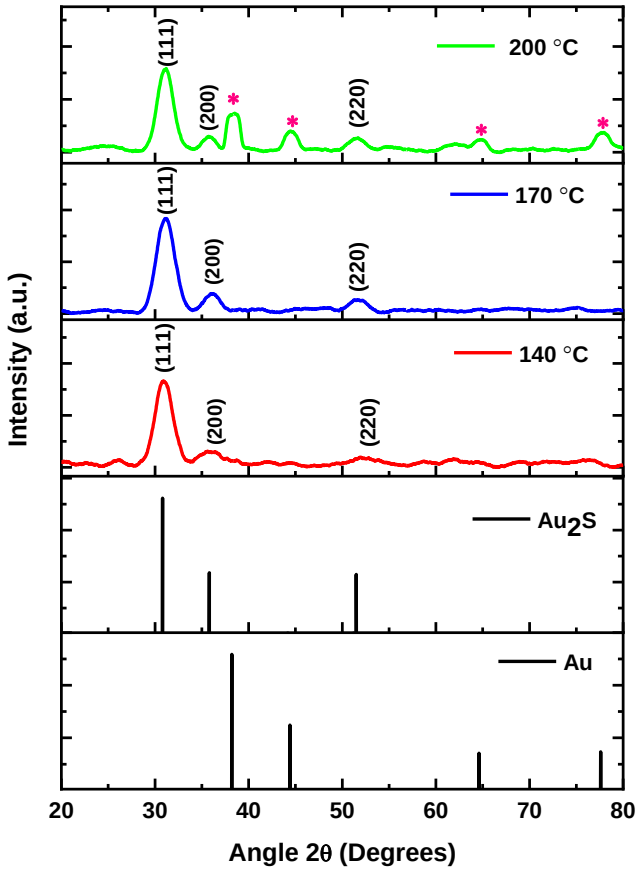

Fig. 4.10: XRD patterns of Au_2S nanostructures synthesized at different temperatures.

TEM was used to investigate the size and morphology of the nanostructures synthesized at various temperatures and the results are shown in **Fig. 4.11(a-c)**. The results show that the synthesized Au_2S nanostructures at 140 and 170 ℃ are all quasi-spherical in shape, polydispersed and highly agglomerated. The TEM image of the synthesized nanostructures at 200 ℃ **(Fig. 4.11c)** show a mixed morphology of nanospheres and nanorods. The nanorods (marked with *) are due to the presence of the elemental gold observed from the XRD data. As the temperature was increased from 140 ℃ to 170 ℃, the synthesized nanostructures were also increasing in size. These results are consistent with the results obtained from the XRD nanoparticle size calculations using the Scherrer equation. The difference in growth of the synthesized nanostructures across the temperature range could potentially be due to differences in surface ligand dynamics. At low temperatures, (i.e., 140 ℃), ligands are more likely to remain on the surface of the nanostructures,

thus having a significant impact on the nanostructures' growth. On the other hand, at higher temperatures, there is thermal agitation of the surface ligands which limits their influence on the nanostructure's growth behavior [38].

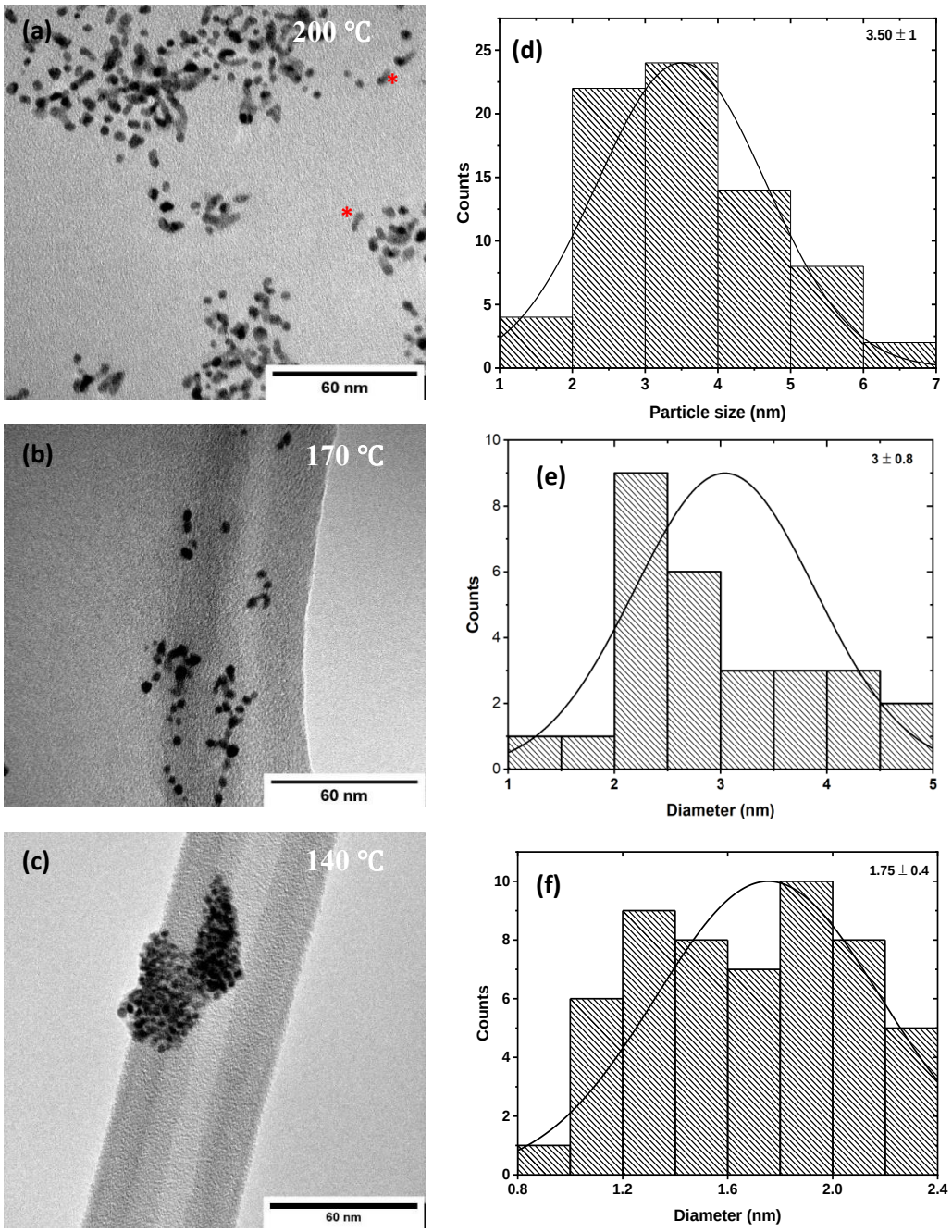

Fig. 4.11: (a-c) TEM images and (d-f) corresponding distribution curves for the Au_2S nanostructures synthesized at different temperatures.

UV-vis and PL spectroscopy were used to determine the optical characteristics of the Au_2S nanostructures synthesized at various temperatures. The UV-vis absorption spectra are shown in **Fig. S5**. Shown in **Fig. 4.12(a)** is the Tauc plot that was used to determine the bandgap energy of the nanostructures. As the temperature was increasing from 140, 170 to 200 ℃, a decrease in band-gap energy was observed from the Tauc plots to be 2.92 eV, 2.66 eV, and 2.24 eV respectively. This was a result of an increase in particle size due to Ostwald ripening effects caused by rising temperatures [39]. **Fig. 4.12(b)** shows the emission spectra of the Au_2S nanostructures synthesized at various temperatures. There was a red shift (bathochromic shift) in the emission wavelength of the Au_2S with an increase in temperature of the nanostructures. The emission spectra of the Au_2S nanostructures synthesized at 140 ℃, 170 ℃, 200 ℃, was 2.52 eV, 2.49 eV and 2.44 eV respectively. The emission spectrum of the nanostructures synthesized at 200 ℃ show a broader peak as compared to the others which is a sign of the polydispersity nature of the nanostructures as confirmed by the TEM image in **Fig. 4.11(a)**.

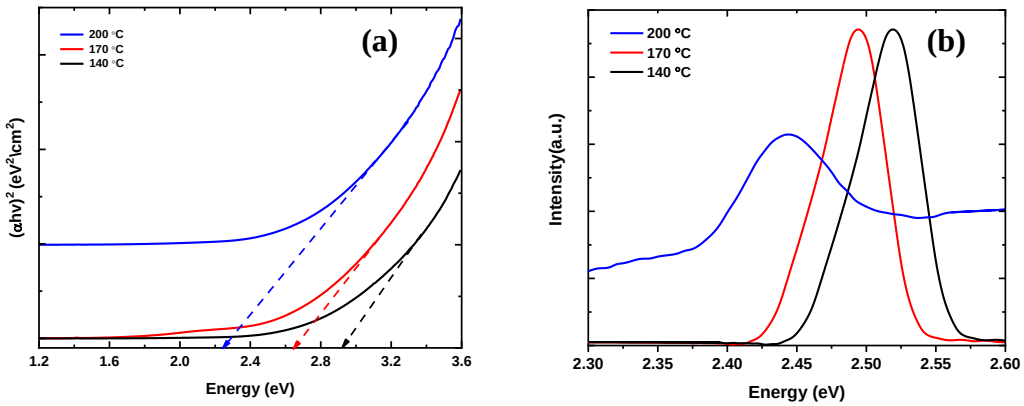

Fig. 4.12: (a) Tauc plots and (b) photoluminescence spectra of Au_2S nanostructures synthesized at different temperatures.

4.2.5 Effect of time

The influence of reaction time on the synthesis of the Au_2S nanostructures was explored at 30, 45 and 60 min while keeping all the other synthesis parameters like temperature and concentration constant. According to several reports by other researchers, longer reaction times (higher nucleation times) yield larger nanoparticles, and this is because of the Ostwald ripening process [24, 40]. The XRD data of all three samples with varying nucleation times are shown in **Fig. 4.13**.

The samples have similar XRD pattern, and they are indexed to pure Au_2S (PDF: 01-085-1997) with cubic crystal phase and space group Pn-3m (224). Using Debye-Scherrer's equation, the average particle sizes were estimated to be 3.47 nm, 3.82 nm, and 3.93 nm for the nanostructures synthesized at 30 minutes, 45 minutes, and 60 minutes respectively.

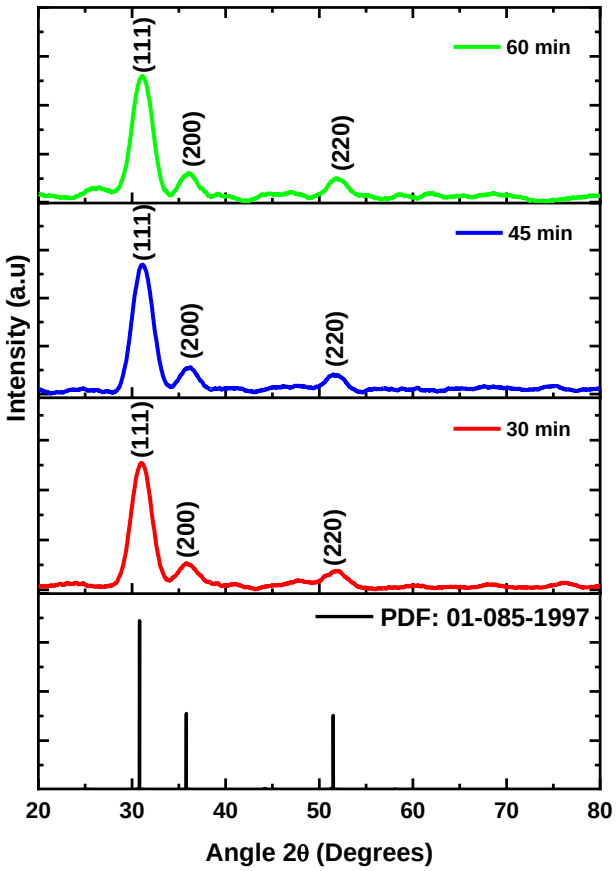

Fig. 4.13: XRD patterns of Au_2S nanostructures synthesized at different reaction times.

The morphology of the synthesized nanostructures at different times was investigated using TEM and the micrographs are presented in **Fig. 4.14(a-c)**. The synthesized Au_2S nanostructures at the different times (30, 45, and 60 min) are all quasi-spherical in shape, polydispersed and agglomerated. The TEM image of the nanostructures synthesized at 30 min, **Fig. 4.14(c)**, shows agglomerates of smaller quashi-spherical nanostructures as compared to those synthesized at 45 and 60 min. The size distribution curves from the TEM images show an average size of 2.0 nm, 3.0 nm and 3.73 nm for the nanostructures synthesized at 30, 45, and 60 min respectively. The

increase in nanostructure size with increase in reaction time is consistent with the results obtained from the XRD data using the Debye-Scherer's equation. This is expected because longer reaction periods allow for more monomer addition to existing nuclei, facilitating growth through the Ostwald repining process [41].

Fig. S5 shows the absorption spectra of the Au_2S nanostructures synthesized at various reaction times. The Tauc plots **Fig. 4.15(a)** show that as the time increased from 30, 45 and 60 min, the band-gap energy decreased accordingly, 3.14 eV, 2.66 eV, and 2.48 eV, respectively due to quantum confinement effects. The photoluminescence spectra of the nanostructures synthesized at different times is shown in **Fig. 4.15(b)**. There is a consistent red-shift from the corresponding absorption band gap that can be observed in their emission spectra. The emission bandgap energies of the nanostructures synthesized at 30, 45 and 60 min were 2.53 eV, 2.49 eV and 2.42 eV respectively. This is expected, given that longer reaction time results in the formation of bigger particles.

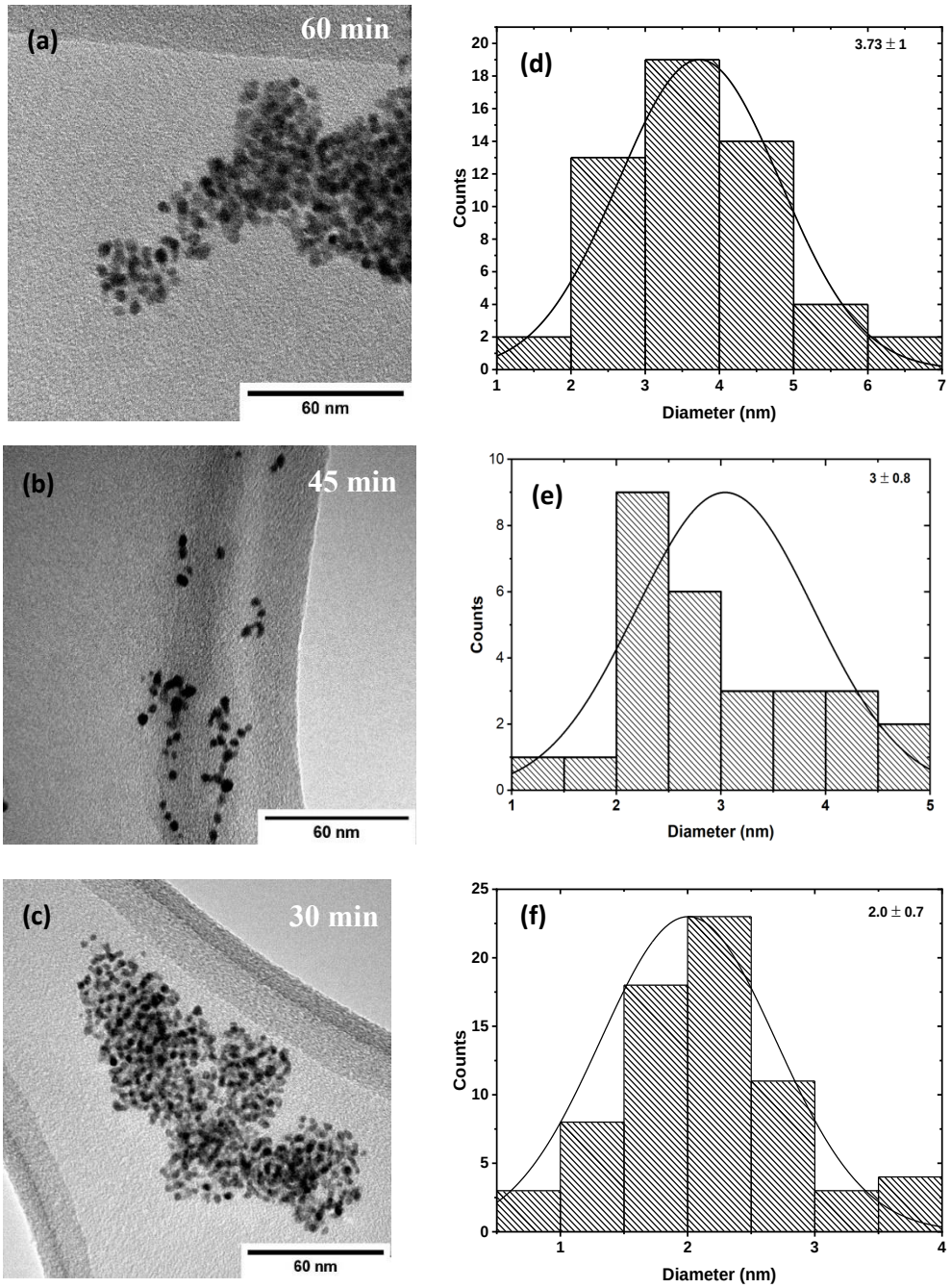

Fig. 4.14: (a-c) TEM images and (d-f) size distribution of Au_2S nanostructures synthesized at different reaction times.

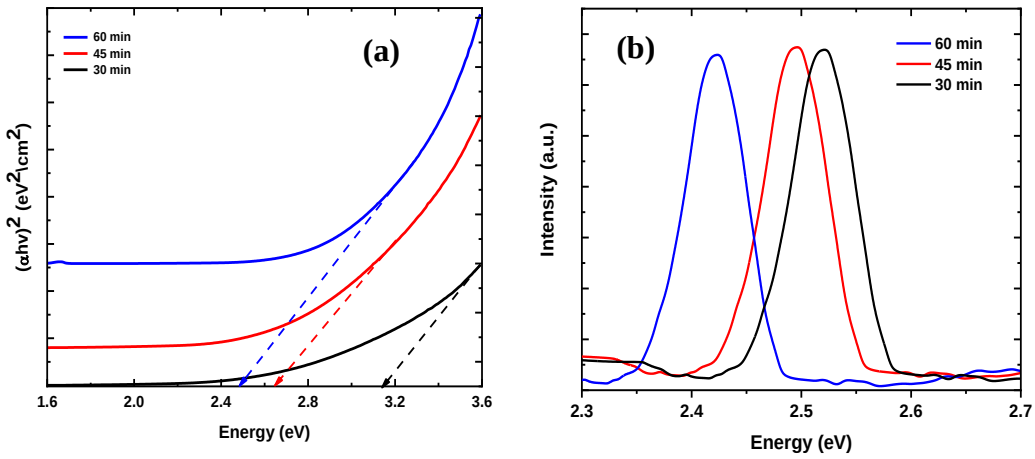

Fig. 4.15: (a) Tauc plots and (b) photoluminescence spectra of Au_2S nanostructures synthesized at different reaction times.

4.2.6 Effect of concentration

According to a few reports, the size and shape of nanoparticles are influenced significantly by the precursor concentration. Higher concentrations favor larger nanoparticles and lower concentrations favor smaller nanoparticles [44, 43]. It has been reported that the reaction route for the synthesis of nanoparticles is influenced by the precursor concentration; the reaction can proceed either under a thermodynamic or kinetic growth control regime. The thermodynamic growth phase is characterized by a steady supply of heat energy and a low monomer concentration, resulting in isotropic shaped nanocrystals, which are the most stable form of nanocrystals (e.g., cubes, spheres). In non-equilibrium, kinetic conditions, on the other hand, with a relatively high monomer concentration, selective anisotropic growth (e.g. rod-like structures) is made easier [26]. **Fig. 4.16** shows the XRD patterns of Au_2S nanostructures synthesized using varying amounts of precursor concentration, 1.918 M, 3.837 M and 7.674 M. The XRD patterns of the samples are comparable for all precursor concentrations, indicating that the complex's concentration had no effect on the stoichiometry and phase of the synthesized nanostructures. The synthesized nanostructures were indexed to pure phase Au_2S (PDF: 01-085-1997) with a cubic crystal phase. The mean particle sizes estimated by the Debye Scherrer equation for the precursor concentrations of 7.674, 3.837 and 1.918 M were 3.96 nm, 3.82 nm, and 3.36 nm, respectively.

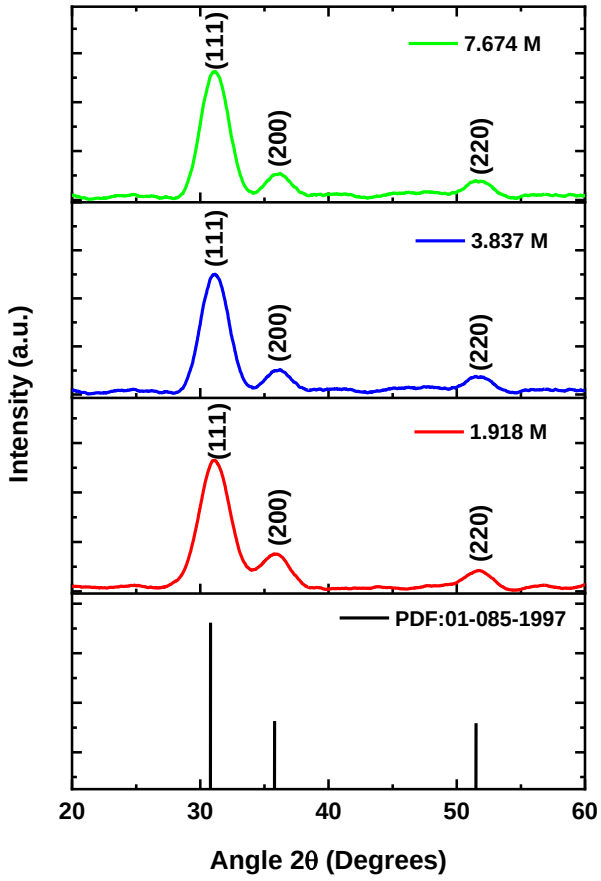

Fig. 4.16: XRD patterns of Au_2S nanostructures synthesized using different precursor concentrations.

TEM images of the Au_2S nanostructures synthesized with varying complex precursor concentrations are shown in **Fig. 4.17(a-c)**. The synthesized nanostructures are all quasi-spherical in shape and the sizes decreased as the precursor concentration decreased. The results obtained however do not agree with the theory that the reaction can proceed either under a thermodynamic or kinetic growth control regime, thus influencing the structure of the nanostructures. For the complex precursor concentration of 7.674, 3.837 and 1.918 M the average size from the histogram distribution curves was 3.34 nm, 3.00 nm, and 2.91 nm respectively.

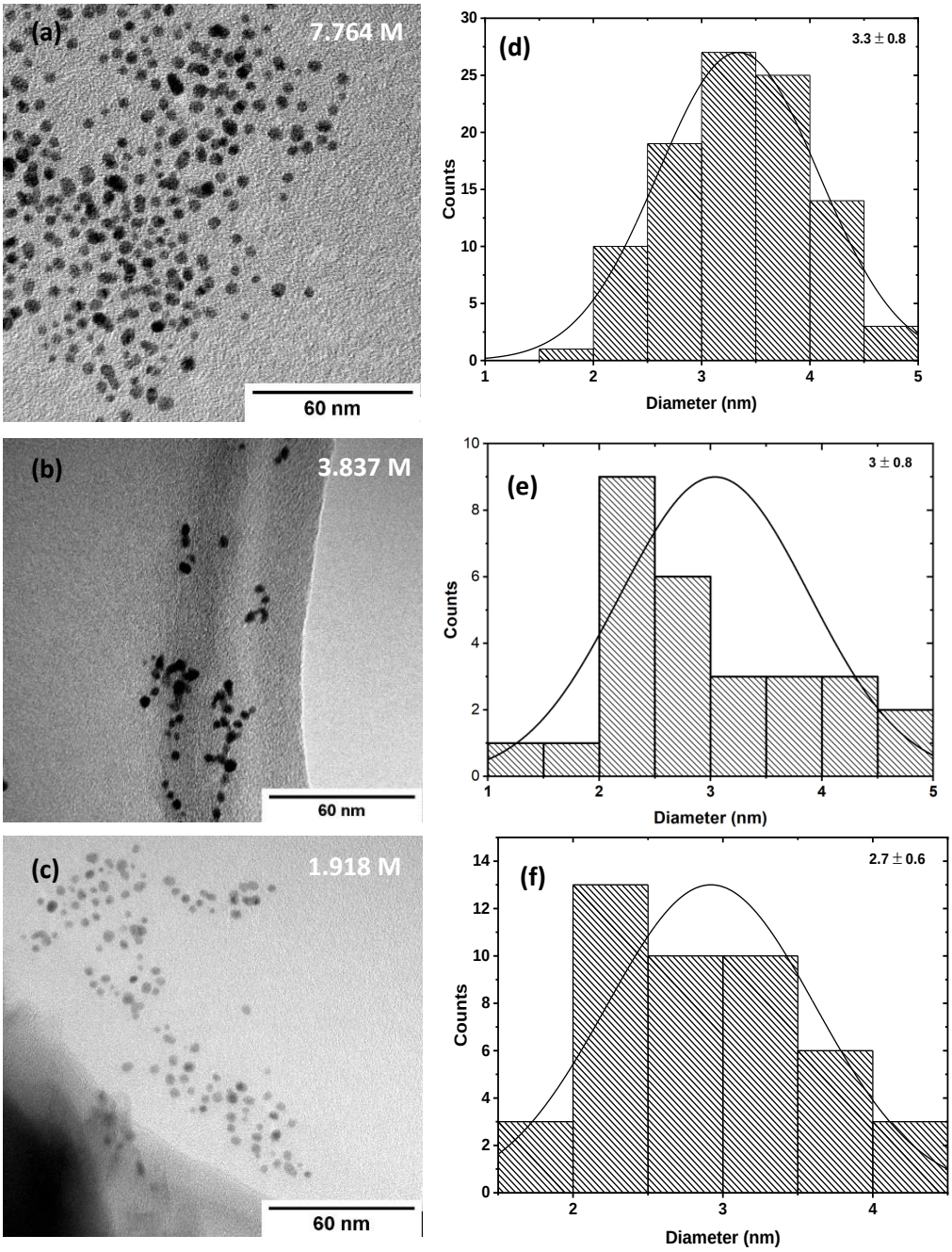

Fig. 4.17: (a-c) TEM images and (d-f) size distribution of Au_2S nanostructures synthesized using different precursor concentrations.

The optical properties of Au_2S nanostructures synthesized using different precursor concentrations were studied using UV-vis absorption and photoluminescence spectroscopy and the UV-vis spectra are shown in **Fig. S5**. From the Tauc plots (**Fig. 4.18)** a decrease in bandgap energy was

observed as the precursor concentration was increased, this can be explained in conjunction of the results obtained from XRD and TEM. As the concentration was increased from 1.918, 3.837 to 7.674 M, there was an increase in the size of the synthesized nanostructures, hence a decrease in the bandgap energy. The bandgap values for the precursor concentrations of 1.918, 3.837 to 7.674 M were 2.77 eV, 2.66 eV and 2.41 eV respectively. The photoluminescence spectra of the nanostructures synthesized with precursor concentrations of 1.918 and 3.837 M were red-shifted from the UV-vis absorption spectrum to 2.50 eV and 2.49 eV respectively. On the other hand, the photoluminescence spectra of the nanostructures synthesized with precursor concentration of 7.674 M, shows a blue-shift from the UV-vis absorption spectrum to 2.47 eV, due to possible nanostructure defects, which deviates from the ideal quantum and electronic confinement effect. The quantum confinement effect ideally states that for a semiconductor crystal, as the size of a particle decreases, the decrease in confining dimension makes the energy levels discrete which increases the band gap, and thus the band gap energy [44].

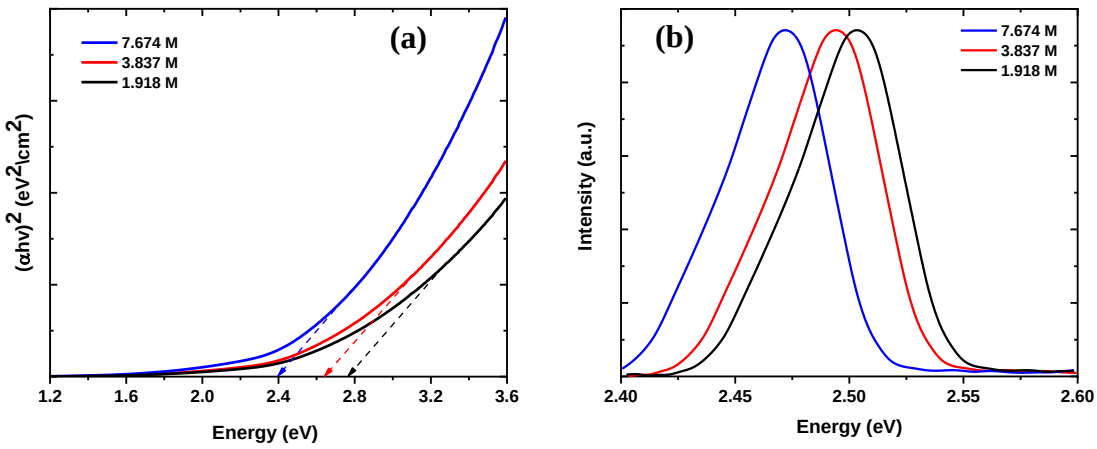

Fig. 4.18: (a) Tauc plots and (b) photoluminescence spectra of Au_2S nanostructures synthesized using different precursor concentrations.

4.3 Conclusion

Au_2S nanostructures with diameters of ~3 nm were successfully synthesized from a single-source precursor via the colloidal synthesis method. Their identity has been confirmed with XRD, TEM, EDS, and Raman characterization techniques. XPS, FT-IR, and NMR spectroscopic techniques were used to investigate the surface chemistry of the nanostructures and the sole ligand capping

the nanostructures was proven to be OLA. The optical absorption characteristics of the Au_2S as a direct bandgap semiconductor was ~ 2.66 eV, which should enable the material find application in photovoltaic devices, especially the dye-sensitized solar cells (DSSCs) as a potential counter electrode. The effect of time, temperature, precursor concentration and precursor source on the synthesis of Au_2S nanostructures from gold dithiocarbamate single-source precursors was investigated. An increase in temperature and time resulted in an increase in the nanostructures size due to Ostwald ripening. The temperature on the other hand, has shown to also affect the morphology of the nanostructures as rod-like nanostructures were observed at higher temperatures. The size of nanostructures was affected by precursor concentration, with the size decreasing as the precursor concentration was reduced. And the change in the different gold dithiocarbamate precursors did not affect the synthesized nanostructures. It can thus be concluded that varying reaction parameters, time, temperature and precursor concentration has a profound effect on the properties of the synthesized nanostructures.

4.4 References

[1] C.H. Lai, M.Y. Lu, L.J. Chen, *Journal of Materials Chemistry*, 22 (2012) 19–30.

[2] F.L. Pua, C.H. Chia, S. Zakari, T.K. Liew, M.A. Yarmo, N.M. Huang, Sains Malaysiana, 39 (2010) 243–248.

[3] Y. Xiao, S.H. Lee, Y. Sun, *Advance Energy Materials*, 20 (2016) 1601329.

[4] A. Balakrishnan, J.D. Groeneveld, S. Pokhrel, L. Mädler, *European Journal of Chemistry*, 27 (2021) 6390–6406.

[5] K. Ishikawa, T. Isonaga, S. Wakita, Y. Suzuki, *Solid State Ionics*, 79 (1995) 60–66.

[6] T. Tani, Oxford University Press: Oxford, U.K. (1995)

[7] A.A. Bagatur'yants, A. Safonov, H. Stoll, H.J. Werner, *Journal of Chemical Physics*, 109 (1998) 3096–3107.

[8] A. Ulman, *Chemical Reviews*, 96 (1996) 1533–1554.

[9] M.R. Gao, Y.F. Xu, J. Jiang, S.H. Yu, *Chemical Society Reviews*, 42 (2013) 2986–3017.

[10] N. Boadi, A. Malik, P. O'Brien, J. Awudza, *Journal of Chemical Society, Dalton Transactions*, 41 (2012) 10497–10506.

[11] P. Marchand, S. Sathasivam, B.A.D. Williamson, D. Pugh, S.M. Bawaked, S.N. Basahel, A.Y. Obaid, D.O. Scanlon, I.P. Parkin, C.J. Carmalt, *Journal of Materials Chemistry C*, 4

(2016) 6761–6768.

[12] D. Paliwoda, P. Wawrzyniak, A. Katrusiak, *Journal of Physical Chemistry Letters*, 5 (2014) 2182–2188.

[13] A.A. Sulaiman, A. Muhammad, A. Anvarhusein, A. Isab, A. Alawad, S. Altuwaijri, S. Ahmad, *Journal of inorganic and general chemistry*, 00 (2016) 00278.

[14] S. Khalid, E. Ahmed, M.A. Malik, D.J. Lewis, S.A. Bakar, Y. Khan, P.O. Brien, *New Journal of Chemistry*, 12 (2014) 101039.

[15] X. Chen, Z. Wang, J. Wan, J. Lui, Y. Qian, *Chemistry Letters*, 33 (2004) 1294–1314.

[16] S. Shen, Y. Zhang, L. Peng, B. Xu, Y. Du, M. Deng, H. Xu, Q. Wang, *CrystEngComm*, 13 (2011) 4572–4579.

[17] G. Barone, T. Chaplin, T.G. Hibbert, A.T. Kana, M.F. Mahon, K.C. Molloy, I.D. Worsley, P. Parkin, L.S. Price, *Dalton Transactions*, 20 (2002) 1085–1092.

[18] J. Van Embden, A.S.R. Chesman, J.J. Jasieniak, *Chemistry of Materials*, 27 (2015) 2246–2285.

[19] C.B. Whitehead, S. Özkar, R.G. Finke, *Materials Advances*, 2 (2021) 186–235.

[20] T. Kolokoto, V. Mashindi, L.E.F. Machogo-phao, Z.B. Ndala, N.P. Shumbula, S.S. Nkabinde, G.N. Ngubeni, S.S. Gqoba, K.P. Mubiayi, N. Moloto, *RSC Advances*, 11 (2021) 31159–31173.

[21] P.S. Nair, T. Radhakrishnan, N. Revaprasadu, P.O. Brien, P.O., Nair, *Materials Science and Technology*, 21(2005) 237–242.

[22] M.S. Ghamsari, H. Mehranpour, M. Askari, *Nanochemistry Research*, 2 (2017) 132–139.

[23] O. Akinbami, G.N. Ngubeni, F. Otieno, R. Kadzutu-sithole, E.C. Linganiso, Z.N. Tetana, S.S. Gqoba, K.P. Muiayi, N. Moloto, *Journal of Materials Chemistry C*, 9 (2021) 6022–6033.

[24] U. Manzoor, F. Tuz Zahra, S. Rafique, M.T. Moin, M. Mujahid, *Journal of Nanomaterials*, 2015, (2015) 189058.

[25] S.B. Sibokoza, M.J. Moloto, N. Moloto, P.N. Sibiya, *Chalcogenide Letters*, 14 (2017) 69–78.

[26] N. Moloto, N. Revaprasadu, P.L. Musetha, M.J. Moloto, *Journal of Nanoscience and Nanotechnology*, 9 (2009) 4760–4766.

[27] Y. Mikhlin, M. Likhatski, A. Karacharov, V. Zaikovski, A. Krylov, *Physical Chemistry*

Chemical Physics, 11 (2009) 5445–5454.

[28] S. Burgess, X. Li, J. Houand, *Microscopy and Analaysis*, 27 (2013) S8–S13.

[29] R.K. Sithole, L.F.E. MacHogo, M.A. Airo, S.S. Gqoba, M.J. Moloto, P. Shumbula, J. Van Wyk, N. Moloto, *New Journal of Chemistry*, 42 (2018) 3042–3049.

[30] R.J. Parmar, V.R. Solanki, R.J. Pathak, M.D. Parmar, *AIP Conference Proceedings*, 1837 (2017) 535–539.

[31] G. Almeida, L. Goldoni, Q. Akkerman, Z. Dang, A.H. Khan, S. Marras, I. Moreels, L. Manna, *ACS Nano*, 12 (2018) 1704–1711.

[32] R. Saraf, *Journal of Electrical and Electronic Engineering*, 2 (2012) 47–51.

[33] M. Saranya, C. Santhosh, R. Ramachandran, A.N. Grace, *Journal of Nanotechnology*, 2014 (2014) 321571.

[34] R. Zamiri, H.A. Ahangar, A. Zakaria, G. Zamiri, M. Shabani, *Chemistry Central Journal*, 9 (2015) 4–9.

[35] B.R. Sankapal, R.S. Mane, C.D. Lokhande, *Materials Chemistry and Physics*, 63 (2000) 226–229.

[36] G. Jarosz, R. Marczyński, R. Signerski, *Materials Science in Semiconductor Processing*, 107 (2020) 104812.

[37] J.C. Sarker, G. Hogarth, *Chemistry Reviews*, 121 (2021) 6057–6123.

[38] N. Pradhan, D. Reifsnyder, R. Xie, J. Aldana, X. Peng, *Journal of American Chemical Society*, 129 (2007) 9500–9509.

[39] S.T. Gentry, S.F. Kendra, M.W. Bezpalko, *Journal of Physical Chemistry C*, 115 (2011) 12736–12741.

[40] Y. Mastai, R. Polsky, Y. Koltypin, A. Gedanken, G. Hodes, *Journal of American Chemical Society*, 121 (1999) 10047–10052.

[41] N. Moloto, M.J. Moloto, N.J. Coville, S. Sinha Ray, *Journal of Crystal Growth*, 324 (2011) 41–52.

[42] N. Miguel-Sancho, O. Bomati-Miguel, A.G. Roca, G. Martinez, M. Arruebo, J. Santamaria, *Industrial and Engineering Chemistry Research*, 51 (2012) 8348–8357.

[43] H. Sharifi Dehsari, A. Halda Ribeiro, B. Ersöz, W. Tremel, G. Jakob, K. Asadi, *CrystEngComm*, 19 (2017) 6694–6702.

[44] L.Z. Zhang, W. Sun, P. Cheng, *Molecules*, 8 (2003) 207–222.

CHAPTER 5

Investigating the electrocatalytic activity of Au_2S synthesized from a single-source precursor as counter electrode in dye-sensitized solar cells

5.1 Introduction

Scientists are looking for sustainable and environmentally friendly alternative sources of energy to replace finite fossil fuels due to rising global energy consumption, climate change, and environmental concerns [1]. Among the various renewable energy sources, solar energy offers abundant, silent, and eco-friendly power that has enormous potential for meeting the global energy consumption demand [2, 3]. Solar energy can be converted into electrical energy using various technologies like photovoltaic (PV) panels, concentrating solar thermal power (CSP), and concentrating photovoltaics (CVT) [4]. The photovoltaics currently present an opportunity to convert the solar energy into electrical energy. Of the PV technologies, crystalline silicon (Si)-based PV systems have been dominating the global PV market over the past five decades because of their high efficiency in electricity generation under full sunlight, the abundance of silicon on the earth's crust and the non-toxicity of the silicon material [4–6]. However, Si-based PV systems, have their own disadvantages including their energy intensive production processes, poor aesthetics, and low photovoltaic performance in low light intensities [4]. This has created a need for the development of solar cells with comparable efficiencies yet capable of performing well in low light intensities. Dye-sensitized solar cells (DSSCs) have emerged as a credible alternative to the Si-based PV systems due to their cheap fabrication processes, low toxicity, and their ability to work even in low-light conditions [7, 8]. The major problem of DSSCs is the efficiency that is low as compared to that of silicon solar cells. An efficiency of 13% has been reported and the conversion efficiencies have further improved to 34.0%, 32.7% and 31.4% under 1000, 500 and 200 lux of fluorescent light, respectively [7, 9]. Improving the efficiency and stability of the DSSCs is the major challenge most researchers are currently trying to resolve. The DSSC is mainly composed of four main components; a photoanode made up of a mesoporous oxide layer (typically,

TiO_2) deposited on a transparent conductive glass substrate; a monolayer of dye sensitizer covalently bonded to the surface of the TiO_2, an electrolyte containing redox couple (typically, I^-/I_3^-) and a counter electrode made of a platinum coated conductive glass substrate [10]. Improved performance of the DSSC can be done by modifying any of the above-mentioned cell components. Of interest recently has been the search for the development of catalyst materials for the CE with properties comparable with those of platinum (Pt). The counter electrode (CE) in DSSCs has the important task of collecting electrons from the external circuit and catalysing the reduction of the redox electrolyte [10, 11]. The key properties of a good CE material are; (i) high conductivity for charge transport, (ii) good electrocatalytic activity for reducing the electrolyte and (iii) excellent stability [12, 13]. Until this point, Pt is commonly used in the manufacture of DSSC CEs due to its high catalytic property for the reduction of the tri-iodide ions. However, Pt is a costly metal and as a result, using Pt as a CE material can raise the cost of DSSC production. Furthermore, experts are concerned about the stability of platinum in the iodic electrolyte as it corrodes and dissolves forming PtI_4 and H_2PtI_6 thereby affecting the device stability and performance [11, 14]. As substitute CEs for platinum, several carbonaceous materials such as carbon black, carbon nanotubes (CNTs), graphene, polymers, transition metal carbides, nitrides, oxides, and sulphides are currently being investigated to enhance the overall photovoltaic performance of the DSSCs [15, 16]. Due to their strong electrocatalytic activity for the reduction of I_3^-, and their plentiful availability than Pt, transition metal sulphides are one of the promising materials capable of replacing Pt [16]. Metal sulphides, and especially transition metal sulphide colloids, are a diverse, adaptable, and interesting class of inorganic compounds that are gaining in popularity due to the functional features that many of them exhibit. CoS, MoS_2, and WS_2 are examples of recent publications on transition metal sulphides. One-dimensional CoS acicular nanorod arrays (ANRAs), WS_2, and MoS_2 as CE materials in DSSCs were shown to have an overall power conversion efficiency of 7.67%, 7.73%, and 7.59%, respectively, with good catalytic activity towards the I^-/I_3^- electrolyte [16–18]. In this regard and to the best of our knowledge, we report for the first time on the synthesis of gold (I) sulphide nanostructures (Au_2S) from a single-source precursor for potential application as CE material in DSSCs.

5.2 Experimental Section

5.2.1 Materials

1-Methyl-2-pyrrolidinone (anhydrous NMP, 99.5%), lithium iodide (99.9%), iodine (≥ 99.8%), lithium perchlorate (≥ 95%), 4-tert-butylpyridine (98%), sodium iodide (anhydrous, ≥ 99.9%), acetonitrile (≥ 99.9%), N-719 dye (95%), nafion (5 wt%), white titania paste, reflector (TiO_2, 20.0 wt%), Whatman™ glass microfiber filter paper, fluorine doped tin oxide (FTO) coated glass slide (surface resistivity ~7 Ω/sq), were obtained from Sigma Aldrich and used without any further purification.

5.2.2 Fabrication of the dye-sensitized solar cells

5.2.2.1 Counter electrode fabrication

To make the counter electrode ink, 40 mg of the Au_2S synthesized previously in Chapter 4 was dispersed in a mixture of 1 mL NMP and 0.1 mL Nafion. This was left to stir for 24 h to obtain a homogenous ink mixture that was then sonicated for 20 min. The ink was drop-casted onto pre-cleaned FTO substrates (area 1.56 cm^2), then baked at 80 °C for 10 min to allow the solvent to evaporate, and then a further layer was deposited and baked as before. Two layers of platinum were sputter-coated onto a pre-cleaned FTO substrate as a reference and for comparative studies.

5.2.2.2 Photo-anode fabrication

The doctor blade approach was used to apply the titania (TiO_2) paste on the conductive side of the pre-cleaned FTO substrate. The substrates were then annealed for 30 minutes at 350°C to eliminate any remaining organic compounds and ensure that the TiO_2 was bound to the plate, allowing for better interaction with the N-719 dye. By dissolving the N-719 dye in methanol ($3.0\ 10^{-4}$ M), the photo-sensitizing dye was carefully made. A drop of the dye mixture was then applied to the annealed TiO_2 substrate and allowed to dry overnight in the dark at ambient temperatures.

5.2.2.3 Device assembly

The photo-anode electrode was placed on the bench as the bottom plate of the cell, with the sensitized TiO_2 side facing up, and the counter electrode was positioned on top of the photo-anode, with the active side facing down. The Whatman filter paper was placed between the two electrodes to act as a sponge for the redox electrolyte solution, and the two electrodes were offset from each

other. 0.05 M iodine, 0.1 M lithium iodide, 0.1 M potassium iodide, 0.1 M sodium iodide, and 0.5 M 4-tert-butylpyridine made up the redox electrolyte solution. Before performing the I-V measurements, the built device was attached with binder clips.

5.2.2.4 Electrocatalytic Activity

The Biologic: SP-300 was used to perform cyclic voltammetry (CV), electrochemical impedance spectroscopy (EIS), and Tafel polarization measurements. The CV measurements were carried out at a scan rate of 50 mVs^{-1} utilizing a three-electrode setup where Ag/AgCl electrode acted as the reference electrode (RE), Pt wire as the auxiliary electrode/counter electrode (CE) and the prepared Au_2S-CE acted as the working electrode (WE) **(Fig. 5.1)**. The triiodide redox electrolyte constituted of 0.1 M $LiClO_4$, 0.001M I_2 and 0.01 M LiI dissolved in anhydrous acetonitrile (40 mL). The EIS measurements were obtained using a symmetrical cell with two identical electrodes in the redox electrolyte used for DSSCs. The electrodes were analysed between 100kHz and 100 mHz at varying open circuit potentials for each sample. The Tafel polarization measurements were conducted at a potential window of -1.0 to 1.0 V with a scan rate of 100 mVs^{-1}. The photocurrent-voltage (J-V) characteristic curves of the DSCCs were measured in ambient conditions using the HP 4141B source measure unit (SMU) under controlled illumination of 100 $mWcm^{-2}$ (AM 1.5G).

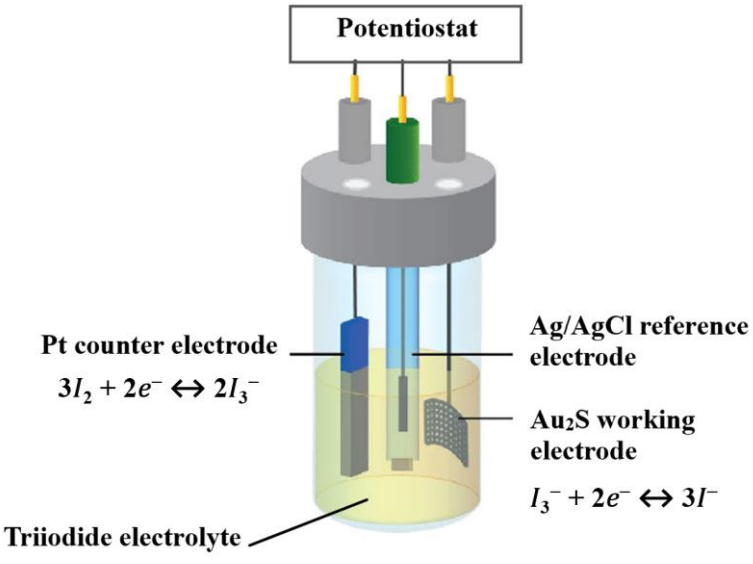

Fig. 5.1: Electrochemical measurements set-up [8].

5.3 Results and discussion

To investigate the application of the as-synthesized Au_2S CE material in DSSCs, CV studies were performed to estimate the reaction kinetics and electrocatalytic performance. CV was conducted using a three-electrode system at a scan rate of 50mV/s and the CV characterization of the Pt film-CE was carried out under the same conditions for comparison reasons. **Fig. 5.2(a)** shows the CV curves of the Pt and Au_2S CEs. From the CV curves, two pairs of redox peaks were observed, the first pair on the left (Red_1/Ox_1), directly affects the DSSC performance and the second pair on the right, (Red_2/Ox_2) has little effect on the DSSC performance. The two pairs of redox peaks have similar shapes suggesting the CEs have similar electrochemical stability and catalytic activity during the redox process [8, 19]. The negative (left side) and positive (right side) are represented by equation (5.1) and equation (5.2), respectively [19].

$$I_3^- + 2e^- \leftrightarrow 3I^- \tag{5.1}$$

$$3I_2 + 2e^- \leftrightarrow 2I_3^- \tag{5.2}$$

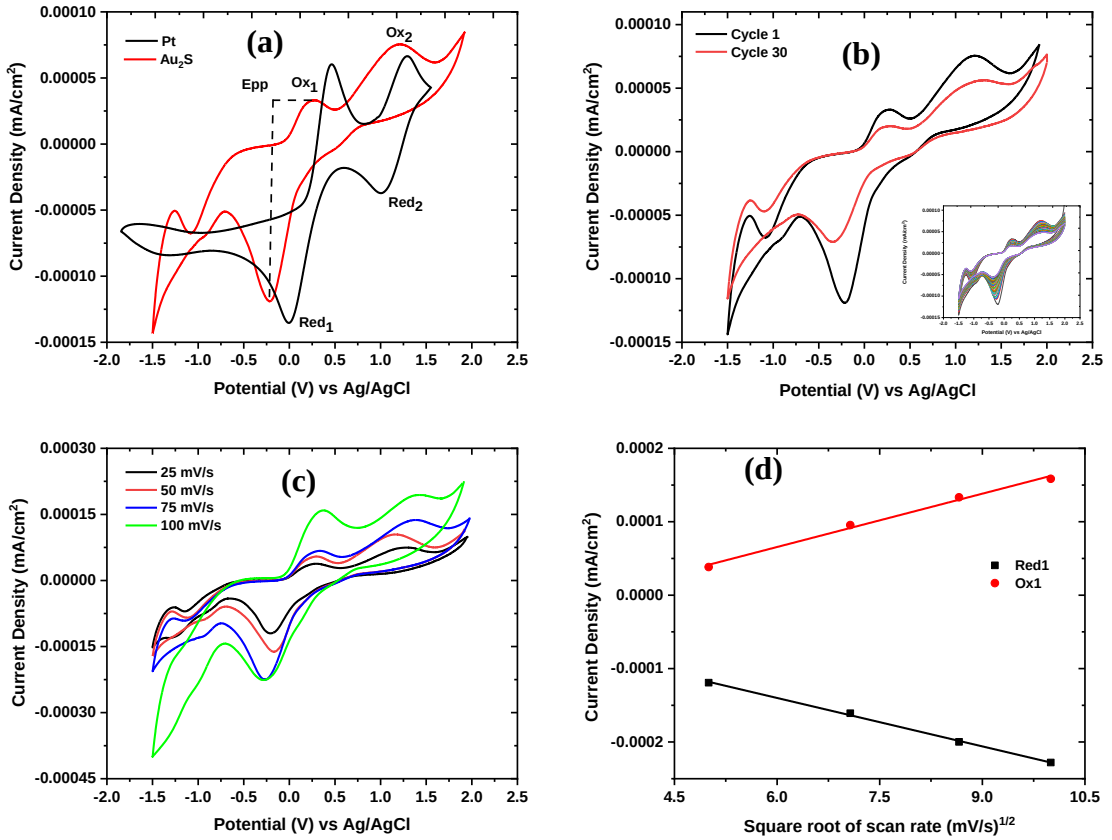

Fig. 5.2: (a) Cyclic voltammograms of the Pt and Au_2S counter electrodes at a scan rate of 50 mV/s for the I^-/I_3^- redox couple, (b) the Au_2S CE for 30 consecutive cycles, with an insert showing the 1st and the 30th cycle, (c) Au_2S CE at varying scan rates from 25 mV/s to 100mV/s and (d) dependence of anodic and cathodic peak currents on square root of the scan rates.

In DSSCs, two crucial parameters are used to compare the electrocatalytic activities of different CEs from the resulting CV curves. These are the cathodic peak current density (J_{red-1}) and the peak-to-peak separation (E_{pp}) between the first reduction peak (J_{red-1}) and the oxidation peak. These are interrelated to the reduction velocity and the reversibility of the redox reaction, respectively [19, 20]. Generally, a larger current (J_{red-1}) and smaller Epp indicates good electrocatalytic activity for the I_3^- reduction [21]. **Table 5.1** compares the discussed parameters for each CE, showing the Pt having a higher (J_{red-1}) of 1.45 mA than that of the Au_2S 1.20 mA. The E_{pp} values are in the order of Pt < Au_2S but with minimal difference, suggesting comparable catalytic activity of the Au_2S CE. The redox behaviour's long-term stability of the DSSC is one of the most important photovoltaic parameters and is assessed by conducting consecutive CV scans. The long-term stability tests of the Au_2S were conducted under the same CV measurement conditions for 30 scans and the results are shown in **Fig. 5.2(b)**. The shape of the CV curve remains constant for all the 30 cycles with little degradation in current densities or peak shifts suggesting that the Au_2S CE possesses good electrochemical stability. The behavior of the Au_2S-CE was studied under various scan rate settings, and as illustrated in **Fig. 5.2(c)**, as the scan increases, the current density and Epp also increases and **Fig. 5.2(d)** shows the relationship between the peak current density and the square root of the scan rate. The current density and square root of the scan rate have a relationship, according to equation 5.3. As the scan rate increases, the diffusion layer becomes thinner, and the electrochemical polarization becomes bigger resulting in a high overpotential and low reversibility [18]. The linear relationship suggests that diffusion limitations in cathodic and anodic reactions may affect iodide species transport on the sulfide electrode surface [22, 23]. As a result, Wu et al. [18] suggest that CV experiments should be carried out at low scan rates to establish the real

chemical reaction process. Basing on these findings, the 50 mV/s scan rate was thus identified as the favorable scan rate for the reduction of triiodide ions using the Au_2S CE.

$$i_p = 2.69\ x\ 10^5\ n^{3/2} A D^{1/2}\ V^{1/2C} \quad (5.3)$$

Where i_p is the peak current density, n is the number of electrons transferred, A is the area of the electrode, D is the diffusion coefficient, V is the scan rate, and C is the concentration [18].

Table 5.1: Electrochemical performance parameters from CV, EIS & Tafel polarization plots for the CEs

CE	|Current Red1 (mA)|	E_{pp} (V)	J_{Red-1} (mA)	R_s (ohm)	R_{ct} (ohm)	Log J_0 ($mA.cm^{-2}$)	Log J_{lim} ($mA.cm^{-2}$)
Pt	1.45	0.45	1.45	63.56	3,496	-5.44	-4.17
Au_2S	1.20	0.48	1.20	67.51	4,634	-5.56	-4.38

The electron transport parameters, that is, the ability of the CEs to transfer charge to the electrolyte, in the DSSC device were analysed using electrochemical impedance spectroscopy (EIS). In this study, EIS analysis was conducted on symmetrical dummy cells with two identical electrodes sandwiching the I_3^-/I^- electrolyte. **Fig. 5.3(a)** shows the Nyquist plots of Pt and Au_2S with the equivalent circuit representing four impedance properties, Rs, R_{ct}, Cdl and Z_w **(Fig. 5.3c)**. These parameters are defined as; R_s, the total ohmic series resistance, R_{ct} the charge transfer resistance at an interface between the CE and the electrolyte, C_{dl} which is the double layer capacitance which denotes the charge storage capacity of the CEs and Z_w which represents the Nernst diffusion impedance in the electrolyte often employed when a line is 45° to the semi-circle at lower frequency region and explains if the interaction between the CE and the electrolyte is diffusion-controlled [24]. The two key parameters, R_s and R_{ct} were fitted using the Z-fit in EC-Chem software from Biologic and are listed in **Table 5.1** for each CE. The values of the R_s were 63.56 and 67.51 Ω for the Pt and Au_2S CEs, respectively. The smaller the R_s value, the higher the conductivity of the CE. In this case the Pt has higher conductivity as compared to the Au_2S, though the difference is only marginal. From the Nyquist plot in **Fig. 5.3(a)** of Pt and Au_2S, the high frequency semicircle is due to the charge transfer resistance, R_{ct} at the CE. The values of R_{ct} for Pt and Au_2S CEs were 3496 and 4634 Ω, respectively and as with the R_s, lower values indicate higher

electrocatalytic efficiency of the CE. The lower value of the Pt again suggests its better performance with respect to the Au_2S.

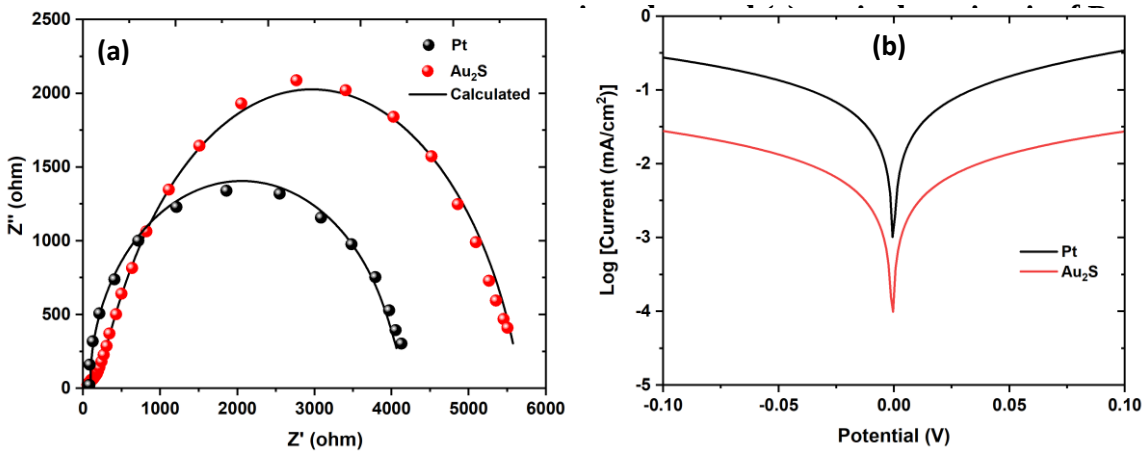

Fig. **Au**

To ere

con ing

resu ion

of v l to

desc and

the or

cathodic contributions of the C. F and are better explained using the following equations;

$$J_0 = \quad (5.4)$$

$$J_{lim} \quad (5.5)$$

where R is the gas constant, T is the temperature (298 K), F is Faraday's constant, n (n = 2) is the number of electrons, R_{ct} is the charge transfer resistance, D the diffusion coefficient, C is the

concentration of I_3^- , and l is the spacer thickness [25]. According to equation (5.4), J_0 is inversely proportional to R_{ct} and this implies that the lower the R_{ct} value at the electrolyte-electrode interface, the larger the J_0 value, hence better catalytic activity of the CE. **Table 5.1** summarizes the electrochemical measurement results obtained from CV, EIS and Tafel polarization curves. Pt has a larger J_0 value of -5.44 $mAcm^{-2}$ as compared to that of Au_2S of -5.56 $mAcm^{-2}$, indicating its better performance as a CE. Similarly, larger J_{lim} values suggest a larger diffusion coefficient D, which is controlled by the peak current of each CE material and indicates stronger catalytic activity of the CE, as shown in equation (5.5). From **Table 5.2**, the values of J_0 and J_{lim} increased as per the order Au_2S < Pt. This suggests that the Pt has better catalytic activity than the Au_2S CE. The results from the EIS and the Tafel plot are consistent with the CV data.

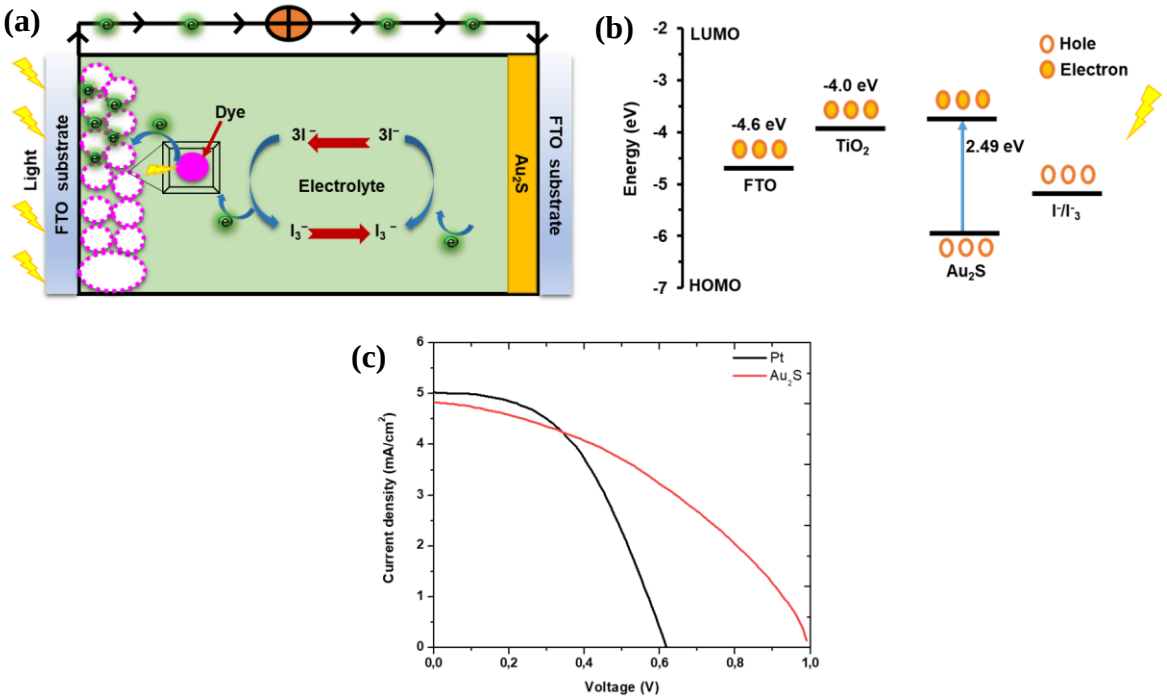

Fig. 5.4: (a) Schematic of the DSSC, (b) band diagram and (c) J-V curves of the DSSCs with Pt and Au_2S CEs.

Fig.5.4(a and b) show the construction of the DSCC and the corresponding energy band diagram. Shown in **Fig. 5.4(c)** are the photocurrent density-voltage (J-V) curves of the DSSCs assembled from the Pt and Au_2S CEs. The respective parameters of DSSC such as the open circuit voltage

(V_{oc}), short circuit current density (J_{sc}), fill factor (FF) and power conversion efficiency (PCE) are summarized in **Table 5.2**. The Pt CE showed a better PCE of 2.5% as compared to that of the Au_2S (1.94%). The current density of the Au_2S, 4.86 mA/cm^2, was relatively close to that of the Pt (5.00 mA/cm^2), and it would be expected that the performance of both devices would be similar. However, the FF of the Au_2S was lower than that of Pt due to the high R_s value which is caused by increasing recombination at interfaces of the DSSC which result from weak adhesion of the nanostructures on FTO [26, 27]. Despite the lower PCE values largely due to the construction of the solar cells, the results of Au_2S and Pt are still comparable.

Table 5.2: J-V parameters of DSSCs with Pt and Au_2S CEs

CE	J_{sc} (mA/cm^2)	V_{oc} (V)	FF (%)	PCE (%)
Pt	5.00	0.62	51	2.50
Au_2S	4.86	0.99	40	1.94

5.4 Conclusion

Electrochemical measurements including CV, EIS and Tafel polarization showed compelling evidence that the Au_2S has potential use in dye sensitized solar cells as counter electrode with good electrocatalytic activity towards reduction of I_3^- ions in the iodide-triiodide redox couple. From the J-V curves, the Pt showed the better performance (PCE 2.50 %) than the Au_2S (PCE 1.94 %), however, with some optimization studies, better values of PCE of the Au_2S can be attained.

5.5 References

[1] P.A. Owusu, S. Asumadu-sarkodie, *Cogent Engineering*, 15 (2016) 1167990.

[2] M. Kokkonen, P. Talebi, J. Zhou, S. Asgari, S.A. Soomro, F. Elsehrawy, J. Halme, S. Ahmad, A. Hagfeldt, S.G. Hashmi, *Journal of Materials Chemistry A*, 9 (2021) 10527–10545.

[3] Selectra, 2022 https://climate.selectra.com/en/environment/solar-energy accessed on 7 March, 2022.

[4] V. Devabhaktuni, M. Alam, S. Shekara Sreenadh Reddy Depuru, R.C. Green, D. Nims, C. Near, *Renewable and Sustainable Energy Reviews*, 19 (2013) 555–564.

[5] L.C. Andreani, A. Bozzola, P. Kowalczewski, M. Liscidini, L. Redorici, *Advances in Physics X*, 4, (2019) 1548305.

[6] A. Blakers, N. Zin, K.R. McIntosh, K. Fong, *Energy Procedia*, 33 (2013) 1–10.

[7] S.P. Mohanty, V. More, P. Bhargava, *RSC Advances*, 5 (2015) 18647–18654.

[8] K. Sharma, V. Sharma, S.S. Sharma, *Nanoscale Research Letters* 13, (2018) 13381.

[9] J. Gong, K. Sumathy, Q. Qiao, Z. Zhou, *Renewable and Sustaintable Energy Reviews*, 68 (2017) 234–246.

[10] M. Ye, X. Wen, M. Wang, J. Iocozzia, N. Zhang, C. Lin, Z. Lin, Materials Today, 18 (2015) 155–162.

[11] T.N. Murakami, M. Grätzel, *Inorganica Chimica Acta*, 361 (2008) 572–580.

[12] Y.S. Yen, H.H. Chou, Y.C. Chen, C.Y. Hsu, J.T. Lin, *Journal of Materials Chemistry*, 22 (2012) 8734–8747.

[13] M.R. Samantaray, A.K. Mondal, G. Murugadoss, S. Pitchaimuthu, S. Das, R. Bahru, M.A. Mohamed, *Materials*, 13 (2020) 2279.

[14] D. Ma, J. Zai, Y. Wang, Q. Qiao, X. Qian, *Chempluschem*, 84 (2019) 241–246.

[15] S. Suhaimi, M.M. Shahimin, Z.A. Alahmed, J. Chyský, A.H. Reshak, *International Journal of Electrochemical Science*, 10 (2015) 2859–2871.

[16] S. Thomas, T.G. Deepak, G.S. Anjusree, T.A. Arun, S.V. Nair, A.S. Nair, *Journal of Materials Chemistry A*, 2 (2014) 4474–4490.

[17] S. Gross, A. Vittadini, N. Dengo, *Crystals*, 7 (2017) 7040110.

[18] M. Wu, Y. Wang, X. Lin, N. Yu, L. Wang, L. Wang, A. Hagfeldt, T. Ma, *Physical Chemistry Chemical Physics*, 13 (2011) 19298–19301.

[19] X. Qian, H. Li, L. Shao, X. Jiang, L. Hou, *ACS Applied Materials and Interfaces*, 8 (2016) 29486–29495.

[20] S.N. Karthick, K.V. Hemalatha, S.K. Balasingam, F. Manik Clinton, S. Akshaya, H.J. Kim, *Interfacial Engineering in Functional Materials for Dye-Sensitized Solar Cells*, 1, (2019) 1–16.

[21] F. Liu, S. Hu, X. Ding, J. Zhu, J. Wen, X. Pan, S. Chen, M.K. Nazeeruddin, S. Dai, *Journal of Materials Chemistry A*, 4 (2016) 14865–14876.

[22] S. Biallozor, A. Kupniewska, *Electrochemistry communications*, 2 (2000) 480–486.

[23] M. Ikegami, K. Miyoshi, T. Miyasaka, *Applied Physics Letters*, 90 (2007) 153122.

[24] G. Yue, X. Liu, Y. Chen, J. Huo, H. Zheng, *Nanoscale Research Letters*, 13, (2018) 188.

[25] P.W. Chen, C.P. Lee, L.Y. Chang, J. Chang, M.H. Yeh, L.Y. Lin, R. Vittal, J.J. Lin, K.C. Ho, *RSC Advances*, 3 (2013) 5871–5881.

[26] J.A. Anta, E. Guille, *Journal of Physical Chemistry C*, 116 (2012) 11413-11425.

[27] M.A. Airo, F. Otieno, L. Mxakaza, A. Ipadeola, R.S. Kadzutu-Sithole, L.F.E. Machogo-Phao, C. Billing, M.J. Moloto, N. Moloto, RSC Advances, 10 (2020) 39509–39520.

CHAPTER 6

Overall conclusions and recommendations

6.1 Conclusions

The aim of the study presented in this dissertation was to investigate the use of gold dithiocarbamate complexes as single-source precursors for the synthesis of gold (I) sulphide nanostructures for application as counter electrode in dye-sensitized solar cells. The colloidal synthesis method was used to synthesize the nanostructures from the gold dithiocarbamate single-source precursors. Gold (I) sulphide nanostructures were successfully synthesized at optimum conditions of 170 ℃ for 45 min using oleylamine and oleic acid as the capping agents. The nanostructures' morphology was quasi-spherical with an average diameter size of ~3 nm. The effect of reaction parameters (precursor source, temperature, reaction time, and precursor concentration) on the synthesis of the nanostructures was explored. Only the temperature, reaction time, and precursor concentration had an impact on the properties of the synthesized nanostructures. Increasing reaction time and temperature increases the growth of the nanostructure's sizes because of the Ostwald ripening process. A similar effect is observed with an increase in precursor concentration. The electrocatalytic properties of the Au_2S were investigated using cyclic voltammetry, electrochemical impedance spectroscopy and Tafel polarization measurements. The material demonstrated good redox catalytic activity towards the I^-/I_3^- electrolyte because of its high current density and smaller E_{pp} value that was comparable to platinum indicating that they could be used as a counter electrode in dye-sensitized solar cells. The Au_2S-CE showed good stability in the electrolyte of the DSSC even after 30 consecutive cycles. The photovoltaic performance of the Au_2S in a DSSC was evaluated and the results were comparable to platinum with a performance of 1.94% PCE.

6.2 Recommendations

- Use other sulphur ligand sources like thiolates, thioureas and xanthates to synthesize the gold sulphur complexes and compare with the gold complexes from the dithiocarbamates.
- Carry out studies on the effect of varying capping agents to determine if they can influence the size, morphology, and optical properties of the synthesized nanostructures.

- Carry out studies to understand why the synthesized nanostructures were agglomerated and explore if size plays a role.
- Carry out post ligand exchange reactions to remove the long chain organic ligands and replace them with shorter chained ligands such as ethanedithiol or 3-mercaptopropionic acid. The post ligand exchange is important, as studies have shown that direct synthesis using shorter chained ligands yields lower quality nanoparticles that are polydispersed and agglomerated.
- Study the electrocatalytic characteristics as well as the overall performance of the DSSC using other substrates such as vitreous carbon (VC) and indium tin oxide (ITO).
- Study the effect of film deposition methods on the quality of the devices, for example use spin coating, dip coating and spray coating instead of drop casting.

Appendix

Chapter 3: Supporting information

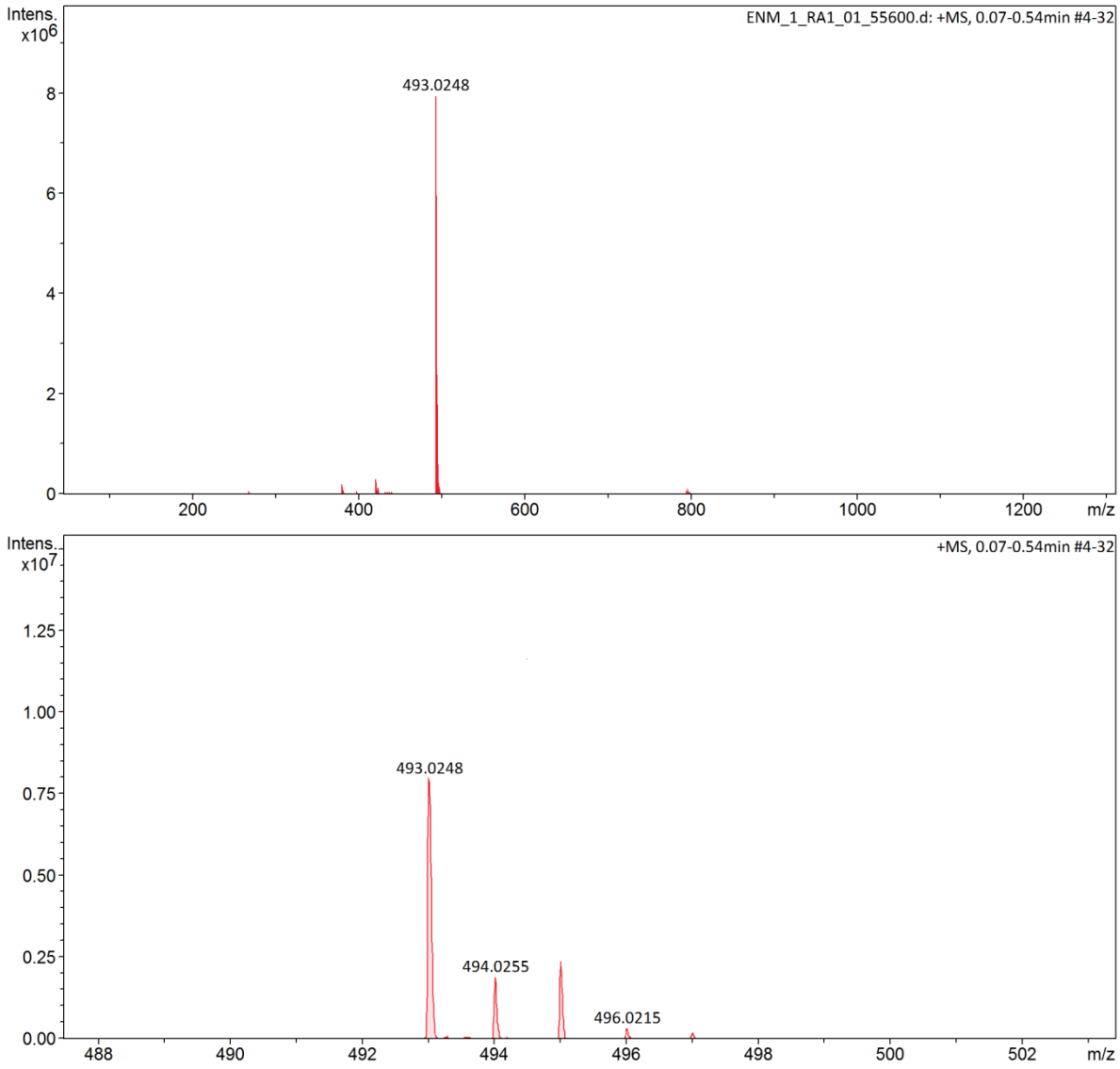

Fig. S1: Mass spectra of the Au(DTC) complex.

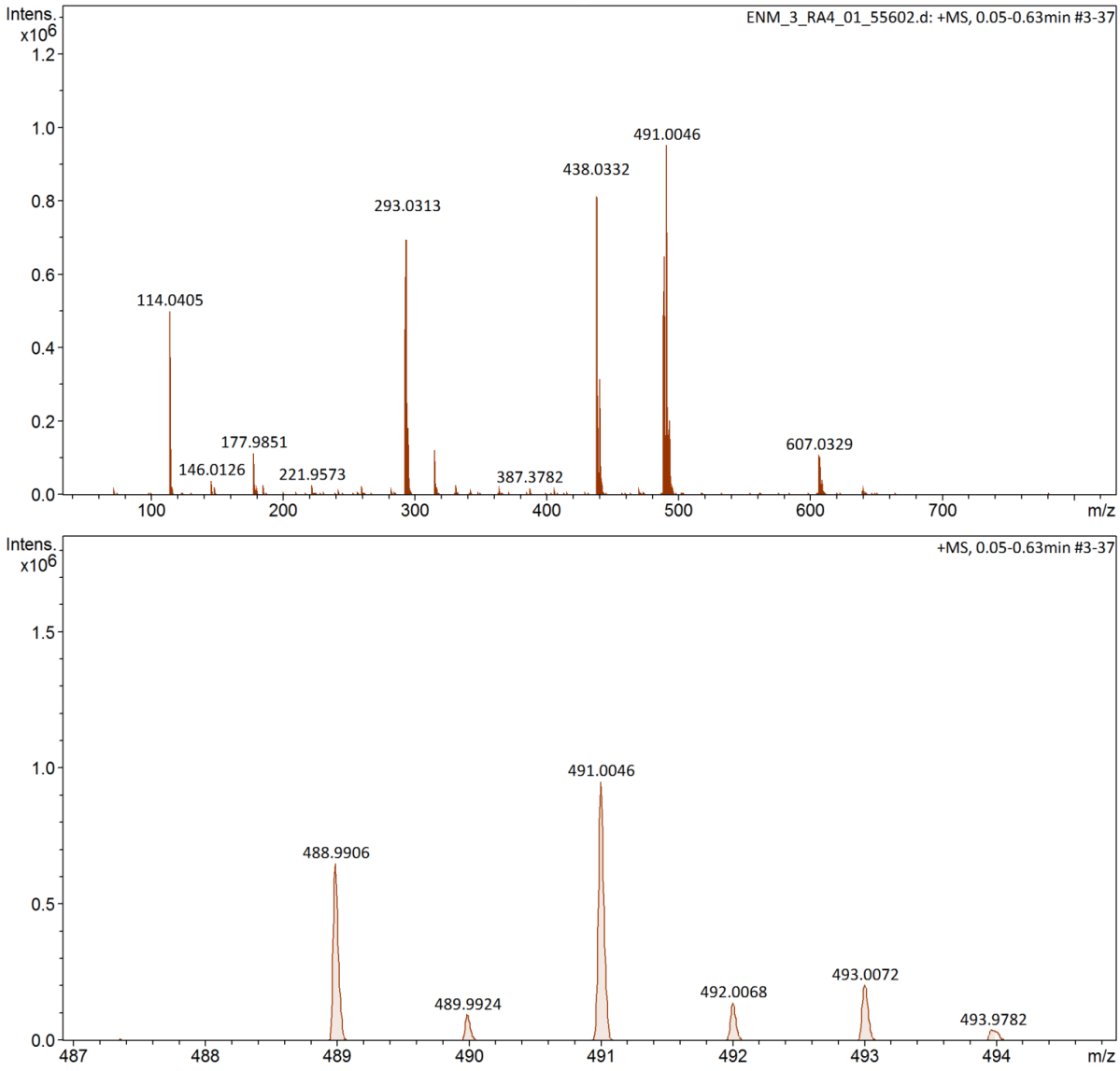

Fig. S2: Mass spectra of the Au(PDTC[1]) complex.

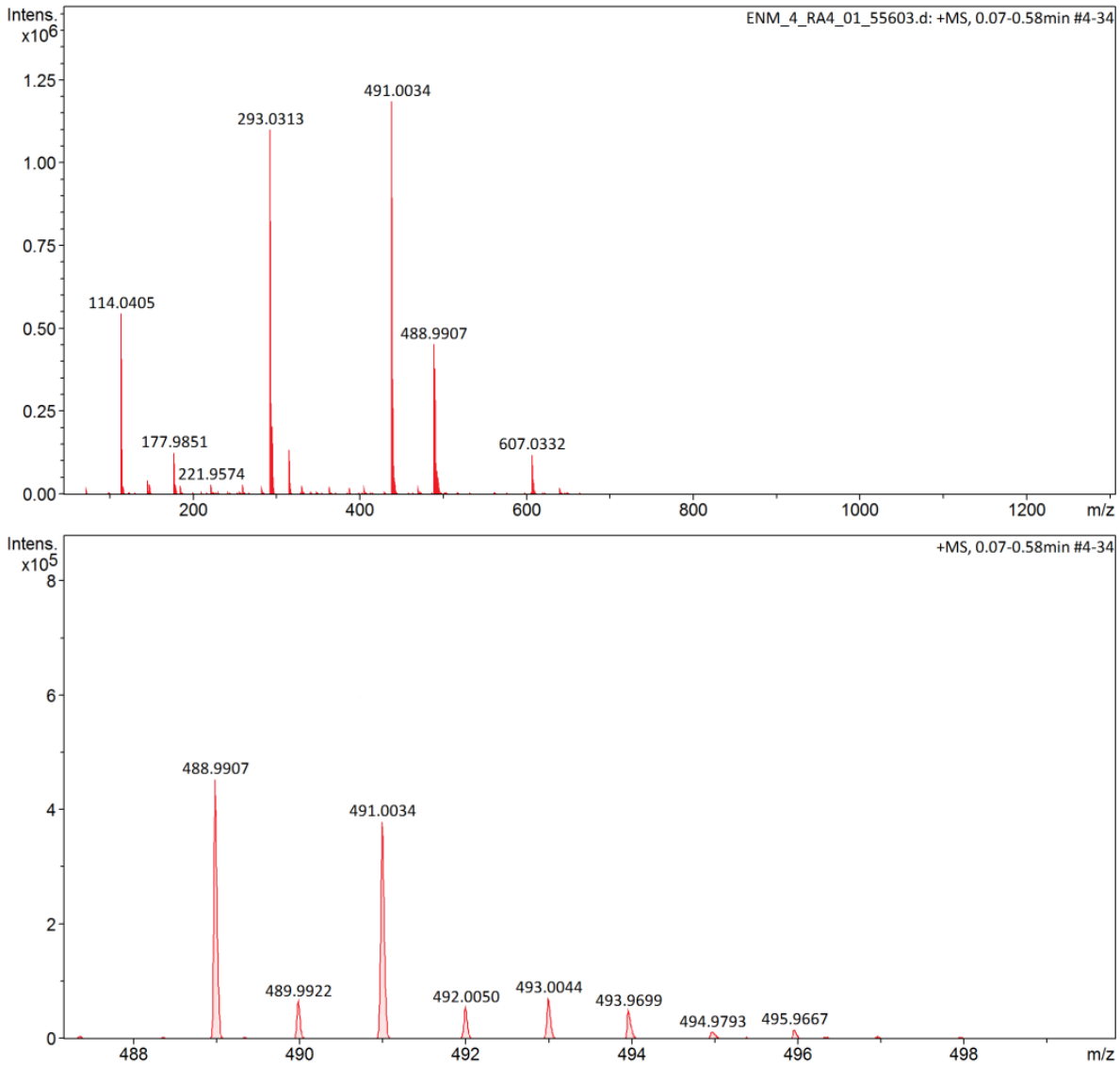

Fig. S3: Mass spectra of the Au(PDTC^2) complex.

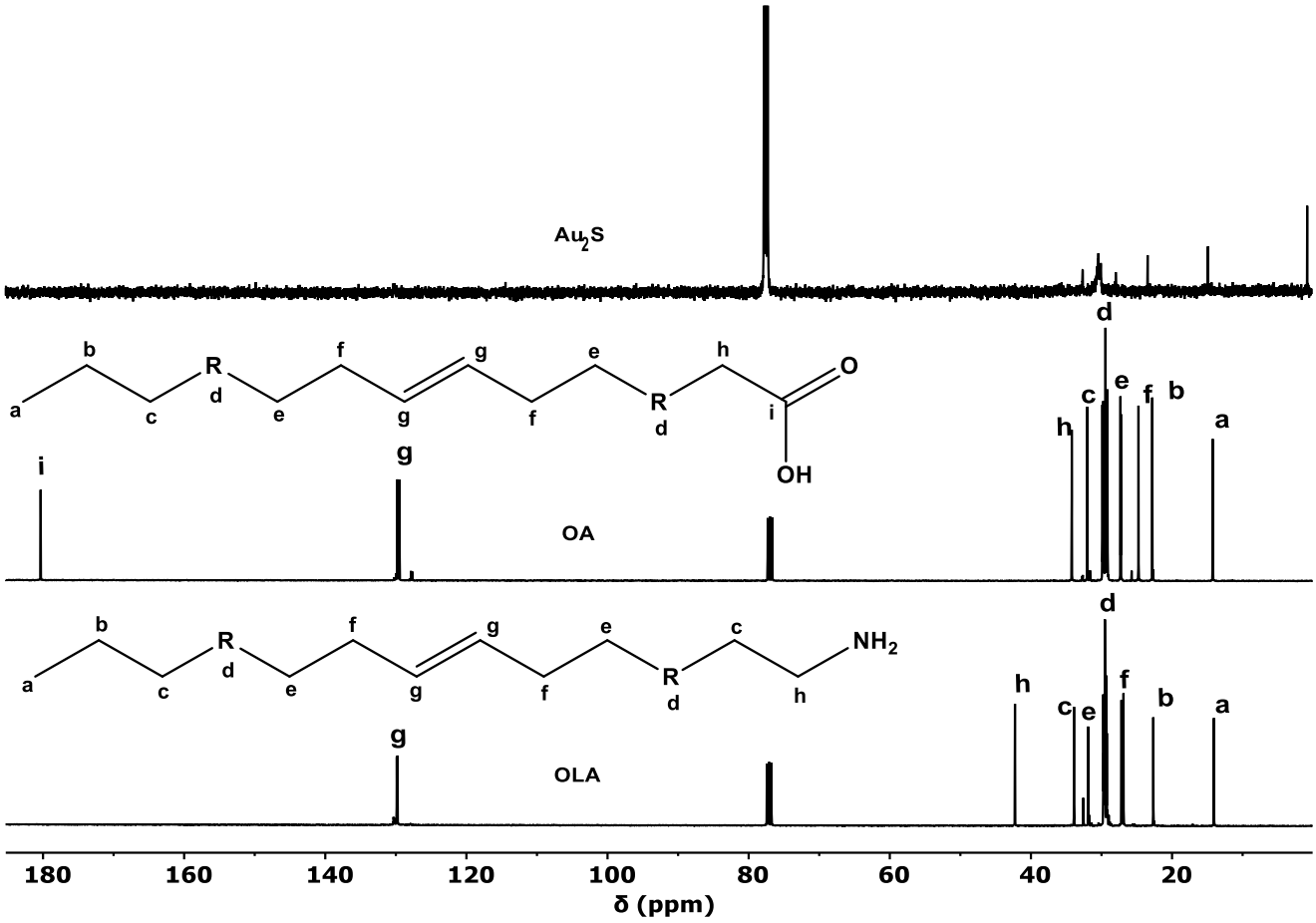

Fig. S4: ^{13}C NMR spectra of OLA, OA, and Au_2S capped nanostructures.

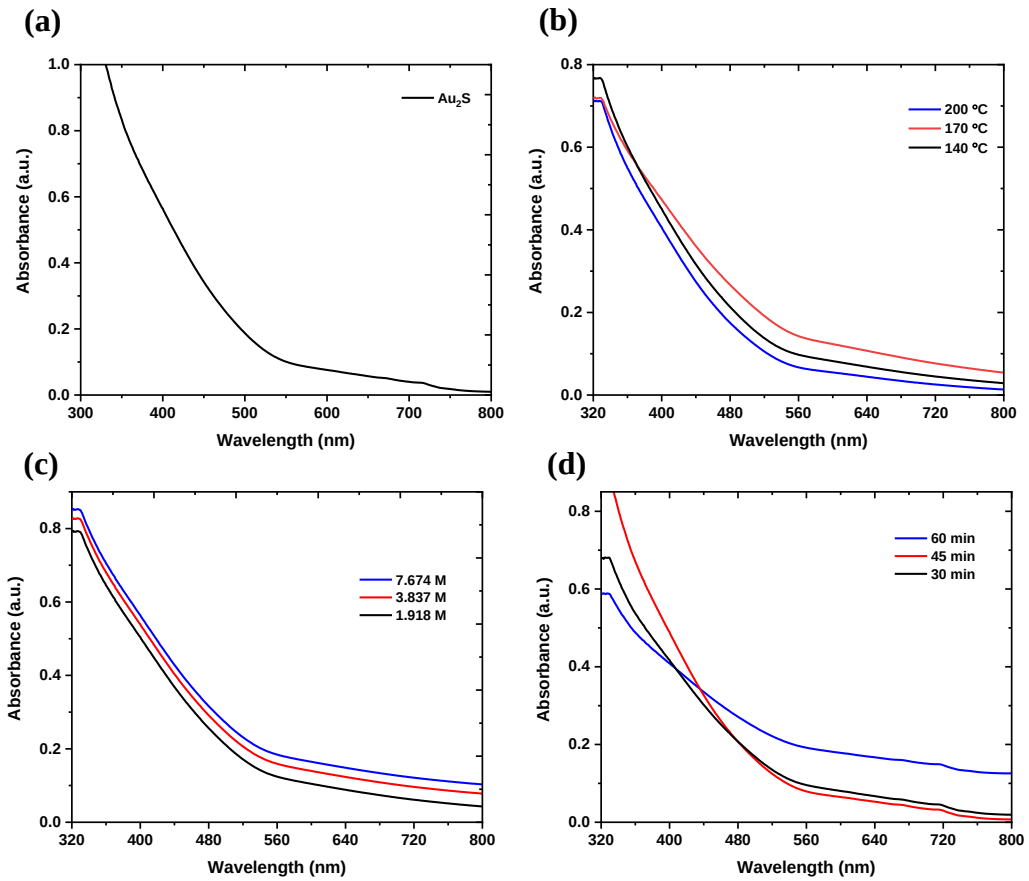

Fig. S5: UV-vis absorption spectra of Au_2S nanostructures synthesized at (a) 170 ℃ for 45 min, (b) different temperatures (c) different concentration and (d) different reaction time.